UNIVERSITY OF SOUTHAMPTON

FACULTY OF PHYSICAL SCIENCE AND ENGINEERING

School of Physics and Astronomy

Optical Trapping and Optical Sources for Nanophotonics

by

Christopher Robin Head

Thesis for the degree of Doctor of Philosophy

September 2013

To Michelle

UNIVERSITY OF SOUTHAMPTON

ABSTRACT

FACULTY OF PHYSICAL SCIENCE AND ENGINEERING
School of Physics and Astronomy

Doctor of Philosophy

OPTICAL TRAPPING AND OPTICAL SOURCES FOR NANOPHOTONICS

by Christopher Robin Head

In this thesis I describe work that I have done in two separate research areas. The first involves optical micro-manipulation of nano-scale objects and their orientation. The second concerns the development of a semiconductor laser to provide high beam quality, average and peak power and short pulse durations.

Optical tweezers are an excellent tool to manipulate nano-scale objects in all three dimensions. An additional degree of control, the rotational alignment of assymetrical particles, is demonstrated by polarisation analysis of two-photon induced fluorescence of the trapped and rotated semiconductor nanorods.

Mode-locked vertical external-cavity surface-emitting lasers (VECSELs) have recently achieved multi-watt average power levels. Nevertheless the need to optimize the gain structure design, in order to consistently obtain sub-200 fs pulse durations, still remains. The evolution of the intra-cavity power build-up transient is utilized for a novel spectro-temporal technique which allows for the extraction of the curvature of the gain spectrum during actual operation and enables the observation of the evolution of the gain spectrum during lasing build-up. In addition a method to obtain the total cavity loss via the combination of the power build-up transient and photo-luminescence decline, during lasing onset, is shown.

The use of an amplified, femtosecond-pulsed and GHz repetition rate VECSEL to generate multi-watt average power supercontinuum in photonic crystal fibres (PCFs) is presented. Supercontinuum generation with GHz pulse repetition rates is of interest for frequency combs as the high repetition rate increases the mode spacing of the comb and energy per mode. Two different PCFs, one with an all-normal dispersion profile and one with a zero dispersion wavelength (ZDW) at 1040 nm, are pumped with the amplified VECSEL pulses generating spectral components over 200 nm and 500 nm, respectively.

The thesis concludes with a proposal to use the advantages of both optical tweezers and VECSELs to analyse and resonantly excite the vibrational frequencies of single nano-scale objects.

Contents

Acknowledgements

First of all I would like to thank my supervisor, Professor Anne Tropper, for her sheer infinite amount of encouragement, wisdom and support. The two years have been tremendously enjoyable. Furthermore I thank Dr Keith Wilcox for invaluable discussions, remarkable skills in the lab and teaching me that intuition should not be underestimated. Thanks also to Professor Pavlos Lagoudakis for his patience.

Thank you to all the various group members I have worked with. In particular Junis Rindermann for many fruitful discussions and introducing me to Igor Pro, Elena Kammann for her excellent work and advice on optical tweezers, Peristera Andreakou for many shared laughs and encouragement, Andrew Acreman for a highly entertaining time and Adrian Quartermann for many mini-lectures. I could not not thank Oliver Morris for many mind opening discussions, cups of tea and helping me to locate equipment. Thank you Andrew Turnbull and Ed Shaw for many relaxing and inspiring discussions. Many thanks to all the other members of the Quantum Light and Matter group for shared ideas and advice.

I would also like to say thank you to my collaborators, especially Ho-Yin Chan and Jonathan Price for their help and persistence on the amplifier system. Furthermore Lene Oddershede and Liselotte Jauffred for advice on optical tweezers, Marco Zanella and Liberato Manna for the nanorods and Giammarino Pugliese for the procedure of nanorod transfer to water. Thank you to Wolfgang Stolz for designing, Bernadette Kunert for growing and Bernd Heinen for processing the samples used for the lasing onset measurements.

I would like to acknowledge all the department support and technical staff, without whom little of this work would have been possible. Thanks to all the electrical and mechanical workshop staff, in particular thanks to Mark in the mechanical workshop for his advice and patience teaching me many lessons that will stay with me for life.

I thank EPSRC for the funding of my PhD and the Doctoral Prize award for the "resonant vibrational spectroscopy of nano-scale particles"-project.

I am most grateful to my family and friends for their love and support without none of this would have ever been possible.

Robin Head

Declaration of Authorship

I, Christopher Robin Head , declare that the thesis entitled *Optical Trapping and Optical Sources for Nanophotonics* and the work presented in the thesis are both my own, and have been generated by me as the result of my own original research. I confirm that:

- this work was done wholly or mainly while in candidature for a research degree at this University;
- where any part of this thesis has previously been submitted for a degree or any other qualification at this University or any other institution, this has been clearly stated;
- where I have consulted the published work of others, this is always clearly attributed;
- where I have quoted from the work of others, the source is always given. With the exception of such quotations, this thesis is entirely my own work;
- I have acknowledged all main sources of help;
- where the thesis is based on work done by myself jointly with others, I have made clear exactly what was done by others and what I have contributed myself;
- parts of this work have been published as in my list of publications.

Signed:.....

Date:.....

List of Figures

Chapter 1

Introduction

In the strange world of nanoscience every discovery generates new opportunities, but often also creates more questions and challenges requiring novel techniques and tools. In this PhD thesis I describe my work on both a technique, optical micro-manipulation of nano-scale objects and their orientation, and a tool, a semiconductor laser source to provide good beam quality, high average and peak power and ultrashort pulse duration, for the investigation of the nano-scale world. The thesis concludes with a proposal for an experiment that draws on features of both, technique and tool, to study the vibrational modes of single nano-scale objects.

I describe my work on optical tweezers in chapter 2, where I show how a single-beam optical trap offers the means for three-dimensional manipulation of semiconductor nanorods in solution and furthermore how rotation of the direction of the electric field provides control over the orientation of the nanorods. The rotation of the nanorods is shown by polarisation analysis of two-photon induced fluorescence.

In chapter 3 I introduce the concept of the vertical-external-cavity surface-emitting semiconductor laser (VECSEL) and highlight recent performance milestones in continuous-wave and mode-locked operation. The VECSELs used in this thesis are based on InGaAs/GaAs quantum wells and operate at a wavelength of around 1-1.04 μm. In passively mode-locked operation the VECSELs have typically GHz pulse repetition rates with picosecond to sub-picosecond pulse durations. In section 3.2 I describe each of the

individual components necessary to build a passively mode-locked VECSEL and summarize design criteria to obtain short pulses, such as the gain bandwidth and spectral filter. Following this introduction I present my experimental work related to VECSELs in the next two chapters.

In chapter 4 I describe a method to investigate the process of lasing build up from noise in a CW VECSEL. The evolution of the stimulated emission, spontaneous emission and laser spectrum is smooth in a VECSEL, where the carrier population follows the photon number adiabatically, and relaxation oscillations are over-damped. I show how it is possible to extract the cavity photon lifetime from these measurements, establishing a precise value for the saturated gain developed by the VECSEL gain structure under specific operating conditions. Spectrally resolved measurements of the laser build-up transient show a slow narrowing of the laser spectrum, spectral condensation, over 1000s photon lifetimes, allowing the determination of the time resolved gain spectrum. The VECSEL gain structures used in this work were grown at the University of Marburg, similar in design to material that has been used to achieve record CW average power levels of over 100 W.

The use of an amplified 400-femtosecond-pulse VECSEL to generate spectral supercontinuum with multi-watt average power, in photonic crystal fibre (PCF) is presented in chapter 5. Supercontinuum generation with GHz pulse repetition rates is of interest for frequency combs, as the high repetition rate increases the mode spacing of the comb, the energy per mode and the ease with which individual modes can be isolated. In my work a VECSEL is used to seed an ytterbium-doped fibre-amplifier system, chosen as the 1040-nm VECSEL emission wavelength aligns with the gain spectrum of ytterbium-doped fibre. PCF is a fibre in which an air-hole structure produces a tight modal confinement and thus strong non-linear interactions. These cause severe broadening of the spectrum of ultrashort pulses propagating in the core, provided the dispersion characteristics of the fibre at the pulse centre wavelength are correct. Two different PCFs, one with an all-normal dispersion profile and one with a zero dispersion wavelength (ZDW) at 1040 nm, were available for this work. In order to further increase the peak power and

enhance the non-linear interactions the amplified pulses were re-compressed with a grating compressor to 400 fs, compensating the dispersion accumulated by the pulses in the fibre amplifier. The incoherent supercontinuum generated with the PCF with the 1040-nm ZDW had spectral components spread over $\sim$ 500 nm. The all normal dispersion PCF generated supercontinuum over 200 nm, which although spectrally narrower was likely to be coherent, providing an alternative approach towards the necessary coherent octave-spanning supercontinuum for frequency combs.

In chapter 6 I summarize my thesis and my major results presented in this thesis.

I conclude my thesis by describing my future work on vibrational spectroscopy of nano-scale objects using VECSELs and optical tweezers in section 6.2. Many nano-scale objects have vibrational frequencies in the GHz regime which is the typical repetition rate regime of VECSELs. Furthermore it is possible to continuously tune the repetition rate of a VECSEL over several GHz and thus enabling the locating and targeting of specific vibrational resonance frequencies, resonantly exiting them and potentially driving them into a non-linear regime or breaking point. The accuracy can be further improved by combining the resonant vibrational single particle spectroscopy with optical tweezers to remove the influence of the substrate.

Parts of this work have been published as stated in my list of publications in Appendix B.

Chapter 2

Spinning nanorods - active optical tweezing

2.1 Introduction

In this chapter I'm going to describe experiments on rotating nanorods with optical tweezers. This work has been published in Nanoscale in 2012 (Head et al., 2012).

The first work on optical micro-manipulation started in 1970 when Ashkin discovered that when photons interact with particles they transfer momentum to those particles, known as radiation pressure. Utilizing this effect he was able to push microspheres in water in the direction of the propagation of the laser beam, now known as optical guiding. With the help of an additional balanced counteracting force, such as gravity or a counter propagating laser beam, he was able to form the first optical trap (Ashkin, 1970). The breakthrough came in 1986 when Ashkin et al. were able to trap particles with a *single* tightly focused beam where the resulting gradient force at the focus was strong enough to confine the particle in all three dimensions (Ashkin et al., 1986), the birth of the optical tweezers. The gradient force, a force in the direction of the intensity gradient and proportional to the beam intensity, and trapping mechanisms are described in detail by: (Grier, 2003; Neuman and Block, 2004; Ashkin, 1997)

A further important step for optical tweezers was the ability to time-share the trapping beam between multiple traps so it was possible to trap multiple objects close to each other to study their impact on each other (Visscher et al., 1996). The ability to control the position of micro- and nano-scale particles has found a vast range of applications over the last few decades from micro-fabricating (Pauzauskie et al., 2006; Agarwal et al., 2005), particle sorting (MacDonald et al., 2003), delivery and printing(Yu et al., 2004) to many biological applications where it is necessary to target individual cells or molecules (Ashkin and Dziedzic, 1987; Ashkin et al., 1987). Optical tweezers are not only active manipulation tools, but are also excellent force sensors. The optical trapping forces applied to the trapped particle can be greater than 100 femtonewton with resolutions down to 100 attonewton (Grier, 2003). The position distribution of the trapped particle can be used to observe the influence of external forces on the particle and thus it is possible to obtain force measurements via calibrated positional measurements. This enables probing of the mechanical properties of biological tissues (Guck et al., 2000), quantifying the way DNA stretches (Gross et al., 2011) or studying microfluidic forces (Brau et al., 2007; Meiners and Quake, 1999)

Optical tweezers are able to deliver particles that can act as fluorescence markers or nanosensors to measure near-field interactions indirectly, such as quantum dots. The emission spectrum of colloidal quantum dots is highly dependent on their surrounding media (Alivisatos, 2004) thus they are able to convert information from the near-field into a property that is observable from the far-field. This combination of optical traps and quantum dots is an area under intense research interest (Jauffred et al., 2008; Jauffred and Oddershede, 2010; Ramachandran et al., 2005).

A special kind of quantum dot that has generated a lot of interest is the core-shell semiconductor nanorod. These are engineered nanoparticles with unusual fluorescence properties (Müller et al., 2005; Carbone et al., 2007). Their asymmetry imposes a defined linear polarisation on the emitted photons (Chen et al., 2001; Hu, 2001) and they are therefore promising candidates for polarised single photon emitters for quantum computing. A possible application of core-shell nanorods as electric field optical nanosensors has already been demonstrated by Müller et al. (2005).

It is possible to control not only the position of optically trapped objects but also to control the orientation of an asymmetrical object, like a nanorod, by adjusting the polarisation of the trapping beam (Tong et al., 2010; Jones et al., 2009; Bonin and Kourmanov, 2002). This has been demonstrated by Engstroem et al. for colloidal nanowires with dimensions of 100s of nanometers (Engstroem et al., 2011). Other works have shown that angular momentum of light can cause spinning of birefringent (Friese et al., 2003) or asymmetric particles (Tong et al., 2010; Ruijgrok et al., 2011).

The most widely used tool for detection and quantification of micro and nanoparticles in single beam optical traps is a quadrant photo diode (Oddershede et al., 2000). Forward scattered light, which contains information about the position of the particle, allows for extraction of the trap stiffness by analysing the distribution of positions. The trap stiffness in different dimensions has previously been used to infer the alignment of the trapped particle when it is too small to be imaged by optical means (Jauffred et al., 2008; Selhuber-Unkel et al., 2008). Here we exploit an alternative detection mechanism: the polarised emission along the long axis of semiconductor nanorods (based on core/shell CdSe/CdS nanocrystals) is utilized to show the alignment of the particle in the trap.

In my work described in this chapter I show how a single beam optical trap offers the means for three-dimensional manipulation of semiconductor nanorods in solution, and furthermore how rotation of the direction of the electric field provides control over the orientation of the nanorods, which is shown by polarisation analysis of two photon induced fluorescence.

2.2 Methods

2.2.1 Nanorods

The nanorods used in this experiment, grown by M. Zanella and L. Manna at the Instituto Italiano di Tecnologia, Italy, were CdSe/CdS core-shell structures, with the CdS shell was grown onto a spherical CdSe core. The nanorods have a cylindrical geometry capped with two half spheres, with the core located at one end of the structure. They are 33.5 ± 3.5 nm long and have a 2.5 ± 0.7 nm diameter. The electron is delocalized through the entire nanorod, whereas the hole is confined to the core due to the large offset in the valence band between CdSe and CdS (Daboussi et al., 1997; Peng et al., 1997). This material anisotropy and shape of the nanorods leads to a strong degree of polarization of the fluorescence (Talapin et al., 2003).

The rods were synthesized as described by Carbone et al. (2007) and then made water-soluble according to a published procedure which involved wrapping of the particles in an amphiphilic polymer shell (Di Corato et al., 2008).

The wavelength of the fluorescence is mainly defined by the confinement energy of the CdSe core, however the fluorescence shifts towards longer wavelengths with a CdS shell due to the decrease of the electron confinement. For these particular nanorods the centre of the fluorescence spectrum was at 580 nm.

The blinking phenomenon, sudden intermittency of the fluorescence which can last up to minutes, is typical for quantum dots and is often used to verify that they are indeed single quantum dots (Frantsuzov et al., 2008). The reasons for emission intermittency are still a mystery and keep raising more questions than answers (Frantsuzov et al., 2008). This blinking behaviour could be observed in the fluorescence of a single nanorod on a glass slide, as can be seen in figure 2.1, where sharp intensity drops to the background level are apparent. The second small peak, at the background level, in the intensity histogram in figure 2.1 is another indicator that blinking is present. The polarisation properties of single nanorods were investigated by spin-coating a low density solution of nanoparticles onto a cover slip and imaging the polarisation resolved fluorescence on

an electron-multiplication CCD. A polarisation analyser in front of the EMCCD was rotated at 0.1 Hz and the frame rate was approximately 28 frames per second. The average intensity of a region of interest containing a single nanorod is displayed in Fig. 2.2. A squared cosine fit to the data allows for extraction of the linear polarisation degree of close to 100 %. Additionally the data exhibits blinking, which confirms that the emission is indeed originating from a single nanorod.

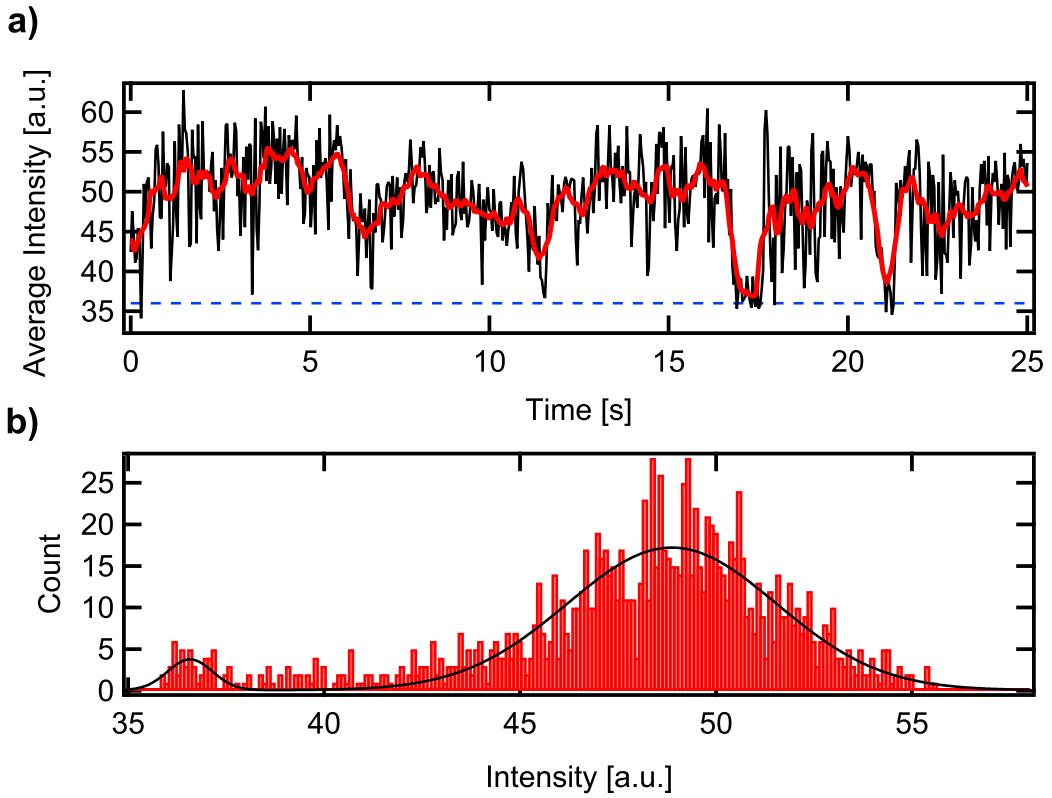

Figure 2.1: Blinking – a) Shows the average intensity trace recorded on an EMCCD of a region of interest containing a nanorod (black), a sliding average (red) and the background level (dashed blue). *Off* states can be seen in the intensity trace at around 16 and 21 s and are also evident as a second small peak at the background level in the intensity histogram of a) in b). Intermittency in the emitted fluorescence is a typical sign for a single quantum dot and is used as a proof to verify that it is indeed a single quantum dot.

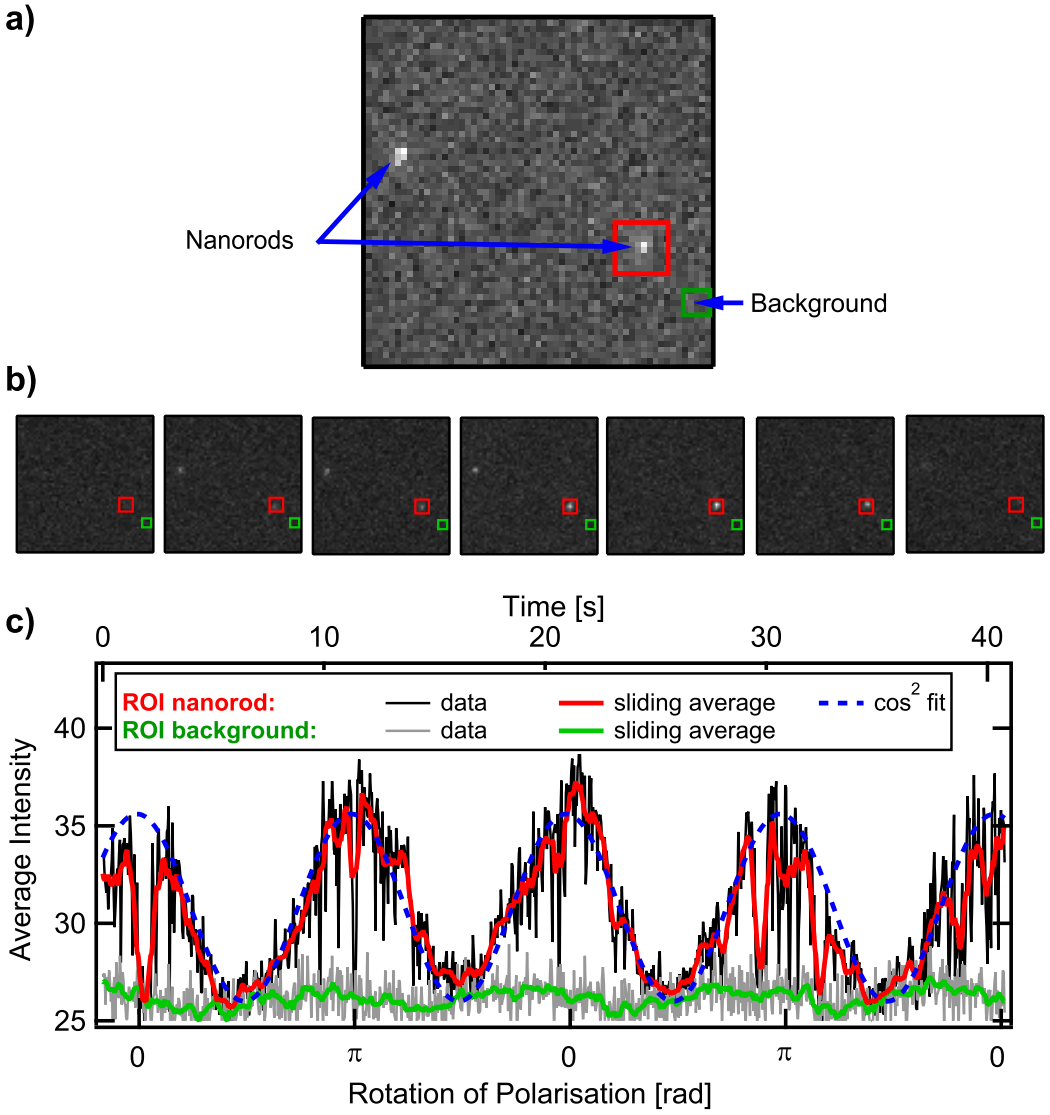

Figure 2.2: Polarized fluorescence of a nanorod on a glass slide – a) Two nanorods can be seen where one was selected with a region of interest (ROI) (red - 36 pixels) and its average intensity was recorded over time. A further ROI (green - 16 pixels) was used to record the average intensity of a region not containing a nanorod to obtain a background intensity. b) Selected frames showing the measured regions over a π-turn of the polarisation with a $\pi/6$ rotation between each. It can be seen that the intensity of the nanorods differs at different polarisation degrees, suggesting a difference in orientation. In c) the red trace is a sliding average over 10 points for the average intensity of the red ROI containing a single nanorod, whereas the green trace shows the average intensity of the green ROI. The blue trace is a cos^2 fit, which reveals a polarisation degree of nearly 100 %. Blinking is apparent at ~1.5, 11, 20, 30 and 33 s confirming that only a single quantum dot was in the red ROI.

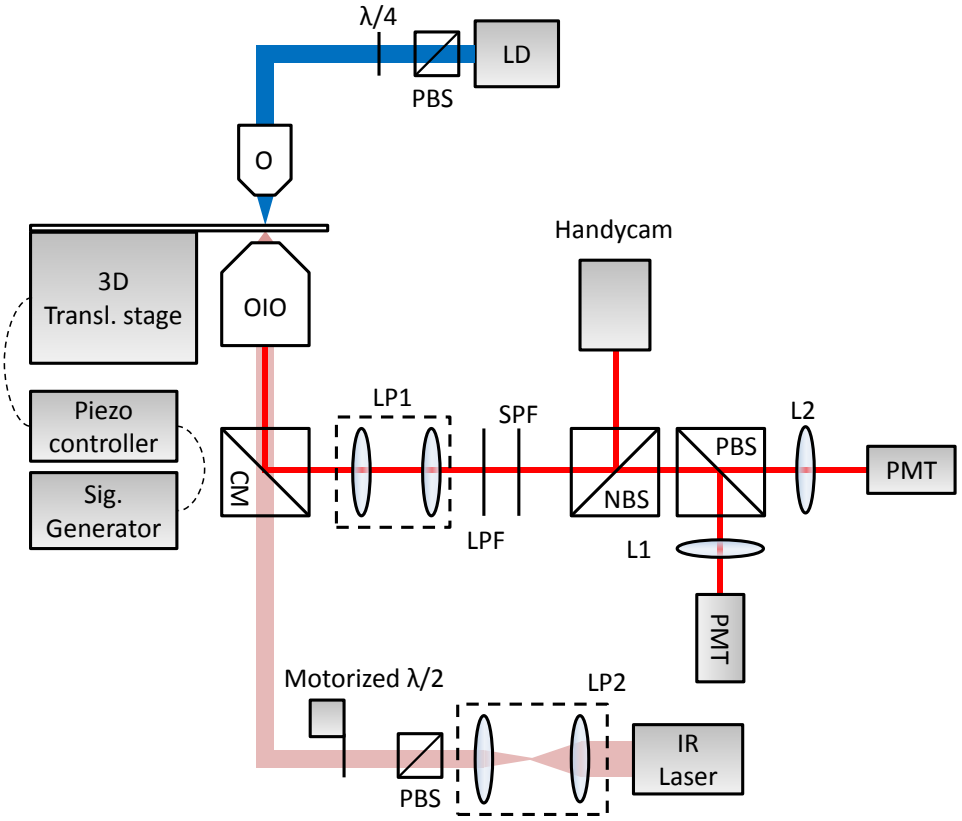

Figure 2.3: Schematic of the experiment – The nanorods are trapped by a 1085 nm CW laser that has its polarisation in the x-y plane rotated by a remote controlled half-wave plate ($\lambda/2$). The trapping laser is expanded with a lens pair (LP2) so it slightly overfills the back aperture of the oil immersion objective (OIO) to utilize its full NA (1.4). The nanorods are excited via two-photon absorption of the trapping laser. The emitted fluorescence is collected with the OIO. A near infra red cold mirror (CM) separates the fluorescence from the reflected trapping laser where a shortpass filter (SPF) blocks any left over scattered NIR light. A fraction of the fluorescence is split-off for imaging purposes with a non-polarizing beamsplitter (NBS). Lens pair 1 (LP1) is necessary to correct the imaging plane due to the difference in wavelength of the trapping laser (1085 nm) and fluorescence (580 nm). A polarizing beamsplitter (PBS) is used to split the fluorescence in two orthogonal polarisations (x and y). Two balanced photomultiplier tubes (PMTs) that record the x- and y-polarised light are used to analyse the polarization components of the fluorescence. A blue laser diode (LD) is loosely focussed with a 10x microscope objective (O) onto the sample to excite the nanorods during alignment. A longpass filter (LPF) following the cold mirror is used to block the blue laser from being imaged on the camera. The samples are mounted on a piezo controlled 3D translational stage to perform a measurement to estimate the trapped particle size, described in section 2.2.4.

2.2.2 Trapping set-up

In Fig. 2.3 the optical trapping setup is shown schematically. A 1085-nm 4-W N-light fibre laser is expanded to slightly overfill the back aperture of the microscope objective so as to exploit the full numerical aperture of the objective. The oil immersion objective had a NA=1.4 where we used an immersion medium from Cargille "Type LDF" immersion oil with a high refractive index of 1.5239 to increase the trapping strength (Reihani and Oddershede, 2007). The focused laser forms the optical trap. The sample solutions were held in a home-made liquid cell consisting of two quartz cover slides and spacers. The particles were trapped ~ 4 μm above the lower cover slide where most efficient trapping was found and spherical aberrations were minimized (Selhuber-Unkel et al., 2008; Jauffred et al., 2008). During the experiment particles in the optical trap were selectively excited through two-photon absorption of the trapping laser (Jauffred and Oddershede, 2010). This non-resonant excitation mechanism ensures that the polarisation is not inherited from the pump laser. Furthermore, two-photon absorption excitation reduces background luminescence, as only objects in the optical trap experience a photon density high enough to induce significant absorption.

The emission was collected through the trapping objective and was spectrally separated from the trapping beam using an infrared cold mirror. An additional short pass filter was used to block any left over scattered IR light. Following the short pass filter, a lens pair was used to correct the difference between the imaging plane and trapping plane due to the difference in wavelength of the trapping laser and the fluorescence. A non-polarizing beamsplitter was used to divert part of the fluorescence onto a handy-cam. Then the fluorescence was split into horizontal and vertical polarisation and simultaneously detected by two photomultiplier tubes (PMTs). A polarizing beamsplitter was used to linearly polarize the trapping laser. The direction of the linear polarisation following the polarizer was controlled by a remote controlled half-wave plate, that could be rotated at up to 80 Hz (corresponding to a polarisation rotation frequency of $f_H V = 320$ Hz). A blue laser diode (433 nm) was loosely focused with a 10x microscope objective onto the sample to excite the nanorods surrounding the trap during alignment of the set up.

2.2.3 Polarisation rotation analysis

The degree of the linear polarisation,

$$DLP = \frac{(I_{max} - I_{min})}{(I_{max} + I_{min})}, \tag{2.1}$$

where $I_{max/min}$ denotes the maximum and minimum intensity measured upon rotation of the polarisation analyser) provides insight into the nature of the trapped particle. A single particle will exhibit a high degree of linear polarisation, comparable to a single particle on a glass slide. Agglomerates of a few particles will show a reduced DLP, which is however still greater than zero. If the particle rotates the fluorescence signal on the PMTs will oscillate with the same frequency, but with a relative phase shift of π (schematically shown for a single nanorod and a small agglomerate with a reduced degree of polarisation (Fig. 2.4)).

2.2.4 Trapping force measurement

The lateral trapping force was estimated by shaking the sample chamber laterally with respect to the optical trap with an amplitude of $A = 20$ μm using a piezoelectric-controlled stage. The movement of the stage was controlled with a signal generator that applied a continuous triangular function with a variable frequency. The speed of the solution with respect to the optical trap is given by $v = 2fA$, where f is the triangular wave oscillation frequency. The lowest frequency at which the trapped particle leaves the trap, ergo when the drag force of the solution exceeds the lateral trapping force, is used to estimate the lateral trapping force using Stokes' law $F_d = 6\pi\mu Rv$ (Oddershede et al., 2000), where F_d is is the drag force exerted, μ the viscosity of the solution, and R the radius of the particle. The frequency at which the particle is pulled out of the trap is referred to as the escape frequency.

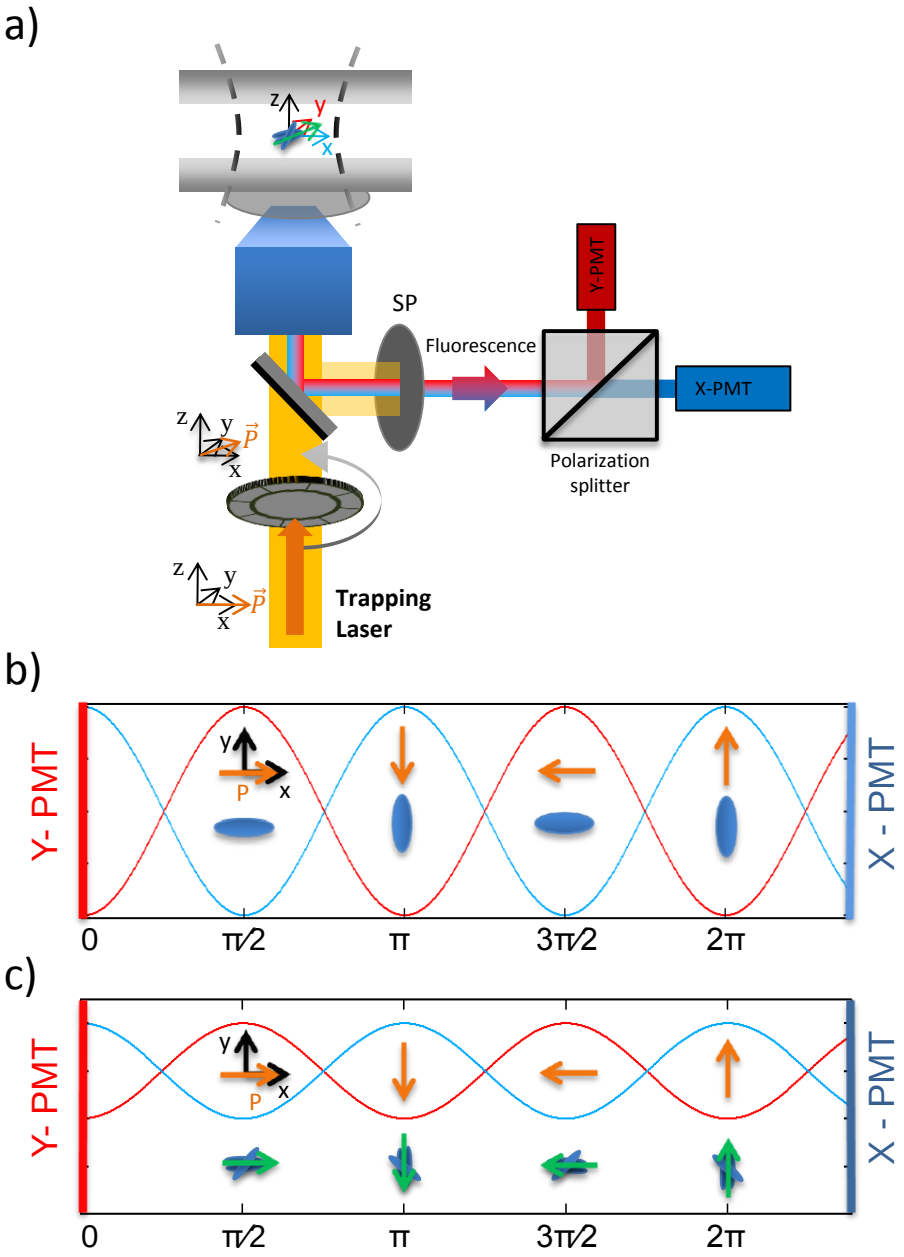

Figure 2.4: Schematic fluorescence signal from a spinning nanorod – a) Simplified schematic of the trapping set-up (Fig. 2.3) b) Single nanorods emit light, which is polarised along their long axis. Upon rotation of the input polarisation the particle follows the orientation of the polarisation. This can be observed by a sinusoidal modulation in the signal on the PMTs which anti-correlate with respect to each other. The amplitude of this modulation is close to the amplitude measured for a single particle on a glass slide. c) For an agglomerate of a few nanoparticles the observed degree of polarisation is reduced due to the different orientations of the individual nanorods in the agglomerate.

2.3 Results and discussion

When imaging the nanoparticles in solution we found a certain inhomogeneity in particle brightness, which leads to the conclusion that some of these particles in the solution are in fact agglomerates of several nanorods. These small agglomerates were equally observed in transmission electron micrographs (TEM), as shown in Fig. 2.5a)-d). We did not succeed in trapping single nanorods in low density solutions, thus in our experiments we used high concentration of particles to ensure a broad distribution of various agglomerate sizes. For sufficiently small agglomerates with high anisotropy (Fig. 2.5a),b) and c)) it is still expected that the particle aligns in the optical trap and that the emission is polarised, albeit to a smaller degree than for a single particle.

Fig. 2.6 a), b) display intensity traces of the two balanced photomultiplier tubes, recording the horizontal (red) and vertical (blue) polarisation of a trapped particle as a function of time (bottom) and angle of polarisation with respect to the horizontal axis (top) with a sliding average over 200 points (0.02 s) (the polarisation was rotated at 1.25 Hz). The background reading for each trapped agglomerate was measured once the escape frequency was determined and thus the agglomerate had left the trap. When the trap was focused onto a dense solution of rhodamine 6G instead, a modulation of the signal was equally observed, corresponding to the rotation frequency f_{HV}. However in this case the signal from both PMTs oscillated with the same phase, which indicates a small polarisation dependent intensity fluctuation of the trapping beam.

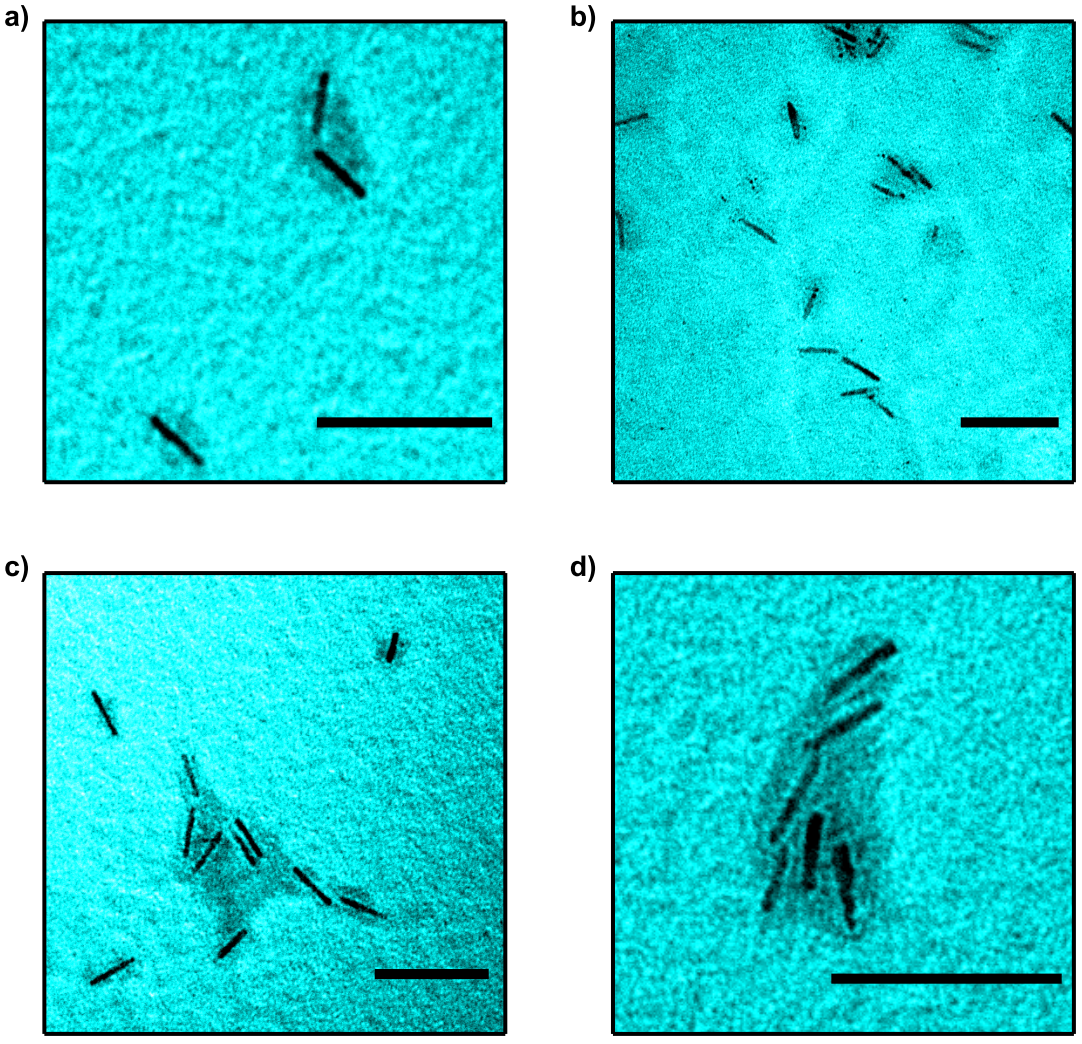

Figure 2.5: TEM of nanorods from single particles to small agglomerates – a) d) Transmission electron micrographs of the nanorods. Ligand material causes nanoparticles to form small agglomerates of for example 2 a), 8 c) or 6 d) nanorods. Black bars are 100 nm long. Small agglomerates still exhibit a high anisotropy.

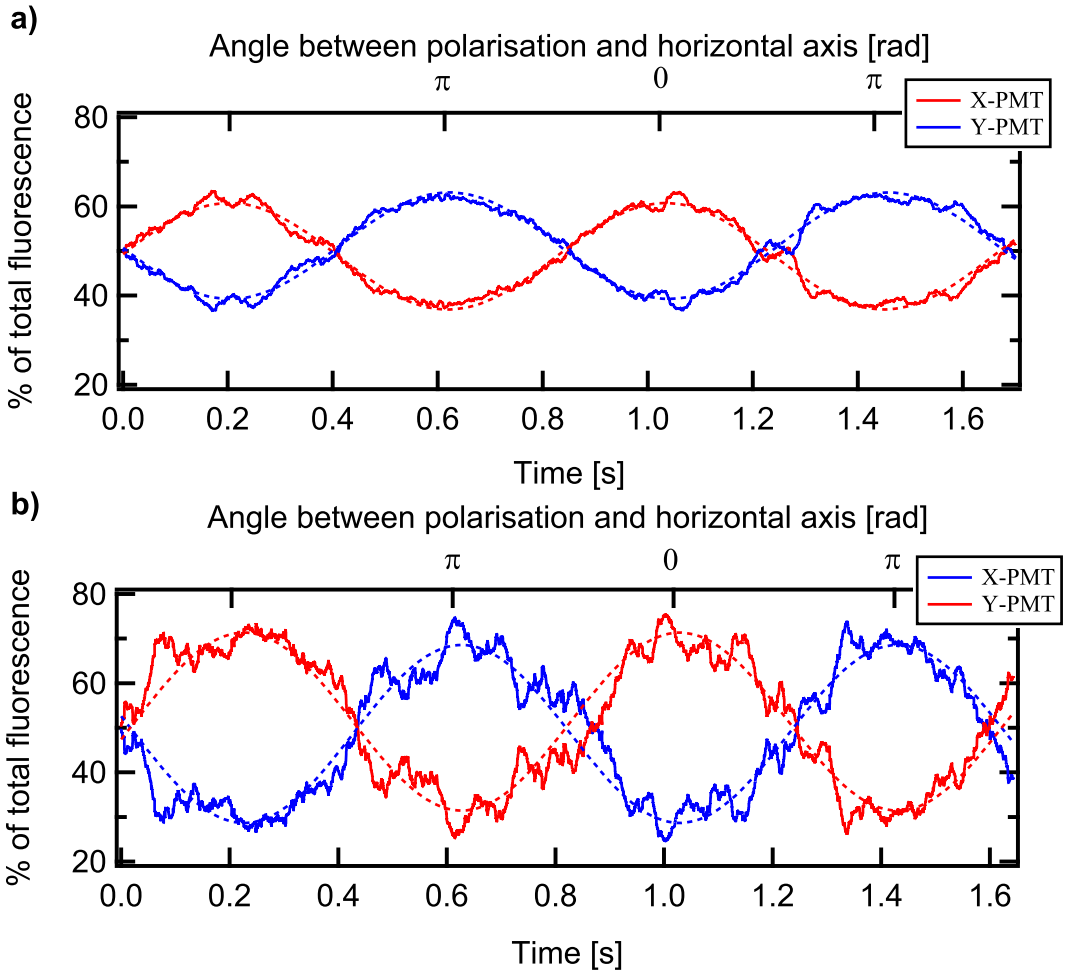

Figure 2.6: Polarisation spectroscopy of two different spinning nanorod agglomerates – a) & b) Signal on the two PMTs from a rotating agglomerate as a function of time/ degree of polarisation with respect to the horizontal axis at 1.25 Hz with a sliding average over 200 points (solid) and a sinusoidal fit (dashed). The trapped agglomerate in b) exhibits a greater DLP than the agglomerate in a).

2.3.1 Rotation speed

A rotation frequency-dependence was then performed in order to determine if the aligned particles can follow the rotation of the polarisation up to a frequency $f_{HV} = 320$ Hz, which is the maximum frequency achievable with our apparatus. The polarisation of the trapping beam was rotated at different frequencies (f_{HV}). As the signal from the rotating particles was contaminated by the mains noise frequency (50 Hz) the normalized signal was analysed with a Fast-Fourier-Transformation (FFT) shown in Fig. 2.8 a). We compared the heights of the FFT peak at the rotation frequency with the normalized Fourier-spectrum of the results obtained for rhodamine 6G, to ensure that the signal modulation is not caused by an intensity modulation of the trapping beam. In Fig. 2.8 a) the ratio of the amplitude of f_{HV} of the rotated nanorod ($A(f_{HV}, NR)$) and the rhodamine ($A(f_{HV}, RHO)$) is plotted as a function of rotation frequency. The ratio remained strictly greater than 1, confirming that the trapped particles can follow the rotation frequency up to $f_{HV} = 320$ Hz and that there was no significant dependence on the rotation frequency in the measured range.

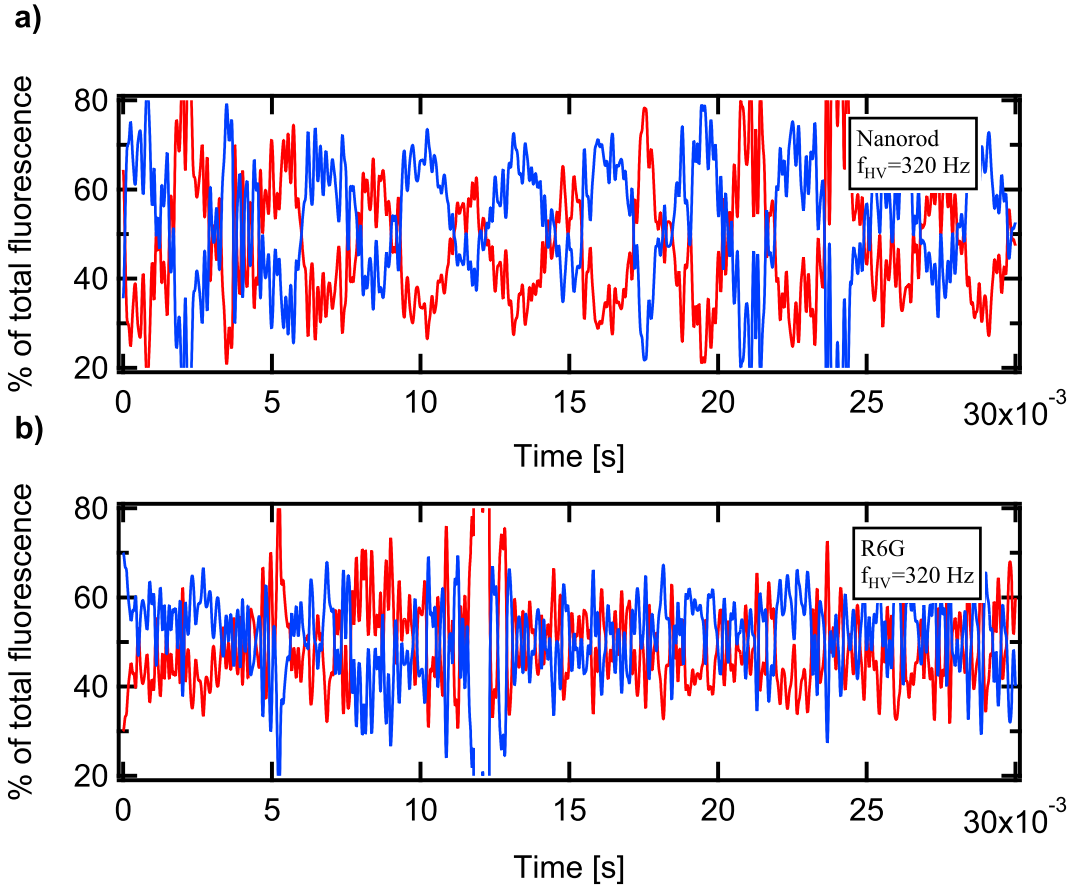

Figure 2.7: Spinning nanorods at 320 Hz – a) Shows the recorded intensity traces for both polarisations of a trapped nanorod during the rotation of the trapping polarisation 320 Hz. Even though the signal has become siginificantly more noisy it is still possible to see the anticorrelation between the two orthogonal polarisations at the rotational frequency. b) To verify whether the signal is due to an intensity fluctuation the nanorods have been replaced with a rhodamine solution where there is no anticorrelation visible.

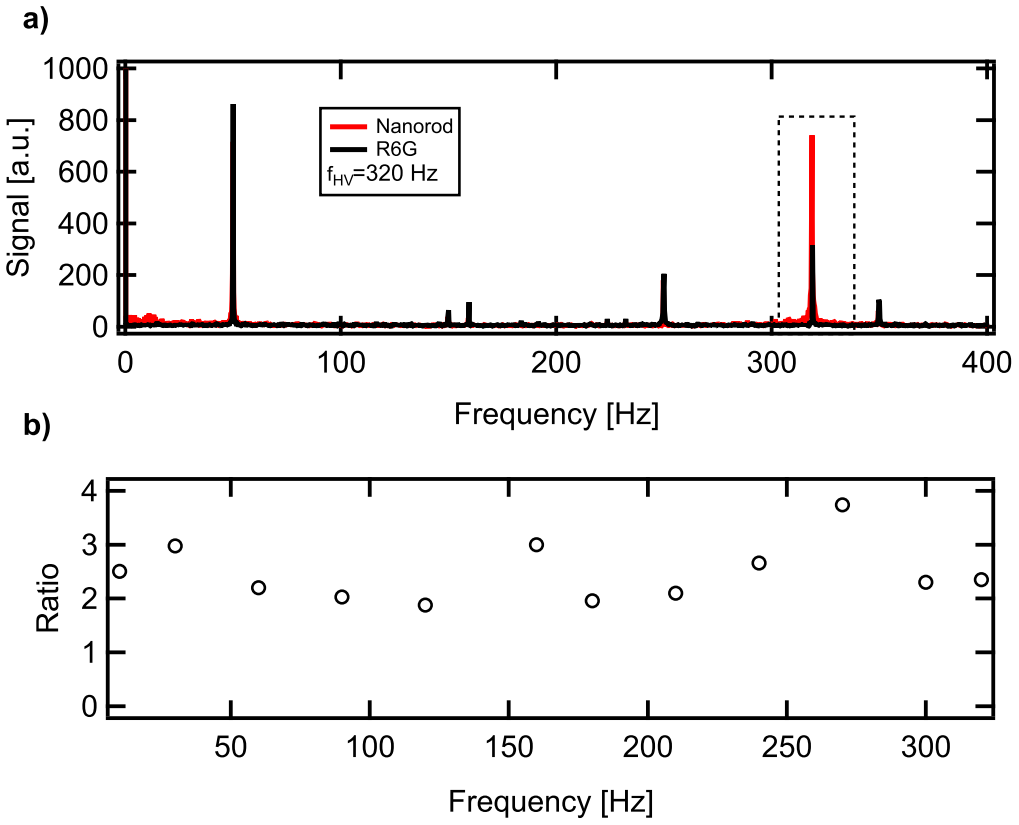

Figure 2.8: FFT analysis – a) Normalized Fourier spectra of the signal from the PMT at a rotation speed of 320 Hz for the nanorods (red) and rhodamine 6G (black). The peaks at 50, 150, 250 and 350 Hz were always evident and originated from the mains noise and a sub-harmonic of the rotation frequency can also be observed. The peak at 50 Hz is greater than the signal itself requiring the FFT data extraction. b) The ratio of the peaks at rotation frequency, for different rotation frequencies. This quantity remains strictly greater than one, confirming that the trapped particles follow the linear polarisation up to 320 Hz.

2.3.2 Degree of polarisation

From the intensity traces of the trapped particles vs time (as displayed in Fig. 2.6a)), it is possible to extract the degree of linear polarisation (DLP). Fig. 2.9 displays a scatter plot of the DLP for 40 trapped particles vs the escape frequency (Fig. 2.9 a)) and the absolute emission intensity (Fig. 2.9 b)). We found that the DLP has a tendency to be lower for brighter particles and higher escape frequencies. This observation confirms that smaller agglomerates have a higher anisotropy and therefore exhibit a large DLP. We measured DLPs of up to 51.5 % for the smallest of particles in the optical trap. Even though this is only half of the DLP of the single nanorod on a glass slide one must consider that the particles cannot be completely immobilised in the optical trap.(Jauffred et al., 2008) The polarisation induced alignment competes with the Brownian motion of the trapped particle. These thermal fluctuations cause a reduction of the DLP.

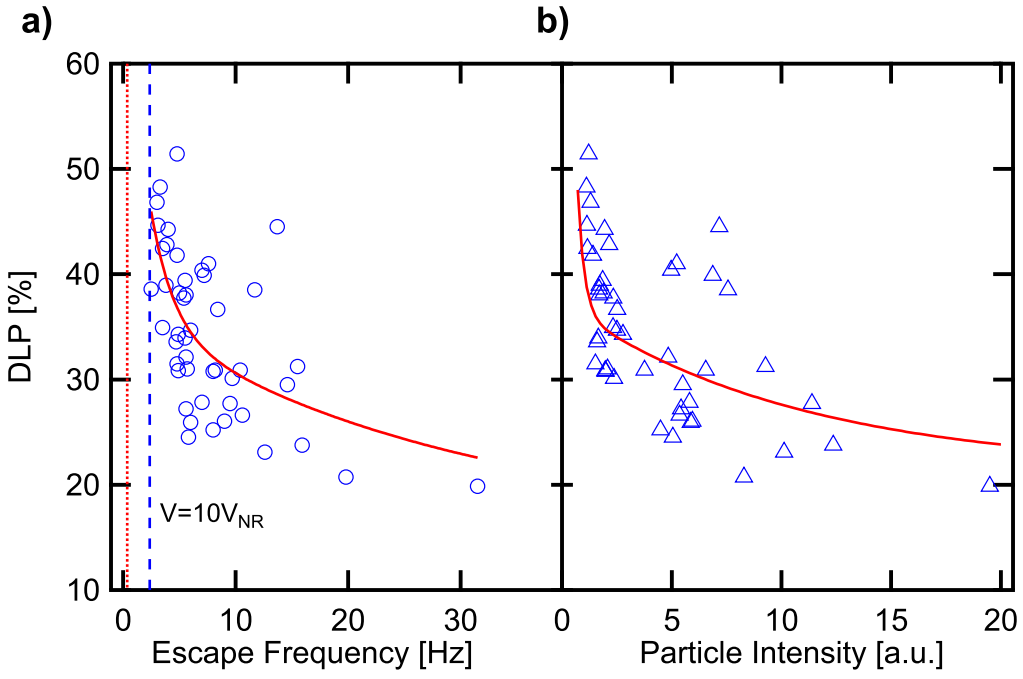

Figure 2.9: DLP statistics of particles in the optical trap – Scatterplots of the measured degree of polarisation (DLP) vs a) the escape frequency and b) the particle intensity emitted of 48 separately trapped objects. A higher degree of polarisation is observed for particles with lower intensity and smaller escape frequencies. The vertical lines in a) indicate the escape frequencies expected for a spherical particle of the same volume as one (red dotted) and ten (dashed blue) of our nanorods. The solid red lines are guides to the eye.

2.3.3 Size distribution

In a final experiment we estimated the size of particles of the trapped agglomerate, by introducing an effective radius, R_{eff}, that corresponds to a spherical particle with the same polarisability as the randomly shaped object in the optical trap. The polarisability of the object can then be approximated as the polarisability of a spherical particle with the radius R_{eff},

$$\alpha = 4\pi n_2^2 \epsilon_0 R_{eff}^3 \frac{m^2 - 1}{m^2 + 2}, \tag{2.2}$$

where n_2 is the refractive index of the solution, ϵ_0 the dielectric constant, n_1 the refractive index of the particle and $m = \frac{n_1}{n_2}$. We calculate the lateral trapping strength using the Rayleigh scattering model (Harada and Asakura, 1996):

$$F_{grad}(x, z) = \frac{-\alpha}{2c\epsilon_0} \frac{I(x, z)}{(1 + 2z^2)} \frac{4x}{w_0}, \tag{2.3}$$

Where α is the polarisability, w_0 the beam diameter at the waist and c the speed of light. The trapping laser intensity is given by

$$I(x, z) = \frac{2P}{\pi w_0^2} \frac{1}{(1 + 2z^2)} e^{-\frac{(2x^2)}{(1+2z^2)}} \tag{2.4}$$

where P is the laser power. We set z to the equilibrium position of the particle, $z = \frac{2\pi}{\lambda} \frac{w_0^2}{2\sqrt{3}}$, where gradient and scattering force are of equal size and opposite direction. Known parameters from the experiment are $P = 0.55\ W$, $n_1 = 2.37$, $n_2 = 1.332$, $\lambda = 1085$ nm and $w_0 = 1\mu$m. Using Stokes' law we can estimate the escape frequency as a function of particle size. The obtained curve is plotted over the data that correlates the particle intensity and the escape frequency (Fig. 2.10). The escape frequencies for a single spherical particle of the same volume as the nanorods and an agglomerate of 10 particles are indicated in the figure. The calculation should, however, be treated only as an estimate to determine the agglomerate size, as there are several factors not taken into account. As in a first order approximation the trapping force depends on the volume of the trapped object, we assumed a spherical shape of the trapped object as it only takes into account the volume of the particle and we don't know the exact shape of each trapped agglomerate. Furthermore Oddershede et al. have found the relation between

aspect ratio, volume and trapping strength to deviate from any theoretical prediction (Selhuber-Unkel et al., 2008). The spotsize was estimated using $w_0 = 1.22\lambda/NA$, although it is likely to be bigger as the microscope objective used was not optimized for NIR wavelength. We assumed a linear scaling between the agglomerate volume and fluorescence intensity. The energy transfer between the nanorods is mainly non-radiative and the transferred energy will eventually be reemitted as fluorescence by a nanorod, which will be only slightly lower due to a <100% quantum yield. Thus the overall intensity will be only marginally reduced due to agglomeration. Furthermore our calculation neglects the polymer coating around each nanorod and also some excess organics, which are also part of the agglomerate as visible on the TEM pictures (Fig. 2.5 a)-d)). The ligand material contributes to the volume and hence to the trapping strength, thus the agglomerates could contain fewer particles than calculated.

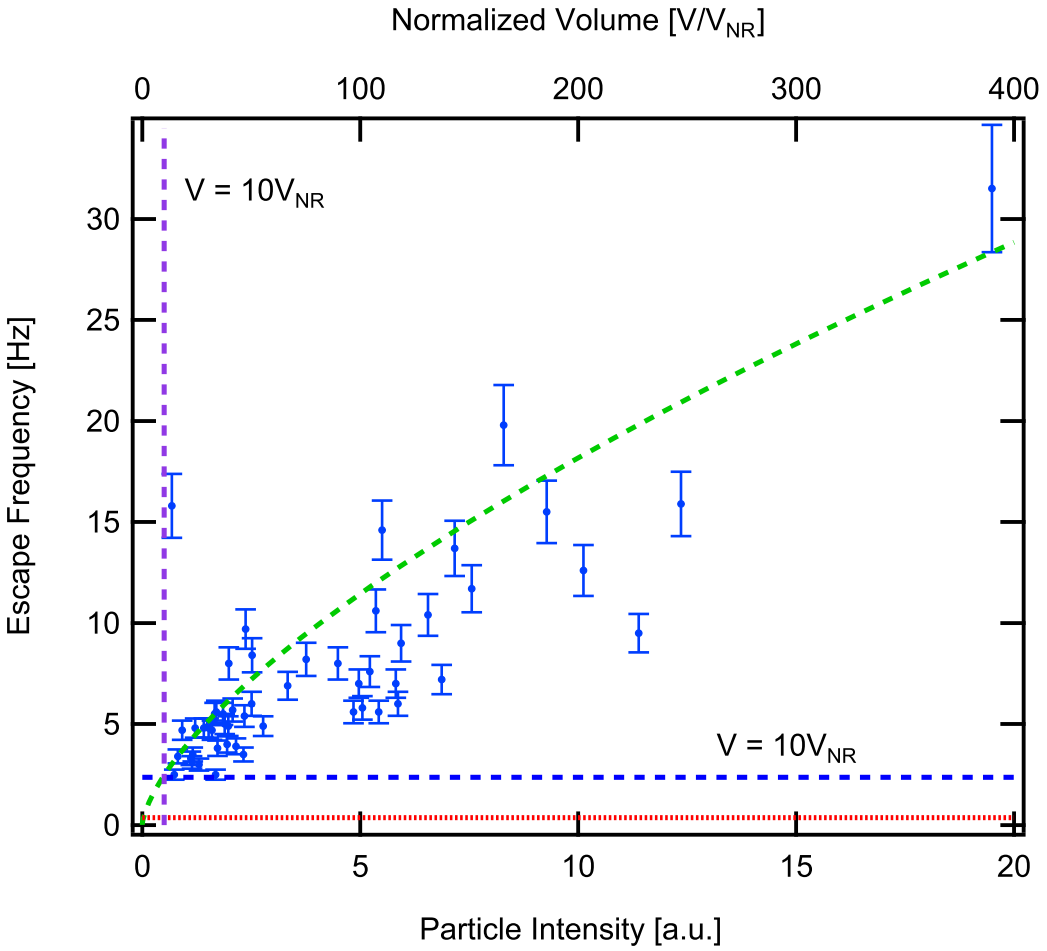

Figure 2.10: Size estimation of particles in the optical trap – Scatterplot of the measured the escape frequency vs the particle intensity of 48 separately trapped objects. The green dashed line is the calculated dependency of the escape frequency on the volume of the particles superimposed on the data to estimate the volume of the agglomerates. The horizontal lines indicate the escape frequencies expected for a spherical particle of the same volume as one (red dotted) and ten (dashed blue) of our nanorods. The effective volume of ten nanorods is marked by the dashed purple line.

2.4 Conclusions

In conclusion we have optically trapped and aligned agglomerates of CdSe/CdS nanorods, which was demonstrated by polarisation resolved fluorescence detection. Although we were not able to trap single nanorods statistics over tens of particles show a correlation between intensity, escape frequency and the degree of linear polarisation (DLP). These findings allow us to estimate the size of the smallest agglomerate we were able to trap to be about ten times the volume of a single nanorod. However as the ligand material contributes to the volume, and hence to the trapping strength, our smallest calculated agglomerate is actually likely to be smaller. Thus we have demonstrated rotational alignment of optically trapped particles on the nanoscale.

The nanorods used in this experiment tend to form agglomerates where the individual nanorods are parallel to each other. Thus the agglomerates maintained their anisotropy and followed the change in polarisation observable in the anti correlation of the two orthogonal PMT signals. The decrease in the DLP for bigger agglomerates suggests that the nanorods become increasingly more randomly orientated with increasing agglomerate size.

It has been shown that the agglomerates rotate up to rotation frequencies of 320 Hz, the fastest we could rotate the polarisation of our trapping beam, suggesting that the alignment force is sufficient to overcome rotational drag forces on the nanorod agglomerates at the frequencies we were able to test. The use of rotating nanorods could be very interesting as nanomixers in microfluidics where the laminar flow enables highly accurate control over amounts of fluids but hinders mixing of different fluids.

These observations pave the way to controlled assembly of nanorods to functional materials and specific positioning of optical nanosensors with control over the alignment of the nanoparticle.

References

Agarwal, R., Ladavac, K., Roichman, Y., Yu, G., Lieber, C., and Grier, D. (2005). Manipulation and assembly of nanowires with holographic optical traps. *Optics Express*, 13(22):8906–8912.

Alivisatos, P. (2004). The Use of Nanocrystals in Biological Detection. *Nature Biotechnology*, 22(1):47–52.

Ashkin, A. (1970). Acceleration and trapping of particles by radiation pressure. *Physical Review Letters*, 24(4):156–159.

Ashkin, A. (1997). Optical trapping and manipulation of neutral particles using lasers. *PNAS*, 94(10):4853–4860.

Ashkin, A. and Dziedzic, J. M. (1987). Optical trapping and manipulation of viruses and bacteria. *Science*, 235:1517–1520.

Ashkin, A., Dziedzic, J. M., Bjorkholm, J. E., and Chu, S. (1986). Observation of a single-beam gradient force optical trap for dielectric particles. *Optics Letters*, 11(5):288–290.

Ashkin, A., Dziedzic, J. M., and Yamane, T. (1987). Optical trapping and manipulation of single cells using infrared laser beams. *Nature*, 348:348–352.

Bonin, K. and Kourmanov, B. (2002). Light torque nanocontrol, nanomotors and nanorockers. *Optics Express*, 10(19):984–989.

Brau, R. R., Ferrer, JMand Lee, H., Castro, C., Tam, B., Tarsa, P., Matsudaira, P., Boyce, M., Kamm, R. D., and Lang, M. J. (2007). Passive and active microrheology with optical tweezers. *Journal of Optics A: Pure and Applied Optics*, 9:103–112.

Carbone, L., Nobile, C., de Giorgi, M., della Sala, F., Morello, G., Pompa, P., Hytch, M., Snoeck, E., Fiore, A., and Franchini, I. (2007). Synthesis and micrometer-scale assembly of colloidal CdSe/CdS nanorods prepared by a seeded growth approach. *Nano Letters*, 7(10):2942–2950.

Chen, X., Nazzal, A., Goorskey, D., Xiao, M., Peng, Z., and Peng, X. (2001). Polarization spectroscopy of single CdSe quantum rods. *Physical Review B*, 64(24):245304.

Daboussi, B. O., Rodrigues-Viejo, J., Mikulec, F. V., Heine, J. R., Mattoussi, H., Ober, R., Jensen, K. F., and Bawendi, M. G. (1997). (CdSe)ZnS Core-Shell Quantum Dots: Synthesis and Characterization of a Size Series of Highly Luminescent Nanocrystallites. *J. Phys. Chem. B*, 101:9463–9475.

Di Corato, R., Quarta, A., Piacenza, P., Ragusa, A., Figuerola, A., Buonsanti, R., Cingolani, R., Manna, L., and Pellegrino, T. (2008). Water solubilization of hydrophobic nanocrystals by means of poly(maleic anhydride-alt-1-octadecene). *Journal of Materials Chemistry*, 18(17):1991–1996.

Engstroem, E., Rahul, P., Persson, M., Goksoer, M., Bertness, K., and Smalyukh, I. (2011). Three-dimensional imaging of liquid crystal structures and defects by means of holographic manipulation of colloidal nanowires with faceted sidewalls. *Soft Matter*, 7:6304–6312.

Frantsuzov, P., Kuno, M., Jankó, B., and Marcus, R. A. (2008). Universal emission intermittency in quantum dots, nanorods and nanowires. *Nature Physics*, 4:1745–2473.

Friese, M. E. J., Nieminen, T. A., Heckenberg, N. R., and Rubinsztein-Dunlop, H. (2003). Optical alignment and spinning of laser-trapped microscopic particles. *Nature*, 394:348–350.

Grier, D. G. (2003). A revolution in optical manipulation. *Nature Photonics*, 424:810–816,.

Gross, P., Laurens, N., Oddershede, L. B., Bockelmann, U., Peterman, E. J. G., and Wuite, G. J. L. (2011). Quantifying how DNA stretches, melts and changes twist under tension. *Nature Physics*, 7:731–736.

Guck, J., Ananthakrishnan, R., Moon, T. j., Cunningham, C., and Kas, J. (2000). Optical deformability of soft biological dielectrics. *Physical Review Letters*, 84:5451–5454.

Harada, Y. and Asakura, T. (1996). Radiation forces on a dielectric sphere in the Rayleigh scattering regime. *Optics Communications*, 124:529–541.

Head, C. R., Kammann, E., Zanella, M., Manna, L., and Lagoudakis, P. G. (2012). Spinning nanorods - active optical manipulation of semiconductor nanorods using polarised light. *Nanoscale*, 4:3693–3697.

Hu, J. (2001). Linearly Polarized Emission from Colloidal Semiconductor Quantum Rods. *Science*, 292(5524):2060–2063.

Jauffred, L. and Oddershede, L. B. (2010). Two-Photon Quantum Dot Excitation during Optical Trapping. *Nano Letters*, 10(5):1927–1930.

Jauffred, L., Richardson, A., and Oddershede, L. (2008). Three-Dimensional Optical Control of Individual Quantum Dots. *Nano Letters*, 8(10):3376–3380.

Jones, P. H., Palmisano, F., Bonaccorso, F., Gucciardi, P. G., Calogero, G., Ferrari, A. C., and Maragó, O. M. (2009). Rotation Detection in Light-Driven Nanorotors. *ACS Nano*, 3(10):3077–3084.

MacDonald, M., Spalding, G., and Dholakia, K. (2003). Microfluidic sorting in an optical lattice. *Nature*, 426(27):421–424.

Meiners, J. C. and Quake, S. (1999). Direct Measurement of Hydrodynamic Cross Correlations between Two Particles in an External Potential. *Physical Review Letters*, 82(10):2211–2214.

Müller, J., Lupton, J. M., Lagoudakis, P. G., Schindler, F., Koeppe, R., Rogach, A. L., Feldmann, J., Talapin, D. V., and Weller, H. (2005). Wave Function Engineering in Elongated Semiconductor Nanocrystals with Heterogeneous Carrier Confinement. *Nano Letters*, 5(10):2044–2049.

Neuman, K. C. and Block, S. M. (2004). Optical trapping. *Review of scientific instruments*, 75(9):2787–2809.

Oddershede, L., Grego, S., Nörrelykke, S. F., and Berg-Sørensen, K. (2000). Optical tweezers: probing biological surfaces. Technical Report NORDITA-2000-46-CM, Copenhagen.

Pauzauskie, P. J., Radenovic, A., Trepagnier, E., Shroff, H., Yang, P., and Liphardt, J. (2006). Optical trapping and integration of semiconductor nanowire assemblies in water. *Nature materials*, 5:97–101.

Peng, X., Schlamp, M. C., Kadavanich, A. V., and Alivisatos, A. P. (1997). Epitaxial Growth of Highly Luminescent CdSe/CdS Core/Shell Nanocrystals with Photostability and Electronic Accessibility. *J. Am. Chem. Soc.*, 119:7019–7029.

Ramachandran, S., Merrill, N., Blick, R., and Weide, D. (2005). Colloidal quantum dots initiating current bursts in lipid bilayers. *Biosensors and Bioelectronics*, 20(10):2173–2176.

Reihani, S. N. S. and Oddershede, L. B. (2007). Optimizing immersion media refractive index improves optical trapping by compensating spherical aberrations. *Optics Letters*, 32(14):1998–2000.

Ruijgrok, P., Verhart, N., Zijlstra, P., Tchebotareva, A., and Orrito, M. (2011). Brownian Fluctuations and Heating of an Optically Aligned Gold Nanorod. *Physics Review Letters*, 107:037401.

Selhuber-Unkel, C., Zins, I., Schubert, O., Sönnichsen, C., and Oddershede, L. B. (2008). Quantitative Optical Trapping of Single Gold Nanorods. *Nano Letters*, 8(9):2998–3003.

Talapin, D. V., Koeppe, R., Götzinger, S., Kornowski, A., Lupton, J. M., Rogach, A. L., Benson, O., Feldmann, J., and Weller, H. (2003). Highly Emissive Colloidal CdSe/CdS heterostructures of mixed dimensionality. *Nano Letters*, 3(12):1677–1681.

Tong, L., Miljković, V. D., and Käll, M. (2010). Alignment, Rotation, and Spinning of Single Plasmonic Nanoparticles and Nanowires Using Polarization Dependent Optical Forces. *Nano Letters*, 10:268–273.

Visscher, K., Gross, S. P., and Block, S. M. (1996). Construction of Multiple-Beam optical traps with nanometer-resolution position sensing. *Journal of selected topics in quantum electronics*, 2(4):1066–1076.

Yu, T., Cheong, F.-C., and Sow, C.-H. (2004). The manipulation and assembly of CuO nanorods with line optical tweezers. *Nanotechnology*, 15(12):1732–1736.

Chapter 3

Vertical external-cavity surface-emitting laser

3.1 Introduction

In this Chapter I shall introduce the concept of the vertical-external-cavity surface-emitting semiconductor laser (VECSEL) and highlight recent milestones of continuous-wave (CW) and mode-locked (ML) operation. In section 3.2 I shall describe each of the individual components necessary to build a mode-locked VECSEL.

VECSELs are lasers that combine the wavelength flexibility of semiconductor materials with high beam quality and high average power. The composition of the semiconductor material and design of the semiconductor wafer allow for a wide range of available lasing wavelengths from 674 nm (Hastie et al., 2005) to 5000 nm (Rahim et al., 2008) while the external cavity makes it possible to have an M^2 value close to 1 (Rudin et al., 2008; Okhotnikov, 2010). The flexibility of the external cavity design allows for the inclusion of intra-cavity elements, such as etalons (Fan et al., 2007) or second harmonic generation crystals (Hastie et al., 2006; Lee et al., 2006) adding further ways to adapt and tune the VECSEL towards the desired output properties.

CW VECSEL technology has matured significantly in the past decade where record average powers of over 100 W have been achieved for spatial multi-mode VECSELs

(Heinen et al., 2012) and 20 W for a TEM_{00} VECSEL (Rudin et al., 2008), predominantly due to efficient thermal management of the VECSEl structures. CW VECSELs are now at a stage that they are commercially available, such as a flexible and low-noise 20 W pump laser for Ti:Sapphire lasers (Coherent, 2013).

It is possible to obtain ultrashort pulses by passively mode-locking VECSELs with semiconductor saturable absorber mirrors (SESAMs) (Keller et al., 1992, 1996), multilayer reflector structures that have a saturable absorber element integrated, either quantum wells (Hoogland et al., 2000), quantum dots (Maas et al., 2008) or graphene (Zaugg et al., 2013b). Due to the short upper-state lifetime, in the nanosecond regime, VECSELs typically operate in the few GHz repetition rate regime (Tropper et al., 2012). However repetition rates ranging from 92 GHz (Klopp et al., 2011) down to 99.6 MHz (Zaugg et al., 2013a) in fundamental operation have been demonstrated. Wilcox et al. (2012) have achieved a repetition rate of up to 175 GHz via harmonic mode-locking, by exploiting the external cavity to introduce a intra-cavity etalon.

At wavelengths around 1 μm pulse durations down to 60 fs for pulse groups (Quarterman et al., 2009) and 106 fs for single pulses (Klopp et al., 2011) have been observed. Although the most significant progress has been made at a wavelength of around 1 μm, VECSELS operating at around 2 μm have obtained pulse durations down to 384 fs demonstrated by Guina et al. (2012) and most recently a ML-VECSEL at 675-nm with a 5-ps pusle duration has been reported (Ranta et al., 2013).

Average powers of up to 5.1 W (Scheller et al., 2012) and pulse durations down to 400 fs have been achieved (Wilcox et al., 2013). Most recently peak powers of up to 13.3 kW (Laurain et al., 2013) have been demonstrated with sub-picosecond pulses. These results show that VECSELS start to approach the performance of fibre and solid-state lasers and could be low cost alternatives. The record for the highest average power mode-locked VECSEL of 6.4 W is held by a MIXSEL, a VECSEL that has the saturable absorber and the gain structure integrated into a single semiconductor chip (Rudin et al., 2010). Keller and Tropper (2006) have written a comprehensive article on the history and mechanisms of passively mode-locked VECSELs.

The recent advances in average power are due to effective processing of the gain samples, where the substrate onto which the components of the gain sample are grown, is removed. Thermal management of both, the gain sample and SESAM, are becoming increasingly more important as the average powers of VECSELs increase (Wilcox et al., 2013). Although significant progress in power scaling of VECSELs has been made, the combination of high average power and pulse durations of $\sim$ 100 fs has not been achieved yet.

VECSELs are so called *class-A* lasers as the upper-state lifetime of the semiconductor gain material is so much shorter than the photon lifetime. This leads to CW-VECSELs having very low noise (Laurain et al., 2010, 2009; Kaspar et al., 2013) and ML-VECSELs having low timing-jitters (Paschotta, 2004; Wilcox et al., 2006; Quarterman et al., 2008; Wittwer et al., 2011) down as low as 60-fs (Wittwer et al., 2013). A further noticeable capability of VECSELs is that, due to the mode-locking dynamics and external cavity, it is possible to continuously tune the repetition rate over a range of several GHz by changing the length of the external cavity. Over a large tuning range the pulse duration and average power stay more or less constant (Wilcox et al., 2011; Sieber et al., 2011) and thus lend themselves for GHz frequency spectroscopy or flexible frequency combs.

In this chapter I will describe the components and typical design considerations for ML-VECSELs. In the following two chapters I will outline my research; in chapter 4 I describe my work on the laser build-up behaviour of VECSELs to improve sample designs for shorter pulse durations and in chapter 5 I present my findings of using a fibre amplified VECSEL to generate supercontinuum for frequency combs.

3.2 VECSEL components

A VECSEL is typically formed by a laser cavity in which one mirror is an active mirror, a semiconductor Bragg reflector with an active region on top containing quantum well-s/dots, referred to as the gain sample/structure. The quantum wells/dots are typically optically pumped. Figure 3.1 a) shows a straight cavity VECSEL consisting of a gain

structure and an output coupler, to form a near-hemispherical cavity. The cavity geometry is adjusted to match the spatial cavity mode on the gain sample with the pump spot to use all the pump power. Okhotnikov (2010, chap. 1) discusses the design of the external cavity and optical pump techniques. The structures used in this thesis are all based on InGaAs/GaAs quantum wells with wavelengths around 1 μm and are pumped by 830- or 808-nm fiberized-diode pumps. As the quantum wells only provide a few percent gain the output coupler has a typical transmission of 0.3 % - 3 %, depending on other intra-cavity elements such as etalons, heat spreaders or a SESAM.

Figures 3.1 b) and c) show the cavity configurations used in this thesis to build passively mode-locked VECESELs, in both cavities a SESAM was introduced into the cavity. In order to achieve mode-locking it is necessary to control the saturation ratio between the SESAM and the gain sample. For most SESAMs this means a smaller spot, higher fluence, is required on the SESAM compared to on the gain sample. In the so-called V-cavity (Figure 3.1 b)) the spot size ratio can be altered by changing the distances between the output coupler and the gain sample, and the gain sample and SESAM. In the Z-cavity (Figure 3.1 c)) the distance between the high reflector and SESAM is varied to change the spot size on the SESAM.

The gain of a VECSEL decreases sharply with increasing temperature, due to the increase of non-radiative carrier recombination rates, thus thermal management is critical for high power operation, > 0.5 W. The samples used in this work are mounted on a copper block with silver paste, which is then fixed to a water-cooled temperature-controlled copper heat sink.

With increasing temperature auger recombinations dominate the carrier behaviour in the gain sample and decreases the laser performance, to the point where lasing ceases, known as the thermal roll-over-point. This can be circumvented by increasing the spot-size on the gain sample. However this increases the threshold at which lasing occurs, as the point of quantum well transparency requires higher pump powers, thus a balance has to be found between a low threshold and a high roll-over point. A detailed discussion of thermal effects and handling strategies in VECSELs can be found in Okhotnikov (2010, chap. 2).

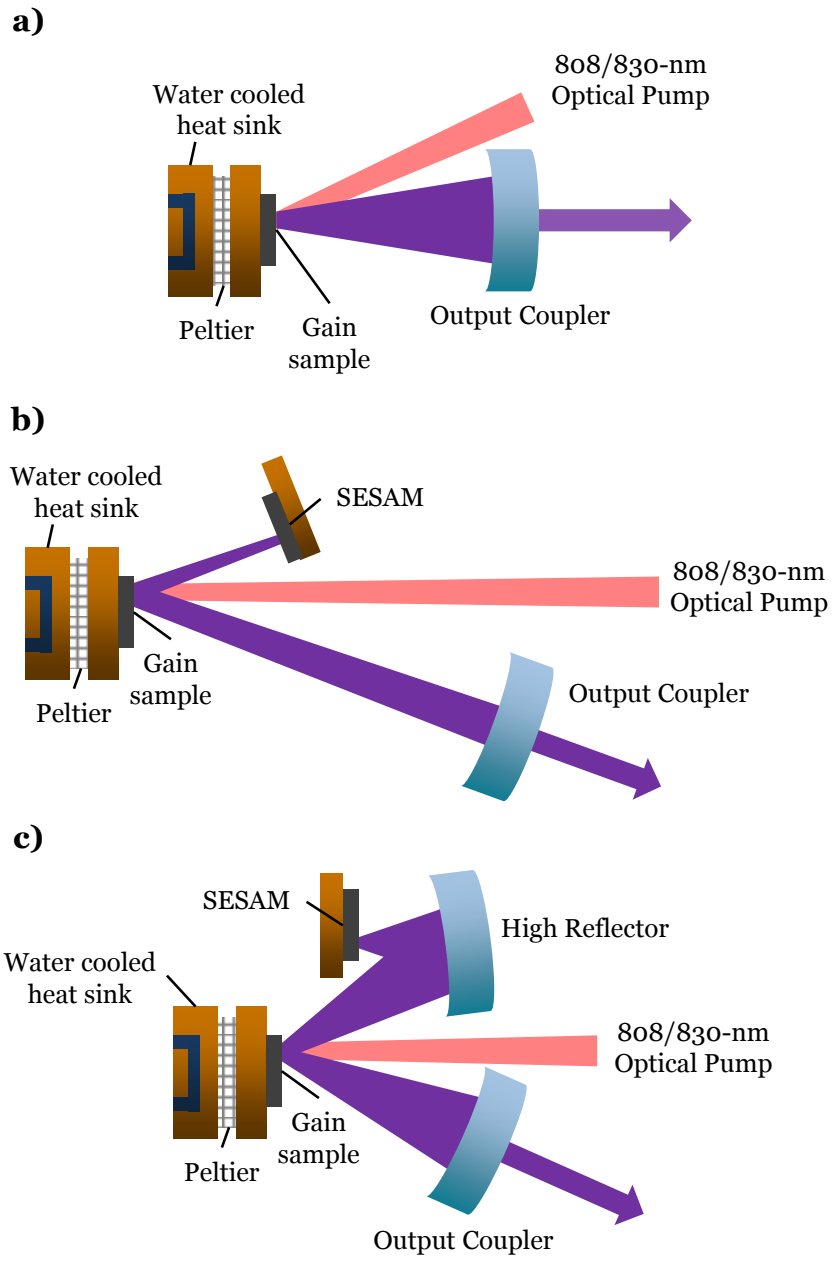

Figure 3.1: VECSEl cavities – a) Straight cavity - The gain sample and the output coupler form a near-hemispherical cavity where the gain sample is pumped by a fibreized-diode laser. b) V-cavity - In this cavity the SESAM is the end mirror and the gain sample acts as a plane folding mirror. By varying the ratio of the distance between the SESAM and the gain sample and the gain sample and the output coupler it is possible to adjust the mode spot size ratio between the gain sample and the SESAM c) Z-cavity - The same can be achieved in the Z-cavity by choosing an appropriate radius of curvature high reflector and adjusting the distance between it and the SESAM. To control the temperature of the gain sample it is mounted on a peltier-controlled water-cooled copper heat sink.

3.2.1 Gain structure

The gain sample itself consists of a substrate, a passive distributed Bragg reflector (DBR) and an active region (Figure 3.2). A capping layer is used to protect the aluminium-containing parts of the structure against oxidisation. The reflection of the DBR sets up a standing wave in the microcavity formed by the active region. The active region is made up of pump-absorbing layers, which also act as barriers for the quantum wells, the quantum wells which are strategically placed at antinodes of the standing wave to enhance the interaction with the electric field, and the window layer, which controls the microcavity field enhancement.

Critical criteria for VECSEL gain chip design are the effective gain bandwidth and longitudinal confinement factor (LCF). These are both controlled by the layer design of the semiconductor chip. The LCF gives the enhancement of the gain of the quantum wells due to their position in respect to the standing wave and is thus wavelength dependent and introduces a spectral filter.

Figure 3.2 A) shows the form of the standing wave in a resonant gain structure of the type used to demonstrate 100-W operation. The quantum wells are placed at anti-nodes to increase the electric field – quantum well interaction. The window layer thickness is so that, for the design wavelength, the boundary between the window layer and air aligns with an antinode of the standing wave and thus there is hardly any intensity reduction of the electric field in the transition. Both effects combined provide optimum gain for the design wavelength. For longer/shorter wavelengths, however, the quantum well– electric field interaction and the transmission at the boundary of the air – window layer interface decrease and thus the gain decreases sharply for wavelengths other than the design wavelength.

Figures 3.2 B) & C) show two gain structure designs and their resulting standing waves used for mode-locked VECSELs to achieve femtosecond pulse durations. Figure 3.2 B) shows the so called anti-resonant design, which has the quantum wells at antinodes of the standing-wave, however the window layer thickness is such that there is a node at the air – window layer interface. This design reduces the electric field intensity to about 1/10

inside the structure compared to the intensity in air. However the transmission at the air – window layer increases for wavelengths longer/shorter than the design wavelength and thus the overall effect results in a broader more even gain spectrum compared to the resonant structure design.

Figure 3.2 C) shows an alternative to the anti-resonant design, where a single layer anti-reflection (AR) coating on top of a resonant sample is used to reduce the spectral filtering of the gain sample. The electric field intensity inside the microcavity is about 1/3 compared to in air and thus AR coated samples provide more gain than the anti-resonant structures. However a further important characteristic of gain samples to consider for mode-locking is the group delay dispersion (GDD), which can lengthen the pulse duration.

Figure 3.3 shows the dispersion profile for the resonant, anti-resonant and AR-coated gain sample designs used in Figure 3.2. The resonant design, has a significantly higher GDD from -4000 to +4000 fs^2 around the design wavelength compared to the GDD of the anti-resonant, < 100 fs^2, and the AR-coated design, ~ 100 fs^2. the resonant design should be avoided to mode-lock VECSELs due to it's high dispersion and gain filtering. Even though the dispersion of the anti-resonant design is less around the design wavelengths it varies significantly more for broader wavelength ranges than the dispersion of the AR-coated design, which varies by only ~ 50 fs^2 compared to ~ 400 fs^2 over 30 nm.

Whether the anti-resonant, with a broader and more even spectral filter, or the AR-coated resonant design, with more gain and a more even dispersion, is better for mode-locked VECSELs is being heavily investigated. It is thought that for pulse durations below 100 fs dispersion becomes the more significant pulse lengthening effect, however the spectral filter needs to be weak enough to support a broad enough spectrum. The 60-fs pulse group result by Quarterman et al. (2009) used an anti-resonant design whereas the 107-fs single pulse result by Klopp et al. (2011) used an AR-coated structure.

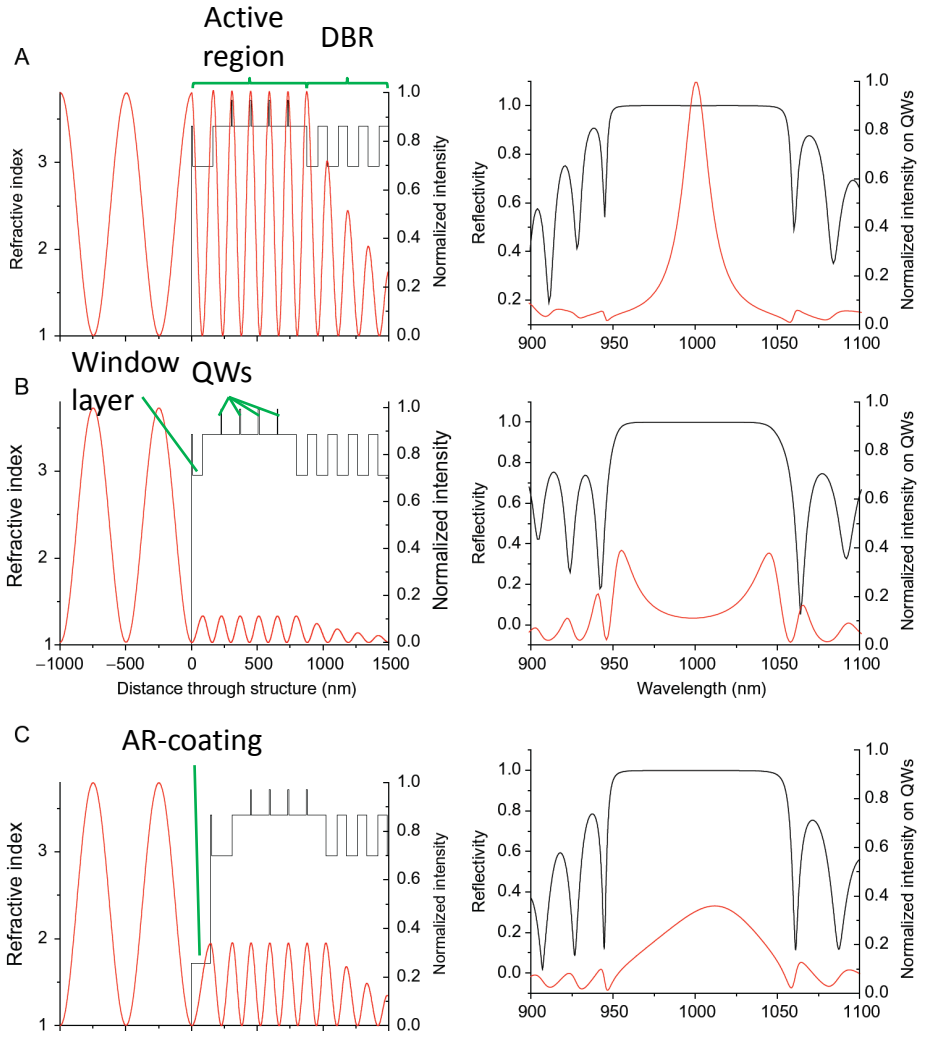

Figure 3.2: Gain structure designs – Spectral characteristics of a VECSEL chip with a design wavelength of 1000 nm for a A) resonant design, B) anti-resonant design and C) anti-reflection-coated resonant design. The left plots show the refractive index and standing wave intensity as a function of distance through the structure. The right plots show the calculated reflectivity and longitudinal confinement factor as a function of wavelength. Figure obtained from (Tropper et al., 2012)

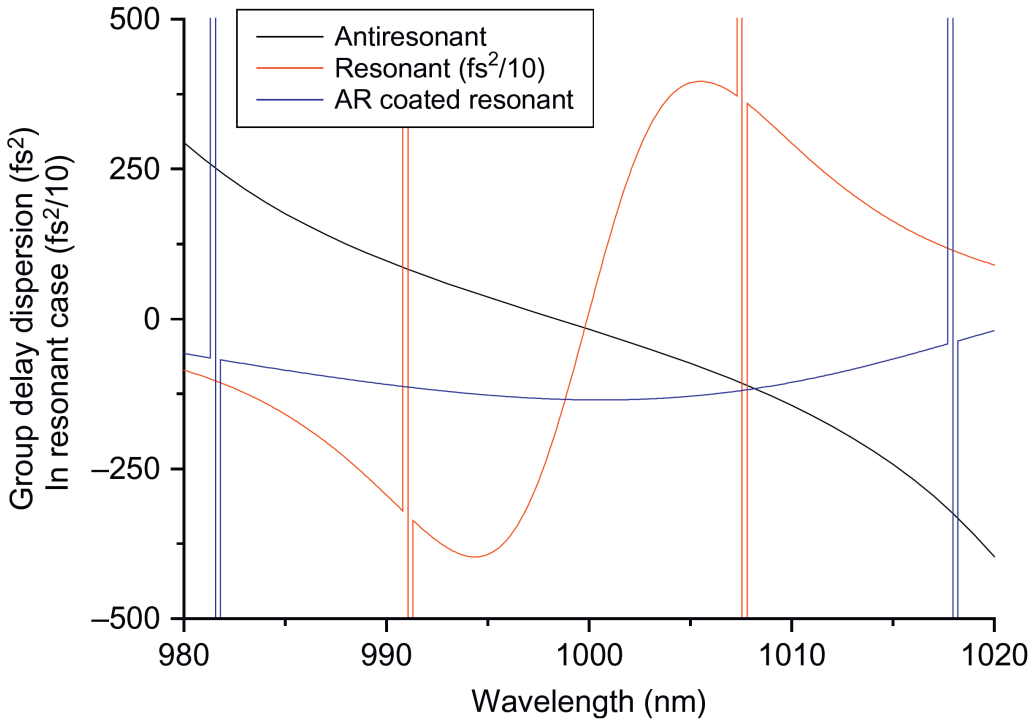

Figure 3.3: Group delay dispersion – GDD as a function of wavelength for resonant, antiresonant and anti-reflection-coated resonant gain structure design of Figure 3.2. Figure obtained from (Tropper et al., 2012)

3.2.2 SESAM mode-locking

The Keller group at ETH Zürich have driven the development and characterisation of SESAMs (Keller et al., 1996; Keller, 1998; Haiml et al., 2004; Grange et al., 2005). I will only provide a brief overview of important characteristics of SESAMs and their use to mode-lock VECSLs in this section.

The SESAM is a semiconductor multilayer reflector structure with an integrated saturable aborber element, such as quantum well(s) or dots. In contrast to the gain sample the quantum wells are unpumped and absorb light and introduce cavity loss. The absorption, however, can be saturated by a sufficiently high intracavity fluence, thus bleaching the quantum wells and increasing the reflectivity of the SESAM. The difference in reflectivity from low fluences to high fluences is known as the modulation depth of a SESAM where the fluence at which the reflectivity has incresed by $\Delta R/e$ is referred to as the saturation fluence.

In a roundtrip in the laser cavity the pulses are temporally stretched by the spectral filter of the gain sample and shortened by the absorption in the SESAM. Thus when designing the SESAM the modulation depth and saturation fluence need to be appropriately chosen with respect to the gain structure and its gain and dispersion characteristics, and the desired laser repetition rate and output power.

The duration of the pulses produced depend most significantly on the recovery time of the absorber, which is typically split into two components; a slow component due to carrier recombination and a fast component due to carrier scattering, carrier trapping at defect sites and thermalization. As VECSELs operate at repetition rates of a few GHz the recovery of the absorber must be able to recover in tens of picoseconds. As semiconductor quantum wells have nanosecond carrier recombination periods they seem unsuitable. The recombination can be sped up by introducing defects, however those may introduce more non-saturable losses.

An alternative design to speed up the recovery time is the so-called surface-recombination SESAM, which has a quantum well grown close, ~ 2 nm, to the surface. This creates an additional recovery channel via tunnelling to defect states on the surface, hence the

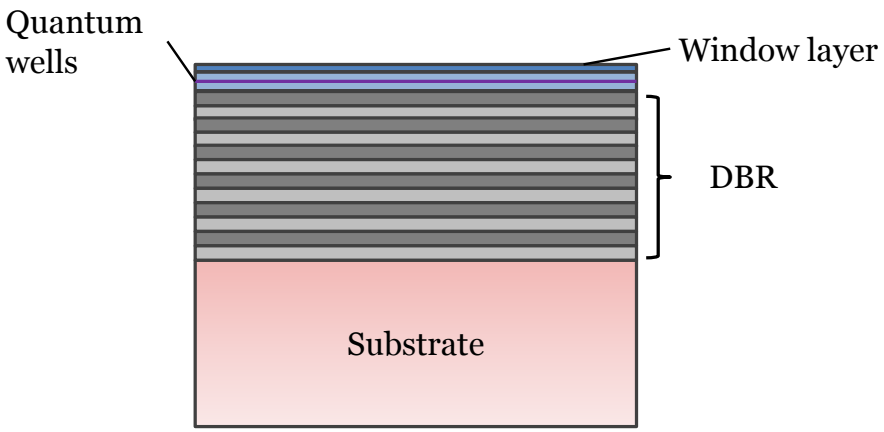

Figure 3.4: SESAM sample schematic – The SESAM, similar to the gain sample, consists of a substrate, a passive distributed Bragg reflector (DBR) and a region containing the quantum well(s), which act as the saturable absorber.

name. Due to the small thickness of the layer the defects introduced are distributed in an approximately 2-dimensional plane and thus minimizing the introduction of non-saturable losses. This surface-recombination SESAM has so-far produced the shortest pulses in mode-locked VECSELs (Quarterman et al., 2009; Klopp et al., 2011).

Soliton-*like* pulse-shaping mechanisms are important too when designing SESAM structures to passively mode-lock VECSELs (Paschotta et al., 2002; Hoffman et al., 2010; Sieber et al., 2013). Similar to the design of gain structures the GDD should be as even as possible over a broad range of wavelengths. Furthermore Sieber et al. (2013) found that in order to balance the phase change of the pulse due to saturation of the gain and absorber it is neccessary to have a slightly positive GDD in the cavity, which can be achieved by using a similar AR-coating as for the gain sample.

References

Coherent (2013). *Verdi G-Series*. http://www.coherent.com/downloads/Verdi_GseriesFamily_DSrevD_0313_5.pdf.

Fan, L., Fallahi, M., Zakharian, A. R., Hader, J., Moloney, J. V., Bedford, R., Murray, J. T., Stolz, W., and Koch, S. W. (2007). Extended Tunability in a Two-Chip VECSEL. *Photonics Technology Letters*, 19(8):544–546.

Grange, R., Haiml, M., Paschotta, R., Phühler, G., Krainer, L., Golling, M., Ostinelli, O., and Keller, U. (2005). New regime of inverse saturable absorption for self-stabilizing passively mode-locked lasers. *Applied Physics B*, 80(2):151–158.

Guina, M., Härkönen, A., Paajaste, J., Alanko, J.-P., Suomalainen, S., Grebing, C., and Steinmeyer, G. (2012). Passively mode-locked GaSb-based VECSELs emitting sub-400-fs pulses at 2 μm. *Proceedings of the SPIE*, 8242:824204.

Haiml, M., Grange, R., and Keller, U. (2004). Optical characterization of semiconductor saturable absorbers. *Applied Physics B*, 79(3):331–339.

Hastie, J., Calvez, S., Dawson, M., Leinonen, T., Laakso, A., Lyytikäinen, J., and Pessa, M. (2005). High power CW red VECSEL with linearly polarized TEM00 output beam. *Optics Express*, 13(1):77–81.

Hastie, J. E., Morton, L. G., Kemp, A. J., Dawson, M. D., Krysa, A. B., and Roberts, J. S. (2006). Tunable ultraviolet output from an intracavity frequency-doubled red vertical-external-cavity surface-emitting laser. *Applied Physics Letters*, 89(6):061114.

Heinen, B., Wang, T.-L., Sparenberg, M., Weber, A., Kunert, B., Hader, J., Koch, S. W., Moloney, J. V., Koch, M., and Stolz, W. (2012). 106 W continuous-wave

output power from vertical-external-cavity surface-emitting laser. *Electronics Letters*, 48(9):516–517.

Hoffman, M., Sieber, O. D., Maas, D. J. H. C., Wittwer, V. J., Golling, M., Südmeyer, T., and Keller, U. (2010). Experimental verification of soliton-like pulseshaping mechanisms in passively mode-locked VECSELs. *Optics Express*, 18(10):10143–10153.

Hoogland, S., Dhanjal, S., Tropper, A. C., Roberts, J. S., Häring, R., Paschotta, R., and Keller, U. (2000). Passively Mode-Locked Diode-Pumped Surface-Emitting Semiconductor Laser. *Photonics Technology Letters*, 12(9):1135–1137.

Kaspar, S., Rattunde, M., Topper, T., Rosener, B., Manz, C., Kohler, K., and Wagner, J. (2013). Linewidth Narrowing and Power Scaling of Single-Frequency 2.X μm GaSb-Based Semiconductor Disk Lasers. *Quantum Electronics*, 49(3):314–324.

Keller, U. (1998). Chapter 4 Semiconductor Nonlinearities for Solid-State Laser Modelocking and Q-Switching . In Garmire, E. and Kost, A., editors, *Nonlinear Optics in Semiconductors II*, volume 59 of *Semiconductors and Semimetals*, pages 211 – 286. Elsevier.

Keller, U., Miller, D. A. B., Boyd, G. D., Chiu, T. H., Ferguson, J. F., and Asom, M. T. (1992). Solid-state low-loss intracavity saturable absorber for Nd:YLF lasers: an antiresonant semiconductor Fabry-Perot saturable absorber. *Optics Letters*, 17(7):505–507.

Keller, U. and Tropper, A. C. (2006). Passively modelocked surface-emitting semiconductor lasers. *Physics Reports*, 429(2):67–120.

Keller, U., Weingarten, K. J., Kartner, F. X., Kopf, D., Braun, B., Jung, I. D., Fluck, R., Honninger, C., Matuschek, N., and Aus der Au, J. (1996). Semiconductor saturable absorber mirrors (SESAM's) for femtosecond to nanosecond pulse generation in solid-state lasers. *Selected Topics in Quantum Electronics*, 2(3):435–453.

Klopp, P., Griebner, U., Zorn, M., and Weyers, M. (2011). Pulse repetition rate up to 92 GHz or pulse duration shorter than 110 fs from a mode-locked semiconductor disk laser. *Applied Physics Letters*, 98(7):071103.

Laurain, A., Myara, M., Beaudoin, G., Sagnes, I., and Garnache, A. (2009). High power single-frequency continuously-tunable compact extended-cavity semiconductor laser. *Optics Express*, 17(12):9503–9508.

Laurain, A., Myara, M., Beaudoin, G., Sagnes, I., and Garnache, A. (2010). Multiwatt-power highly-coherent compact single-frequency tunable Vertical-External-Cavity-Surface-Emitting-Semiconductor-Laser. *Optics Express*, 18(14):14627–14636.

Laurain, A., Scheller, M., Wang, T.-L., Hader, J., Moloney, J. V., Heinen, B., Kunert, B., and Stolz, W. (2013). Recent advances in power scaling of high-power optically-pumped semiconductor lasers for ultrashort pulse generation and continuous wave single frequency operation. *Proc. SPIE 8733, Laser Technology for Defense and Security IX*, page 873303.

Lee, J., Lee, S., Kim, T., and Park, Y. (2006). 7 W high-efficiency continuous-wave green light generation by intracavity frequency doubling of an end-pumped vertical external-cavity surface emitting semiconductor laser. *Applied Physics Letters*, 89(24):241107.

Maas, D. J. H. C., Bellancourt, A. R., Hoffmann, M., Rudin, B., Barbarin, Y., Golling, M., Südmeyer, T., and Keller, U. (2008). Growth parameter optimization for fast quantum dot SESAMs. *Optics Express*, 16(23):18646–18656.

Okhotnikov, O. (2010). *Semiconductor Disk Lasers*. Wiley-VCH.

Paschotta, R. (2004). Noise of mode-locked lasers (Part II): timing jitter and other fluctuations. *Applied Physics B*, 79:163–173.

Paschotta, R., Häring, R., Garnache, A., Hoogland, S., Tropper, A., and Keller, U. (2002). Soliton-like pulse-shaping mechanism in passively mode-locked surface-emitting semiconductor lasers. *Applied Physics B*, 75:445–451.

Quarterman, A. H., Wilcox, K. G., Apostolopoulos, V., Mihoubi, Z., Elsemere, S. P., Farrer, I., Ritchie, D. A., and Tropper, A. c. (2009). A passively mode-locked external-cavity semiconductor laser emitting 60-fs pulses. *Nature Photonics*, 3:729–731.

Quarterman, A. H., Wilcox, K. G., Elsemere, S., Mihoubi, Z., and Tropper, A. C. (2008). Active stabilisation and timing jitter characterisation of sub-500 fs pulse passively modelocked VECSEL. *Electronics Letters*, 44(19):1135–1137.

Rahim, M., Felder, F., Fill, M., Zogg, H., and Vi, I. V. (2008). Optically pumped 5 m IV-VI VECSEL with Al-heat spreader. *Optics Letters*, 33(24):3010–3012.

Ranta, S., Härkönen, A., Leinonen, T., Orsilla, L., Lyytikäinen, J., Steinmeyer, G., and Guina, M. (2013). Mode-locked VECSEL emitting 5 ps pulses at 675 nm. *Optics Letters*, 38(13):2289–2291.

Rudin, B., Rutz, A., Hoffmann, M., Maas, D., Bellancourt, A., Gini, E., Südmeyer, and Keller, U. (2008). Highly efficient optically pumped vertical-emitting semiconductor laser with more than 20 W average output power in a fundamental transverse mode. *Optics Letters*, 33(22):2719–2721.

Rudin, B., Wittwer, V. J., Maas, D. J. H. C., Hoffmann, M., Sieber, O. D., Barbarin, Y., Golling, M., Südmeyer, T., and Keller, U. (2010). High-power MIXSEL: an integrated ultrafast semiconductor laser with 6.4 W average power. *Optics Express*, 18(26):27582–27588.

Scheller, M., Wang, T.-L., Kunert, B., Stolz, W., Koch, S. W., and Moloney, J. V. (2012). Passively modelocked VECSEL emitting 682 fs pulses with 5.1W of average output power. *Electronics Letters*, 48(10):588–589.

Sieber, O. D., Hoffman, M., Wittwer, V. J., Mangold, M., Golling, M., Tilma, B. W., Südmeyer, T., and Keller, U. (2013). Experimentally veried pulse formation model for high-power femtosecond VECSELs. *Applied Physics B*, pages 1–13.

Sieber, O. D., Wittwer, V. J., Mangold, M., Hoffmann, M., Golling, M Südmeyer, T., and Keller, U. (2011). Femtosecond VECSEL with tunable multigigahertz repetition rate. *Optics Express*, 19(23):23538–23543.

Tropper, A. C., Quarterman, A. H., and Wilcox, K. G. (2012). *Advances in Semiconductor Lasers: Ultrafast Vertical-External-Cavity Surface-Emitting Semiconductor Lasers*, volume 86. Academic Press, Burlington, USA. 269–300.

Wilcox, K. G., Foreman, H. D., Roberts, J. S., and Tropper, A. C. (2006). Timing jitter of 897 MHz optical pulse train from actively stabilised passively modelocked surface-emitting semiconductor laser. *Electronics Letters*, 42(3):159–160.

Wilcox, K. G., Quarterman, A. H., Apostolopoulos, V., Beere, H. E., Farrer, I., Ritchie, D. A., and Tropper, A. C. (2012). 175 GHz, 400-fs-pulse harmonically mode-locked surface emitting semiconductor laser. *Optics Express*, 20(7):7040–7045.

Wilcox, K. G., Quarterman, A. H., Beere, H. E., Ritchie, D. A., and Tropper, A. C. (2011). Variable repetition frequency femtosecond-pulse surface emitting semiconductor laser. *Applied Physics Letters*, 99:131107.

Wilcox, K. G., Tropper, A. C., Beere, H. E., Ritchie, D. A., Kunert, B., Heinen, B., and Stolz, W. (2013). 4.35 kW peak power femtosecond pulse mode-locked VECSEL for supercontinuum generation. *Optics Express*, 21(2):1599–1605.

Wittwer, V. J., van der Linden, R., Tilma, B. W., Resan, B., Weingarten, K. J., Südmeyer, T., and Keller, U. (2013). Sub-60-fs Timing Jitter of a SESAM Mode-locked VECSEL. *Photonics Journal*, 5(1):1400107.

Wittwer, V. J., Zaugg, C. A., Pallmann, W. P., Oehler, A. E. H., Rudin, B., Hoffmann, M., Golling, M., Barbarin, Y., Südmeyer, T., and Keller, U. (2011). Timing Jitter Characterization of a Free-Running SESAM Mode-locked VECSEL. *Photonics Journal*, 3(4):658–664.

Zaugg, C. A., Klenner, A., Sieber, O. D., Golling, M., Tilma, B. W., and Keller, U. (2013a). Sub-100 MHz Passively Modelocked VECSEL. *CLEO US 2013*. CW1G.6.

Zaugg, C. A., Sun, Z., Popa, D., Milana, S., Kulmala, T., Sundraram, R. S., Wittwer, V. J., Mangold, M., Sieber, O. D., Golling, M., Lee, Y., Ahn, J. H., Ferrari, A. C., and Keller, U. (2013b). Wavelength Tunable Graphene Modelocked VECSEL. *CLEO US 2013*. CW1G.4.

Chapter 4

Experimental measurements of lasing onset characteristics

4.1 Introduction

In this chapter I describe my work on the laser onset behaviour of VECSELs to extract the internal losses and the curvature of their gain spectrum, which defines the demands on the SESAM to generate ultrashort pulses.

The traditional Findlay-Clay method to determine the internal losses of a 4-level laser requires several different lasers to be built, each with a different output coupling (Findlay and Clay, 1966). It is an assumption of the method that these cavities are aligned identically (or more precisely, that any differences between the alignment losses of the different cavities are small compared to the output coupling), so that the output coupling is the only variable which is changed. This can be challenging in practice, particularly in the case of low gain lasers like VECSELs, where even small differences in loss resulting from misalignment may corrupt the analysis.

In order to optimize the design of VECSELs for continuous-wave and mode-locked operation it is essential to control the magnitude, spectrum and saturation behaviour of the semiconductor gain. However as the gain of a single quantum well is determined by a multitude of factors such as its well thickness, the band structure of the well and the

barriers, carrier population, temperature and the interaction of light and the carriers as determined by the longitudinal confinement factor (Coldren and Corzine, 1995), calculating the gain is non-trivial. Especially for structures with multiple quantum wells, where these properties are likely to be different for each well, calculations can only be used as estimates and experimental techniques are required.

Coldren and Corzine (1995), who were looking at edge-emitting laser diodes and vertical-cavity surface-emitting lasers (VCSELs), have done comprehensive work to determine gain parameters for semiconductor lasers, experimentally and theoretically, on which Kuznetsov et al. (1999) drew to present an empirical model for an InGaAs/GaAs VECSEL and used it to estimate the optimum numbers of quantum wells for high power operation, assuming a logarithmic dependence of the quantum well gain, g, on the carrier density, N,

$$g = g_0 \; ln(N/N_0). \tag{4.1}$$

In 2007 Moloney et al. (2007) have developed a microscopic model with many-body physics, such as coloumb interactions, instead of rate equations with phenomenlogical time constants to model the gain and design VECSELs. This microscopic-model approach has been further developed since by Hader et al. (2010) and has been used to improve the external efficiency of VECSELs (Hader et al., 2011). However due to the required computational capabilities the microscopic model is only of limited use to model transient behaviours and several experimental methods have been developed to obtain gain characteristics of VECSEL gain structures.

Borgentun et al. (2011) developed a CW-reflectivity measurement technique, which was able to determine the small-signal gain and gain bandwidth for a single pass through a gain structure. Using this technique an anti-resonant gain structure was investigated, which exhibited an almost constant gain of 3 % over 35 nm. More recently Mangold et al. (2012) provided a further improvement of the gain characterisation of VECSELs by using a saturation fluence measurement technique to obtain the saturation fluences of AR-coated VECSEL gain structures to be around 30-80 μJ/cm^2.

To investigate the transient behaviour of a VECSEL Diehl et al. (2007) used a streak camera to resolve the laser power build-up and photoluminescence (PL) behaviour on the nanosecond scale, where a 500-ns pulsed laser was used to pump the gain. Furthermore Diehl et al. (2007) showed that the general rate equations were able to predict and model the transient behaviour at early times. A shift of the lasing spectrum during power build-up was observed, which was attributed to heating of the lasing structure as the pump pulse was absorbed. El Amili et al. (2012) used the laser power build-up transients to verify the *class-A* like behaviour of VECSELs by investigating the delayed threshold phenomena.

Barnes et al. (2010) employed a spectro-temporal approach, a forerunner of the work presented in this thesis, where an acousto-optic modulator (AOM) was used to deflect the laser emission onto a spectrometer at various times following lasing onset and thus allowed for the observation of resolved the spectral behaviour following the VECSEL onset. The narrowing of the spectrum, known as spectral condensation, was used to determine the spectral gain filter of the VECSEL structure under operating conditions. However, due to the response time of the AOM, this spectro-temporal technique had a low time resolution of 3.75 μs and was unable to acquire data for very early times, < 18 μs, after lasing onset.

In this section I will present my investigation into the transient behaviour of the intra-cavity power build-up and PL behaviour which in combination with each other allow for the extraction of the total cavity loss, due to the class-A laser characteristics. Furthermore a novel tempo-spectral technique, which enables the observation of the spectral behaviour from within the first microsecond of lasing onset for ~ 100 μs with a time resolution of 32 ns, will be presented. By analysing the measured spectral condensation it is possible to observe the evolution of the gain spectrum and obtain the spectral filter of a gain structure under operating conditions, which will be demonstrated for two structures; one with a resonant and one with a near anti-resonant design.

4.2 Theory

4.2.1 Semiconductor gain properties

In order to interpret the laser power build-up transient a rate equation model is necessary. The model needs to describe the relationship between the pump rate, carrier density and intracavity power. Where the latter two are influenced by many body effects, the band structure of the semiconductor and quantum confinement in the quantum wells. Chow and Koch (1999) and Haug and Koch (2004) provide two comprehensive books on the optical properties of semiconductors as lasing media.

The laser transients can be described by equations 4.2 and 4.3, using just two dynamical variables; the total number of electron hole pairs in the gain region, N, and the total number of photons in the laser cavity ,Φ,

$$\frac{d\Phi}{dt} = G(N)\Phi - \frac{\Phi}{\tau_c} \tag{4.2}$$

and

$$\frac{dN}{dt} = \Pi - G(N)\Phi - (aN + bN^2 + cN^3). \tag{4.3}$$

$G(N)$ is the modal gain, which can be approximated as a logarithmic gain (Kuznetsov et al., 1999). However we have not made any assumptions for the dependency of the modal gain, as in our method it is replaced by experimental data and thus no analytic form for the gain is required. We do assume, however, that the modal gain is hysteresis free.

Π is the pumping rate, which is constant as we are pumping the quantum wells before and during lasing, thus we assume that the temperature in the semiconductor is constant when lasing starts, too. Furthermore we assume that the carrier populations are homogeneously distributed between the quantum wells, as we operate well above threshold.

a, b and c are related to the defect, spontaneous emission and Auger recombination processes, respectively. When the semiconductor is pumped carriers, electrons, are moved

from the valence to the conduction band. From there the excited carriers can decay radiatively or non-radiatively, where both processes typically takes place on approximately a nanosecond, the time-scale of the carrier lifetime (Kuznetsov et al., 1999). The carrier population increases with increasing pump rate, however it is reduced due to the radiative and non-radiative recombination processes. The radiative recombination channel, the rate of spontaneous emission, is proportional to the carrier density squared. The two main non-radiative recombination processes are recombination at defect site and Auger recombination. Recombination due to defects depends linearly on the carrier density, whereas the recombination through Auger recombination, a carrier-carrier scattering effect where a third carrier is required to be present to conserve energy and momentum when two carriers recombine, is dependent on the cube of the carrier density. However Hader et al. (2010) have found, via microscopic modelling, that the Auger recombination dependency changes to an approximately squared dependency at very high pump densities. Typical numbers for the a, b and c recombination coefficients can be found in Kuznetsov et al. (1999)

τ_c is the cavity photon lifetime, which expresses the rate at which photons are lost from the cavity. Thus it is possible to calculate the total loss of a cavity if the photon cavity roundtrip time and cavity photon lifetime is known:

$$\text{Cavity loss} = \frac{\text{cavity roundtrip time}}{\text{cavity photon lifetime}}. \tag{4.4}$$

4.2.2 Cavity loss extraction

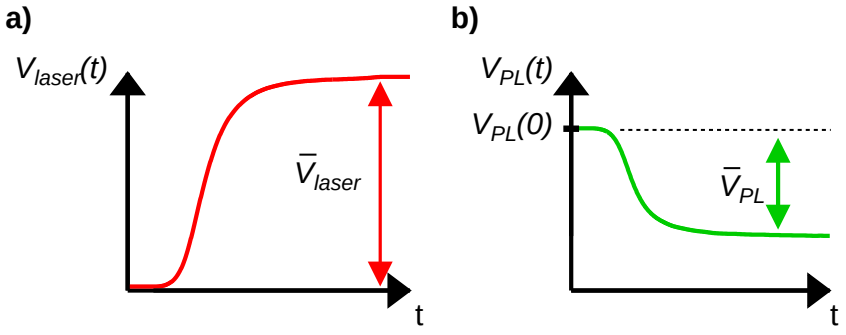

Figure 4.1: Schematics of intra-cavity power build-up and photoluminescence (PL) measurements – a) The intra-cavity power starts building up from zero to a steady state value ($\overline{V}_{laser}$). b) The PL starts at $V_{PL}(0)$ and drops to a steady state at a lower level, the difference between the steady state and the inital value before lasing onset is denoted as $\overline{V}_{PL}$.

Figure 4.1 shows schematics of our measurements of the a) intra-cavity power build-up transient and b) photo luminescence decay, where $V_{laser}(t)$ is the output power of the laser measured with a photodiode and $V_{PL}(t)$ is the signal from a photodiode collecting PL from the laser active region off-axis. From $V_{laser}(t)$ and $V_{PL}(t)$ we can define dimensionless normalized transient equations 4.5 and 4.6 characterising the power build-up and PL, respectively, using

$$f_{laser}(t) = \frac{V_{laser}(t)}{\overline{V}_{laser}}, \tag{4.5}$$

where $\overline{V}_{laser}$ is the steady state value and

$$f_{PL}(t) = \frac{V_{PL}(0) - V_{PL}(t)}{\overline{V}_{PL}}, \tag{4.6}$$

where $\overline{V}_{PL}$ is the difference between the initial value before lasing onset ($V_{PL}(0)$) and the steady state value of the PL.

The typical cavity photon lifetime for a VECSEL, $\sim$ microseconds, is much greater than the carrier lifetime, $\sim$ nanoseconds, and thus it is assumed that the carrier population follows the cavity photon population adiabatically, a so-called class-A laser. This means that in equation 4.3 we can set $\frac{dN}{dt} \approx 0$.

We assume that the carrier recombination in VECSELs is dominated by the radiative recombination process, spontaneous emission. Using Kuznetsov et al. (1999) quoted a, b and c coefficients to calculate the carrier losses we obtain that ~ 85 % of the carrier losses are due to spontaneous emission. Furthermore Hader et al. (2010) have also found, via microscopic modelling, that spontaneous emission dominates the recombination processes and thus we can reduce the last term in equation 4.3 to (bN^2) and can rearrange to give us:

$$V_{PL}(t) = \gamma b N^2 \approx \gamma(\Pi - G(N)\Phi) \tag{4.7}$$

where γ is a constant of proportionality describing the photodiode sensitivity. As the PL intensity before lasing is defined by the pumping rate, $V_{PL}(0) = \gamma\Pi$, we can further say that

$$V_{PL}(0) - V_{PL}(t) = \gamma G(N)\Phi = \overline{V}_{PL} f_{PL}(t). \tag{4.8}$$

Substituting equation 4.8 into equation 4.2 we obtain

$$\frac{d\Phi}{dt} = \frac{\overline{V}_{PL}}{\gamma} f_{PL} - \frac{\Phi}{\tau_c}. \tag{4.9}$$

As the power measured directly follows the number of photons in the cavity we can write

$$f_{laser}(t) = \frac{V_{laser}(t)}{\overline{V}_{laser}} = \frac{\Phi(t)}{\overline{\Phi}}, \tag{4.10}$$

which we can combine with equation 4.9 and the steady state photon number, $\overline{\Phi} = \frac{\overline{V}_{PL}\tau_c}{\gamma}$, to give us

$$\frac{df_{laser}(t)}{dt} + \frac{f_{laser}(t)}{\tau_c} = \frac{f_{PL}(t)}{\tau_c}, \tag{4.11}$$

which has the integral given in equation 4.12.

$$f_{laser}(t) = \frac{1}{\tau_c} \int_o^t f_{PL}(t')\, e^{\left(\frac{t'-t}{\tau_c}\right)} dt' \tag{4.12}$$

To summarize: in this dynamical limit, where the carrier population is adiabatically following the photon number, the laser cavity is acting like a capacitor, smoothing and delaying the population inversion with the cavity lifetime. The cavity lifetime can thus

be extracted rearranging equation 4.11 for τ_c

$$\tau_c(t) = \frac{f_{PL}(t) - f_{laser}(t)}{\frac{df_{laser}(t)}{dt}} \tag{4.13}$$

4.3 Experimental methods

4.3.1 Gain structures

Two gain structures were used in this work, which were designed by W. Stolz, grown by B. Kunert and processed by B. Heinen at NASP III/V, Marburg. Both structures consisted of a 6-λ-thick active region at 1010 nm, containing 10 InGaAs QWs with GaAsP barriers, emitting at 1000 nm at low excitation. A 23 pair $Al_{0.2}Ga_{0.8}As$/AlAs distributed Bragg reflector (DBR) centered at 1010 nm completed the structures. The structures were bonded by solid-liquid inter-diffusion bonding onto a diamond heat spreader before chemical etching to remove the substrate (Bernstein, 1966). The InGaP cap of the resonant sample was left with its original thickness of $\lambda/2$. The InGaP cap of the second sample was chemically etched to a thickness of 1.25 $\lambda/4$, a near anti-resonant design. Schematics of the resonant and near-antiresonant structures are shown in Fig. 4.2 a) and b). By etching the cap to near-antiresonance, the spectral filter from the microcavity is significantly reduced, but the overall modal intensity overlap is also reduced by a factor of ten at the design wavelength as shown in Fig. 4.2 c). This reduction of the gain filtering and corresponding increase of the gain bandwidth of the structure, combined with the low device dispersion associated with the near-antiresonant design (Fig. 4.2 d)), enables short pulse operation to be achieved. The relative advantages and disadvantages of resonant, antiresonant and dielectric antireflection coated resonant structures are described in detail in section 3.2.1.

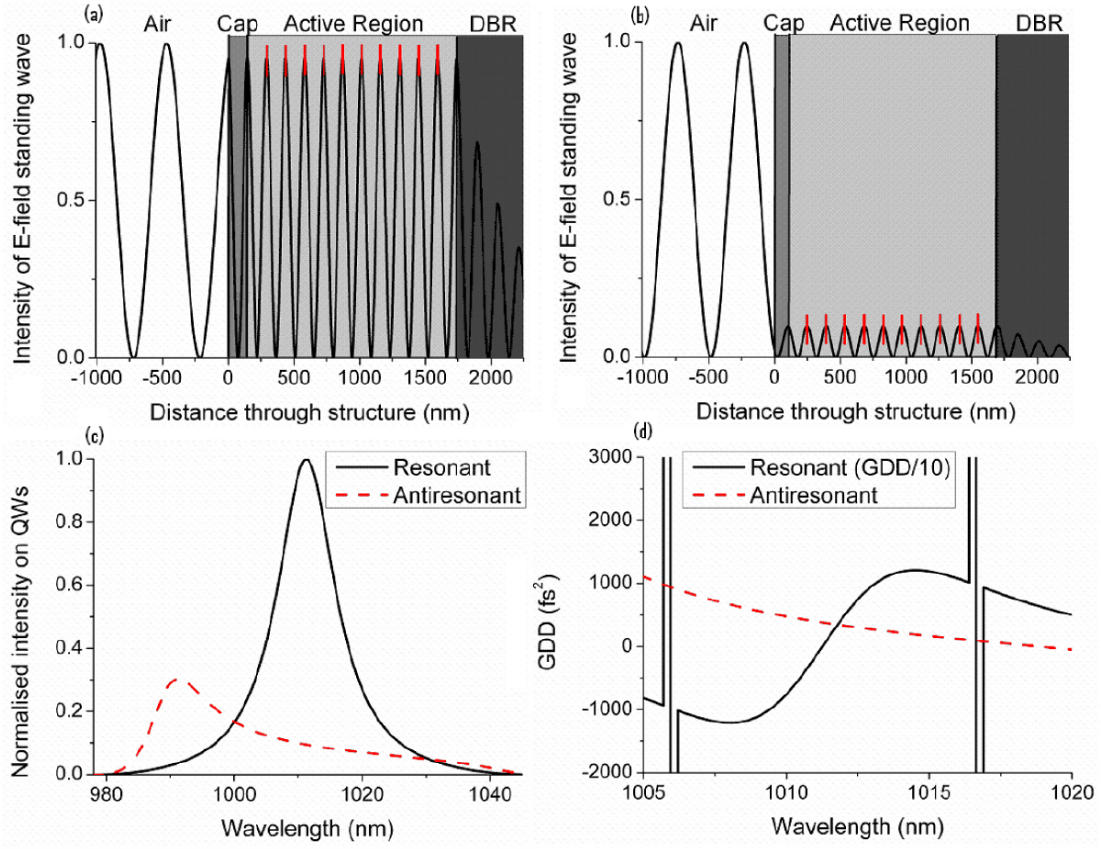

Figure 4.2: Gain structure designs – a) and b) show the refractive index and standing wave intensity as a function of distance through the structure for the resonant and near anti-resonant sample, respectively. c) shows the calculated longitudinal confinement factor as a function of wavelength and d) the calculated dispersion for both structure designs. Figures obtained from (Wilcox et al., 2013)

4.3.2 VECSEL cavity

A Z-shaped cavity is used to study the laser build-up characteristics of the gain samples as shown in figure 4.3. A 100 mm radius of curvature (RoC) high reflector was used to form the short arm of the cavity, whereas the long arm of the cavity consists of a 50 mm RoC high reflector and output coupler used as a folding mirror and cavity end mirror, respectively. The laser cavity length was about 28 cm. The output coupler had a transmission of 0.3 %. The gain structures were pumped with a fibre-coupled 810 nm diode laser focused to a 60 μm radius pump spot. The gain samples were mounted on a temperature-controlled water-cooled copper heat sink.

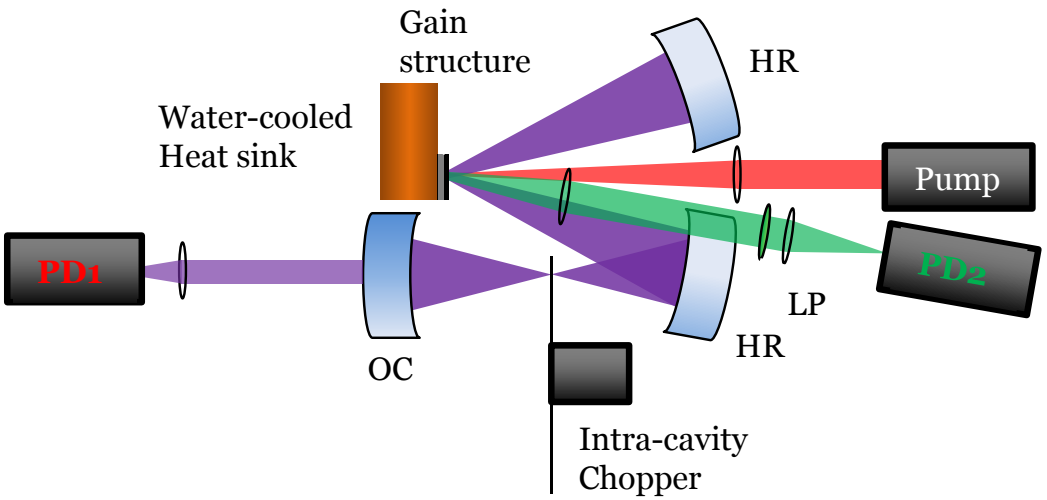

Figure 4.3: Cavity loss experimental set-up – A Z-shaped cavity is used to study the laser build-up characteristics of the gain samples. A 100 mm radius of curvature (RoC) high-reflector (HR) was used to form the short arm of the cavity, whereas the long arm of the cavity consists of a 50 mm RoC HR and output coupler (OC), used as a folding mirror and cavity end mirror, respectively. The laser cavity length was about 28 cm. The output coupler had a transmission of 0.3 % and the gain structures were pumped with a fibre-coupled 810 nm diode laser (pump) focused to a 60 μm radius pump spot. The gain samples were mounted on a temperature-controlled water-cooled copper heat sink. To switch the laser on and off an intra-cavity chopper was used, to unblock and block the cavity mode at the focus in the long arm of the cavity. The output of the laser was recorded by a fast photodiode (PD1) to measure the intra-cavity power build-up. A 11.2-mm focal length lens with a NA of 0.25 was used to collect part of the photoluminescence (PL) emitted from the gain sample. The PL was then recorded by a fast photodiode (PD2) following a long-pass filter (LP) to cut out any scattered pump light.

4.3.3 Experimental Set-up

To switch the laser on and off an intra-cavity chopper was used, to unblock and block the cavity mode at the focus in the long arm of the cavity. This approach was chosen rather than pump modulation to reduce heat load changes in the active region.

Figure 4.3 shows a schematic of the set-up to measure the cavity loss. The output of the laser was recorded by a fast photodiode to measure the intra-cavity power build-up transient and a 11.2-mm focal length lens with a NA of 0.25 was used to collect part of the PL emitted from the gain sample. The lens was at an angle, out of the laser cavity plane, in order not to block the cavity mode. The PL was then recorded by a fast photodiode following a long-pass filter to cut out any scattered pump light.

Figure 4.4 shows the experimental set-up used to determine the spectrally resolved lasing transients. The output of the laser was split by a 90:10 beamsplitter, and the small fraction deflected onto a fast photodiode to measure the intra-cavity power build-up behaviour. As triggering of the chopper was not possible, due to the stochasticity of the laser build-up onset, the intra-cavity power build-up signal was used to trigger the oscilloscope for all subsequent measurements. The remainder of the beam was then directed to a 1-m monochromator where it was split into its wavelengths components. A photodiode following the exit slit was used to measure the spectrally-resolved intra-cavity power build-up. A stepper motor was used to step through the wavelengths measured by the photodiode, thus a power build-up measurement was obtained for each wavelength.

In order to resolve the transient behaviour it was critical that the bandwidths of the electronics were fast enough. The photodiodes used were 1-GHz InGaAs photodetectors (Thorlabs D400FC) coupled with 50 Ω resistors and the oscilloscope had a 200-MHz bandwidth and a risetime of 2.1 ns (Tektronix DPO2024).

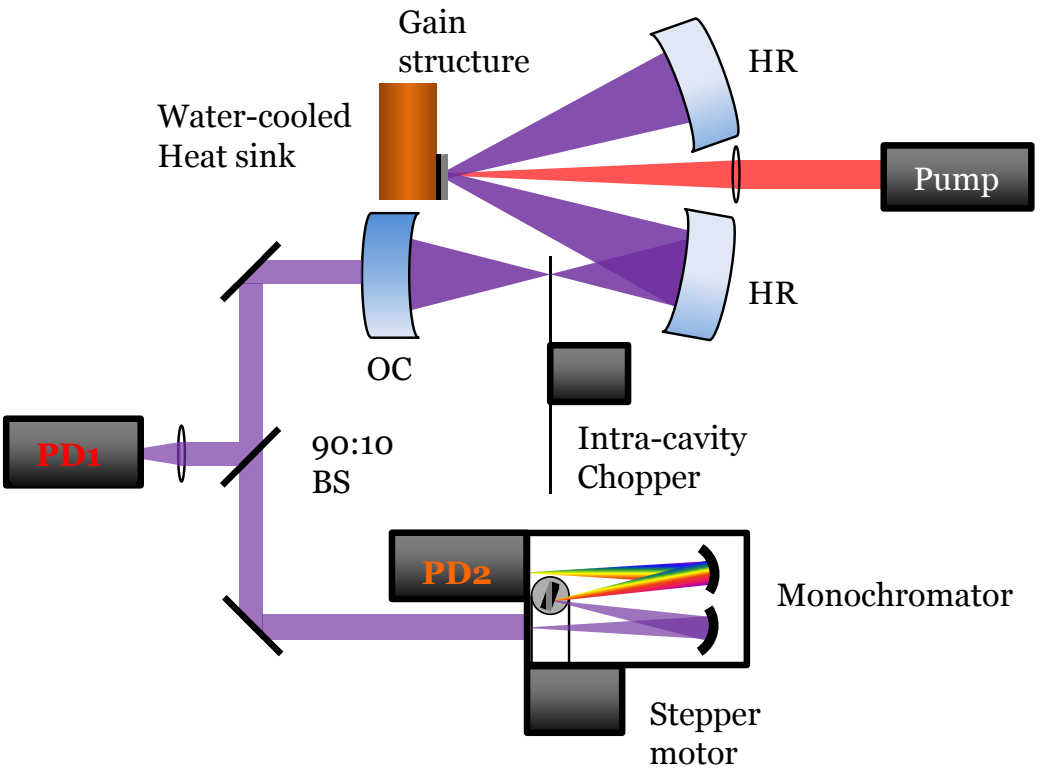

Figure 4.4: Spectrally resolved laser build-up experimental set-up – The output of the laser was split by a 90:10 beamsplitter (BS) where the small fraction was deflected onto a fast photodiode (PD1) to measure the intra-cavity power build-up behaviour. The large fraction of the beam was then directed to a monochromator. A photodiode (PD2), following the exit slit, was used to measure the spectrally-resolved intra-cavity power build-up.

4.4 Results and discussion

4.4.1 Cavity loss extraction

The intra-cavity power build-up transient exhibits a characteristic smooth and fast initial build-up, within a few microseconds, to a steady state, without relaxation oscillations or other features observable (Figure 4.5).

Using the equation 4.13 from section 4.2.2 it was possible to extract the overall cavity loss using the intra-cavity power build-up and PL drop measurements. Figure 4.5 shows an example of a measurement where the photon lifetime in the cavity has been calculated. The PL signal had to be smoothed to avoid digitization effects of the oscilloscope. This together with the cavity round trip time can then be used to obtain the total cavity loss. The extracted cavity lifetime, between 20 and 80 % of the rise, of 0.43 $\pm$ 0.03 μs combined with the cavity roundtrip time of 1.8 ns gives a loss of 0.42 % $\pm$ 0.03 %. This is in line with the losses one would expect as 0.3 % of the loss are due to the output coupler was used and the remaining 0.12 % are most likely due to scattering of the reflector and sample surfaces.

For the resonant sample the temperature of the copper heat sink had to be adjusted so that the quantum well emission was on resonance with the peak of the gain filter. Otherwise the power build-up was convoluted with the shift of the spectrum towards the peak of the gain spectrum and the photon-number build up. This is evident in a slow power-build up component in the intra-cavity power build-up as shown in Figure 4.6 a), where the quantum well emission was off-resonance in respect to the peak of the gain spectrum and an initial shift, of about 8 nm, in the lasing spectrum could be observed, Figure 4.6 b).

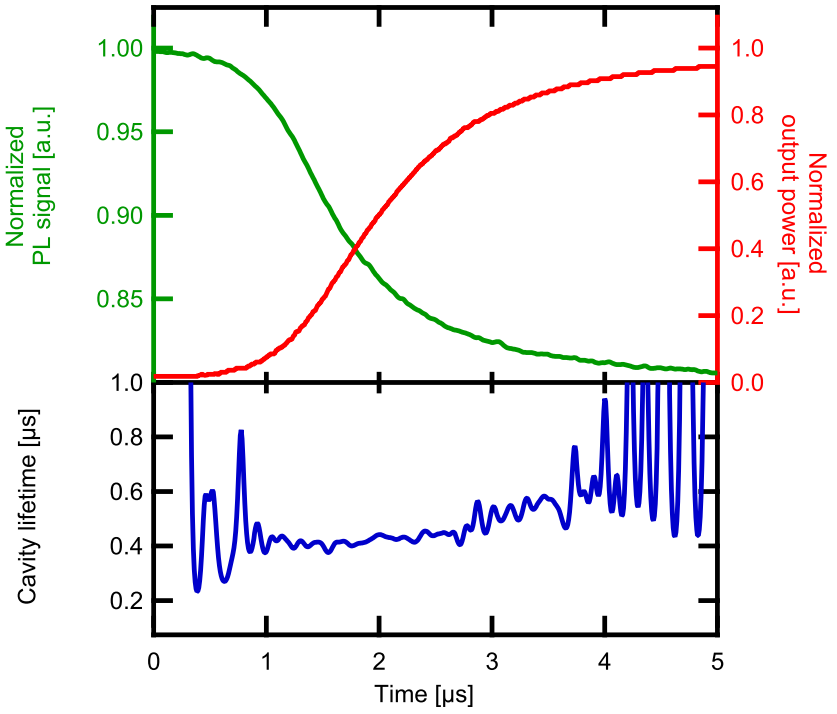

Figure 4.5: Loss extraction via power build-up and PL decay – Calculation of the photon lifetime in the cavity (blue) using the power build-up transient (red) and PL decay (green) measurements for the resonant sample.

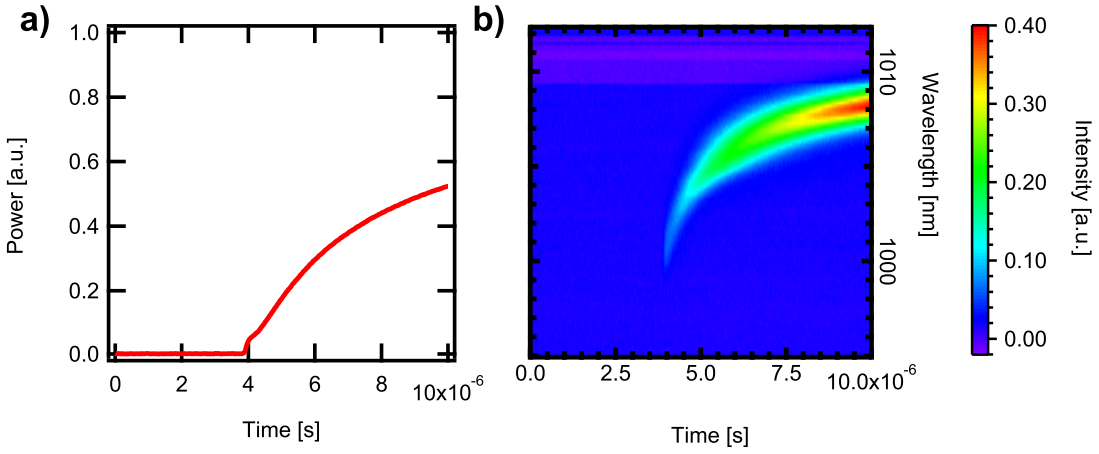

Figure 4.6: Power build-up transient with quantum well emission offset from the peak of the gain spectrum – The power build-up behaviour of the resonant sample shown in a) is convoluted with the shift of the lasing wavelength towards the centre of the gain spectrum observable in b) where a shift of over 8 nm can be seen within the first 5 μs of lasing onset.

4.4.2 Spectrally resolved measurements

The laser spectrum, can continue to change shape over a period of 100 μs or more, during which the photon population is slowly redistributed over the cavity modes, out of the wings and into the centre, in response to the spectral curvature of the gain. This slow dynamic narrowing is referred to as spectral condensation. The individual spectrally resolved power build-up measurements, Figure 4.7, were recorded for up to 100 μs after lasing onset as the spectral dynamics are observable over a much longer time scale. The individual spectrally resolved measurements are combined into a matrix, Figure 4.8, coupling the spectral and transient information. This matrix enables the observation of spectral condensation right from the beginning of the laser build-up and furthermore makes it possible to observe the shift of the lasing wavelength towards the peak of the gain spectrum (Figure 4.6).

For some individual spectrally resolved measurements at wavelengths to which the spectrum collapsed to at the end of the recorded time, a slight ringing effect on the photodiode signal can be observed, Figure 4.9 b). This caused the early voltage photodiode readings at those wavelengths to decrease below the background. This can be seen in Figure 4.6 where at a wavelength of around 1011 nm purple lines (lower value than blue) can be observed. To reduce the photodiode ringing a custom-made chopper blade has been used (Figure 4.9 a)). It had only one slot, long enough to record the signal for $\sim$ 100 μs but giving the photodiode more time to recover.

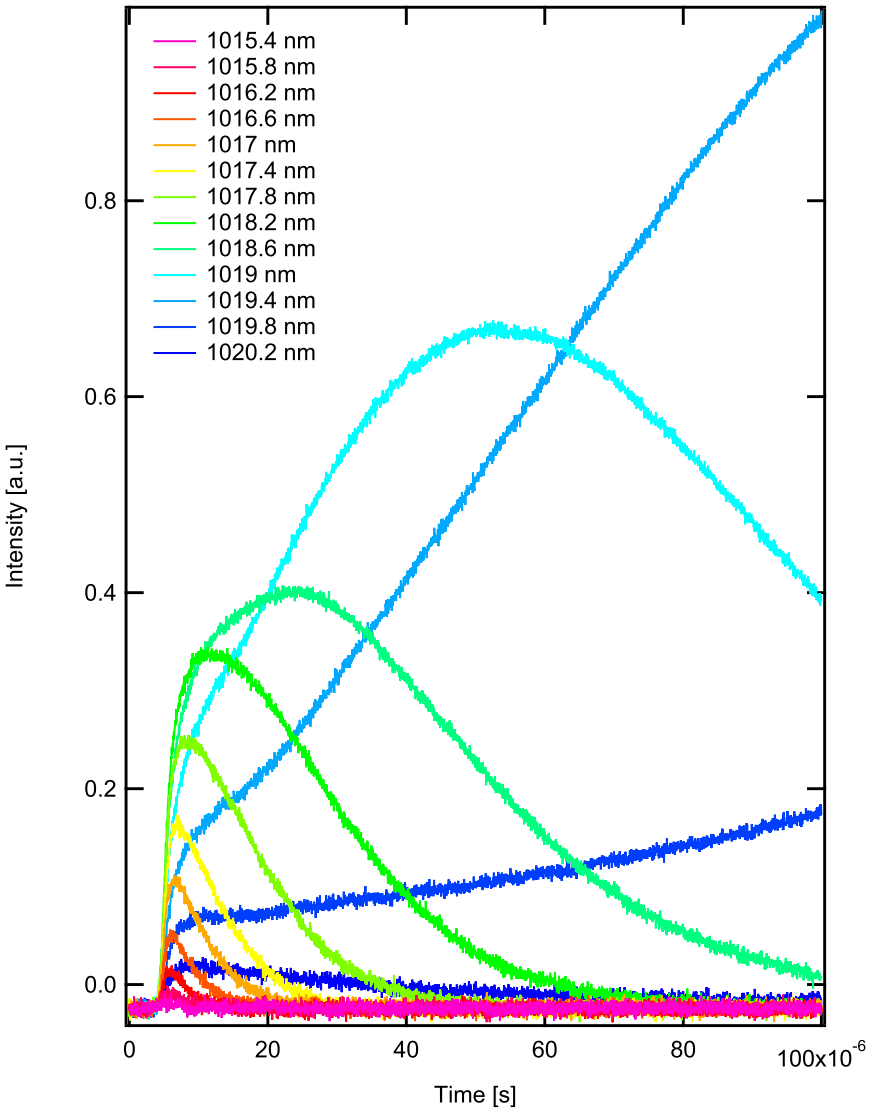

Figure 4.7: Spectrally-resolved laser build-up behaviour of the resonant structure – Individual spectrally resolved laser power build-up measurements between 1015.4 and 1020.2 nm. These can be combined in a matrix to observe the spectral behaviour after lasing onset, shown in figure 4.8.

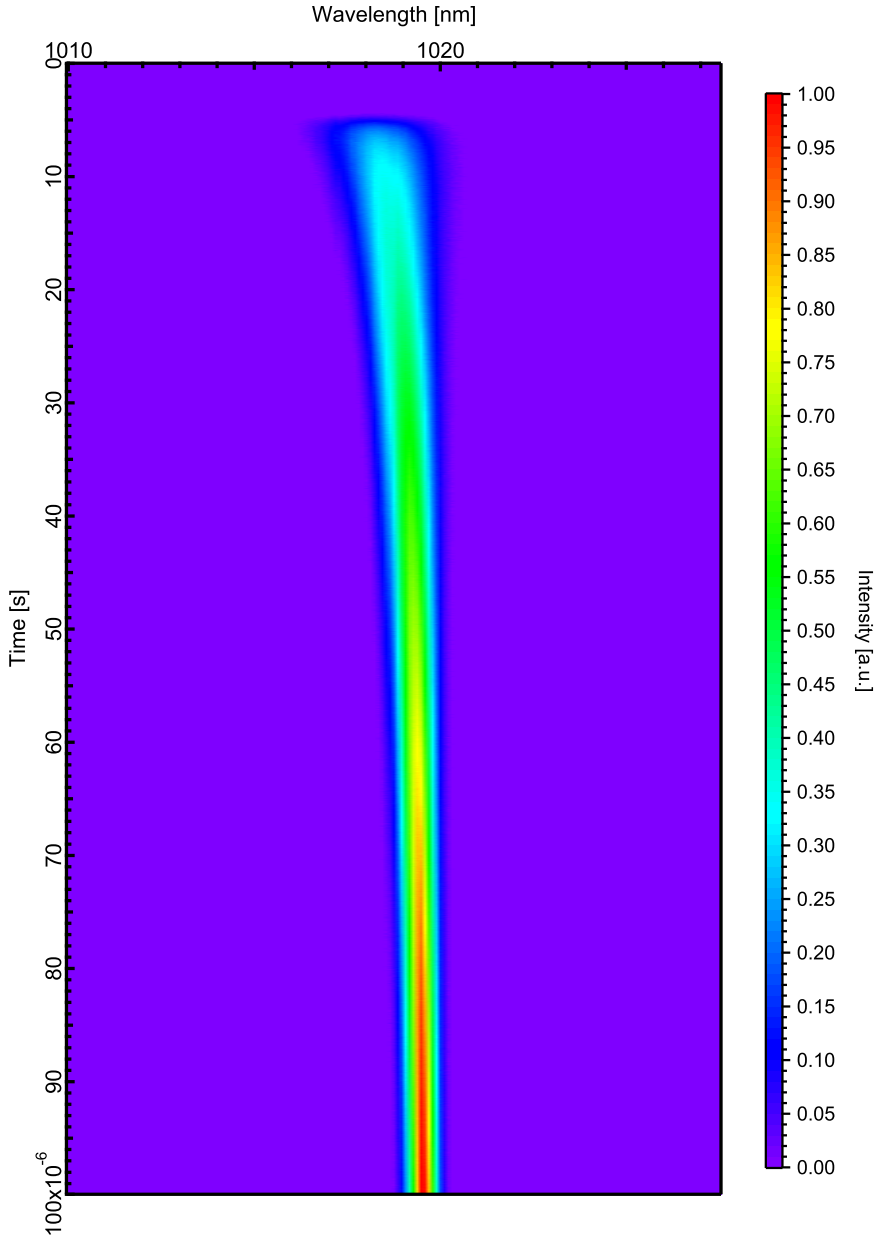

Figure 4.8: Spectral behaviour following lasing onset of the resonant structure– The spectral characteristics of a VECSEL after lasing onset can be observed from within the first microsecond up to ∼100 μs, spectral condensation and a slight shift in lasing wavelength of ∼1 nm can be seen.

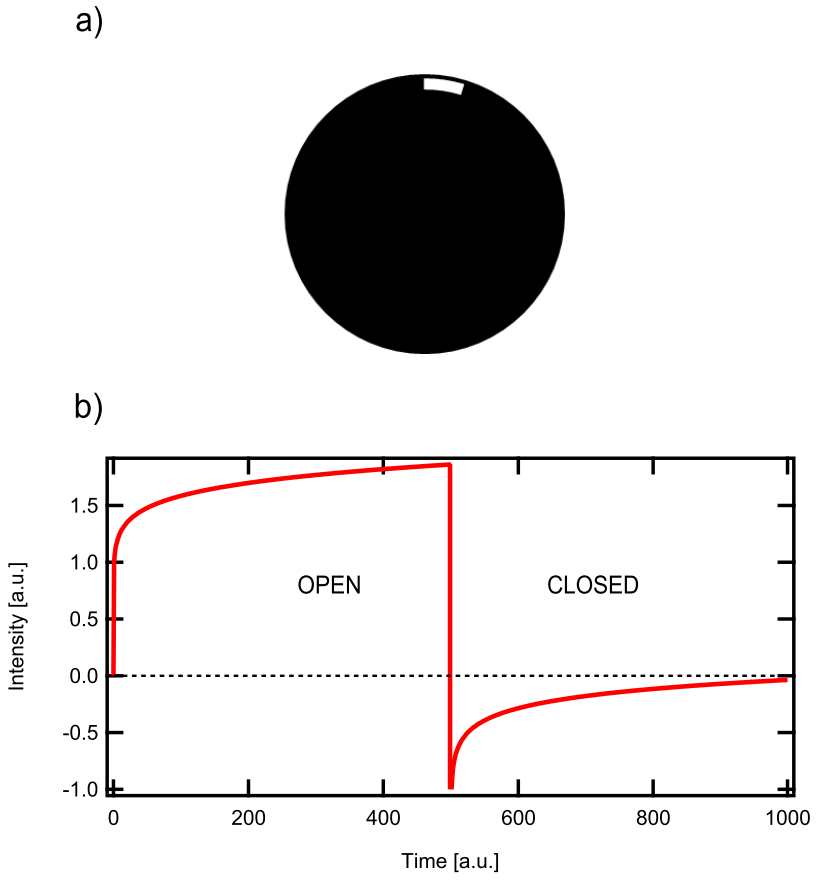

Figure 4.9: Custom chopper blade used to reduce signal ringing – a) shows the single slot blade design used to give the photodiode maximum time to recover and reduce the ringing effect, shown in b). Ringing was only present at wavelengths to which the laser collapsed. The slot length was about 5 mm at $\sim$ 5 cm from the centre of the disc, which, combined with the chopper speed, allowed to record the power build-up for $\sim$100 μs.

4.4.3 Evolution of the gain spectrum

The gain spectrum of the gain chip was obtained by differentiating each line in the matrix, containing the spectral and transient information, with respect to time and dividing it by the intensity at each given time. The individual traces were previously smoothed to reduce differentiation spikes due to noise or digitization.

$$G = \frac{dI/dt}{I} \tag{4.14}$$

A mask was applied to ignore intensity values two orders of magnitude lower compared to the maximum intensity to eliminate dividing by very small numbers. The resulting matrix is shown in figure 4.10.

In order to observe how the gain spectrum evolves over time a parabolic dependence of gain on wavelength was assumed and each row containing at least 4 datapoints in the wavelength dimension was fitted with equation 4.15,

$$G = A(x - x_0)^2 + C, \tag{4.15}$$

where A is the curvature of the parabola, x_0 the centre wavelength and C the offset in the y-direction.

Figure 4.11 shows how each fitting parameter evolves over time. The offset in the y-direction, C, rapidly goes towards zero as the power builds up and the gain saturates, whereas the curvature, A and the centre wavelength, x_0, of the gain spectrum are almost constant over the entire time. Using the fitting parameter it is possible to reconstruct the gain spectrum over the entire measured range of wavelengths, shown in Figure 4.12. The initial rise in the curvature of the gain spectrum is thought to be an artefact due to the mixture of spectral condensation and the signal rising above the noise floor. The errors come from how well the fit-parameters could be determined, which becomes increasingly more difficult when the number of data points decreases. Large errors for some of the fits at later times are due to the spectral condensation, where there are fewer points to fit to.

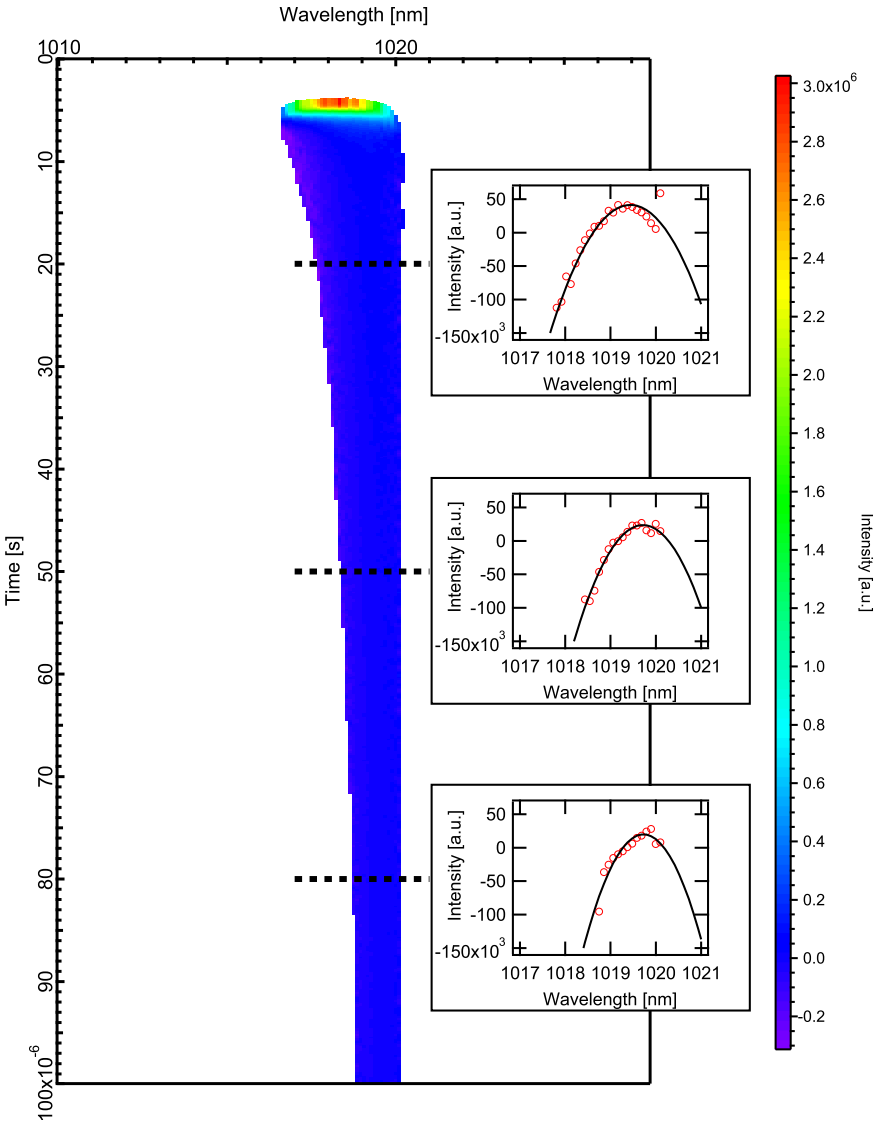

Figure 4.10: Evolution of the gain spectrum of the resonant structure – The gain spectrum obtained using equation 4.14 on figure 4.8, including a mask to ignore data points with an intensity intensity that is lower than two orders of magnitude compared to the maximum. Due to the spectral condensation and the mask fewer data points for the gain spectrum are obtained at later times. The insets show the gain spectra at 20, 50 and 80 μs.

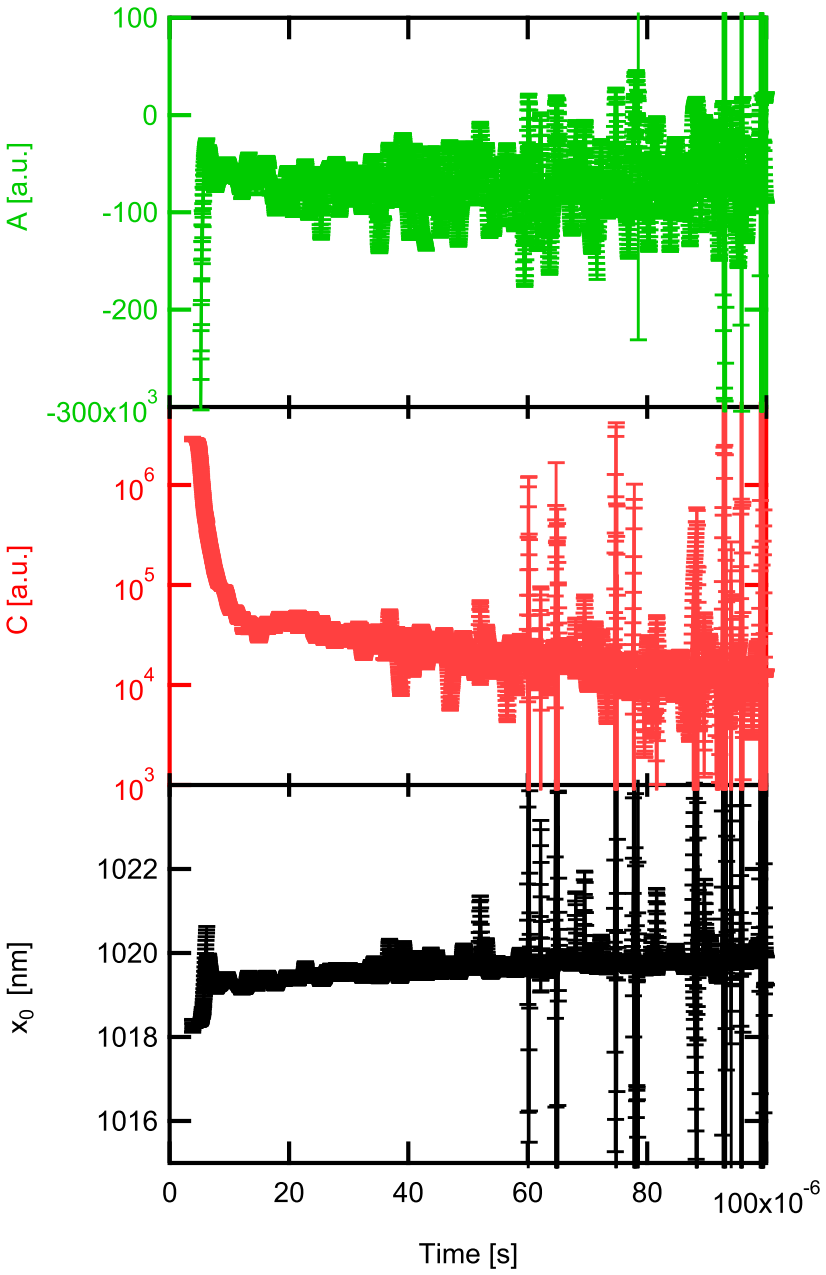

Figure 4.11: Extracted fit parameters for the gain spectrum of the resonant structure – The obtained fit parameters using equation 4.15 on the extracted gain spectra in figure 4.10. The offset in the y-direction (red), C, rapidly goes towards zero as the power builds up and the gain saturates, whereas the curvature (green), A and the centre wavelength (black), x_0, of the gain spectrum are almost constant over the entire time. The first initial rise in the curvature of the gain spectrum is attributed to a convolution of the spectral condensation and the signal rising above the noise floor. The errors for each parameter arise from how well the fit has converged, which becomes increasingly more difficult when the number of data points decreases. At later times, due to the spectral condensation where there are less points to fit to, some larger errors can be observed.

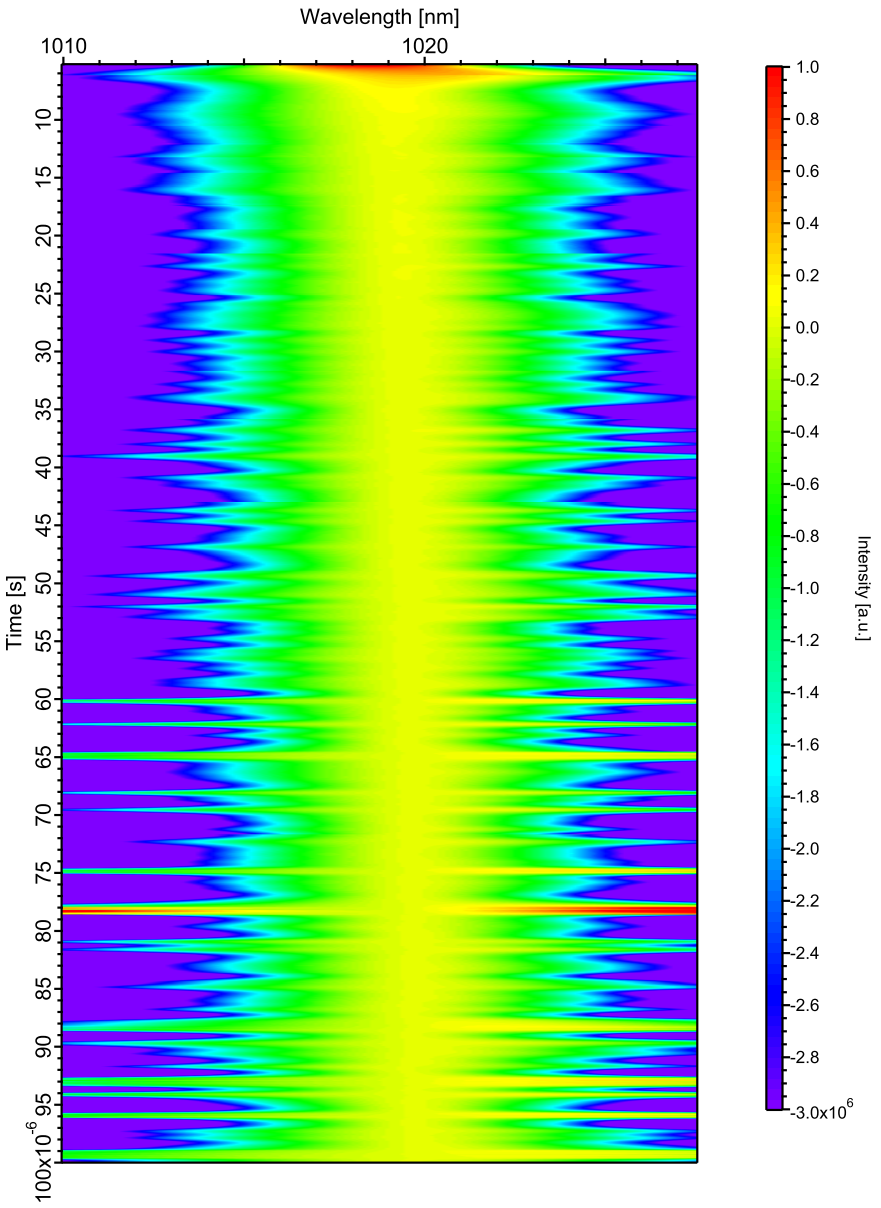

Figure 4.12: Reconstructed gain spectrum of the resonant structure – Using the obtained fitting parameters in figure 4.11 it is possible to reconstruct the gain spectrum over the entire measured range of wavelengths.

4.4.4 Comparision between resonant and near anti-resonant structure

The method described in section 4.4.3 was applied to both the resonant and near anti-resonant sample. The reconstructed gain spectra are shown in figure 4.13, in which parabolic gain spectra, with curvature and centre wavelength extracted from the data of the spectrally resolved onset measurements, are plotted as a function of time. A few artefacts are included, corresponding to spectra which could not be fitted, The vertical axis corresponds to net gain over cavity loss. The analysis shows that the shape of the gain spectrum, its curvature and centre wavelength, remains stable over the period, 80 μs, over which the spectrum evolves.

It can be seen in figure 4.13 that the gain spectrum of the resonant sample is narrower than the gain spectrum of the anti-resonant sample, consistent with the longitudinal confinement factor (LCF) data of figure 4.2. c) The effect does not, however, appear to be large.

By averaging the curvatures found by the fits, excluding the early times, the curvature of the gain filter of a sample per pass through the sample can be obtained, shown in Figure 4.14 for the resonant and anti-resonant sample.

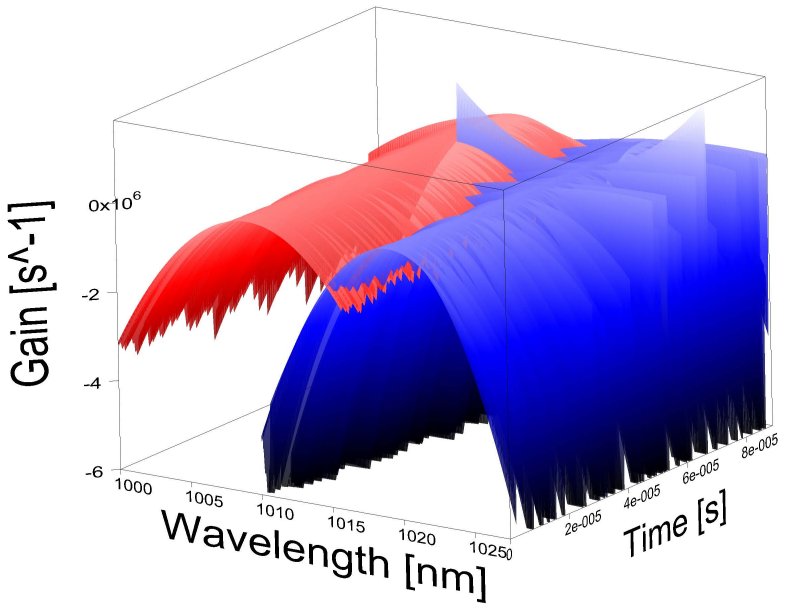

Figure 4.13: Reconstructed gain spectra of the resonant (blue) and near anti-resonant (red) structure – The method described in section 4.4.3 was applied to both the resonant and near anti-resonant sample and their respective reconstructed gain spectra are shown.

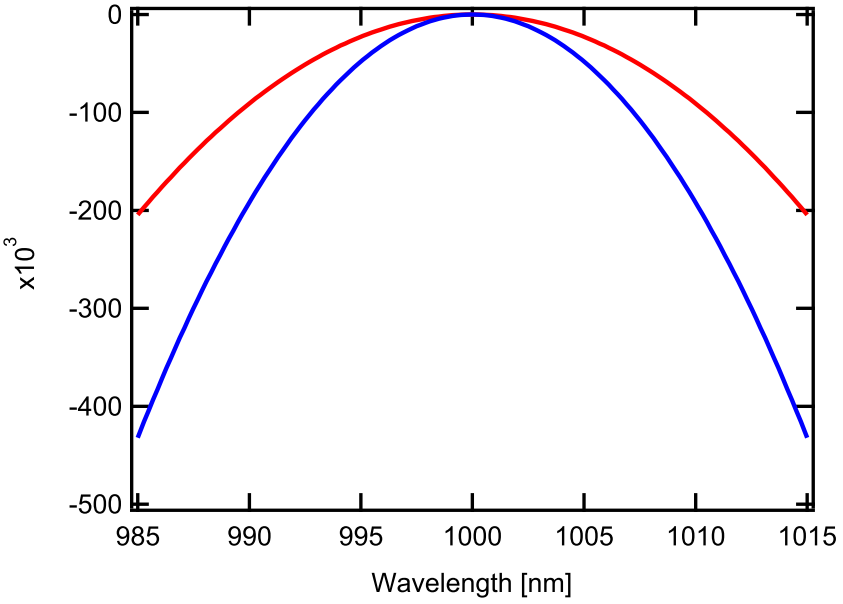

Figure 4.14: Average gain spectra of the resonant (blue) and near anti-resonant (red) structure – Averaging the curvatures found by the fits, excluding the early times, the curvature of the gain filter of a sample can be obtained. Both curvatures of the gain spectra are shown as if they had a common central peak at 1000 nm.

In order to extract an effective gain bandwidth, Ω_g, for both samples we apply the method described in (Barnes et al., 2010) work. These authors show by an analytical model that

$$\Omega_g = \sqrt{\frac{1}{\tau_c \frac{dA}{dt}}}, \tag{4.16}$$

where τ_c is the cavity photon lifetime. $A = \frac{1}{2\mu_2}$,where μ_2 is the spectral variance of the spectrum at generation time. The variation of A with time, derived from data as shown in figure 4.8 for the resonant and anti-resonant structures, is plotted in figure 4.15. At early times the cavity is filling with photons and the approximations made in the analytical model do not apply. At largest times, other mechanisms start to control the laser bandwidth, and spectral condensation ceases. We therefore estimate a bandwidth based on the slope of the approximately linear part at intermediate times using the value $\tau_c = 0.43$ μs, measured as described in section 4.4.1.

The calculated gain bandwidth for the resonant sample is 14 nm and 17 nm for the anti-resonant structure. The surprisingly small difference, given that in figure 4.2 c) it can be seen that the LCF shows a sharp peak for the resonant structure, whereas the LCF for the anti-resonant structure is comparatively flat. It is important, however, to consider the different factors that contribute to the gain bandwidth; the intrinsic gain bandwidth of the quantum wells, which becomes broader with increasing temperature, and the longitudinal confinement factor. In this experiment we were pumping the low temperature-impedance processed ten-quantum well samples with relatively low pump power, ∼1.5 W, thus the temperature of the wells was relatively low.

The inference of the results is that the intrinsic gain bandwidth of the quantum wells was the limiting factor, about 15 nm, and the filter induced by the longitudinal confinement factor decreased (increased) the overall gain bandwidth for the resonant (anti-resonant) structure measurably, ~ 2 nm, but not dramatically. The gain bandwidth of the quantum wells for the resonant sample is likely to be higher compared to the anti-resonant sample, as the resonant sample had to be heated to 52°C in order to be on-resonance, whereas the anti-resonant sample was measured at 20°C, further decreasing the difference between the two gain bandwidths of the structures.

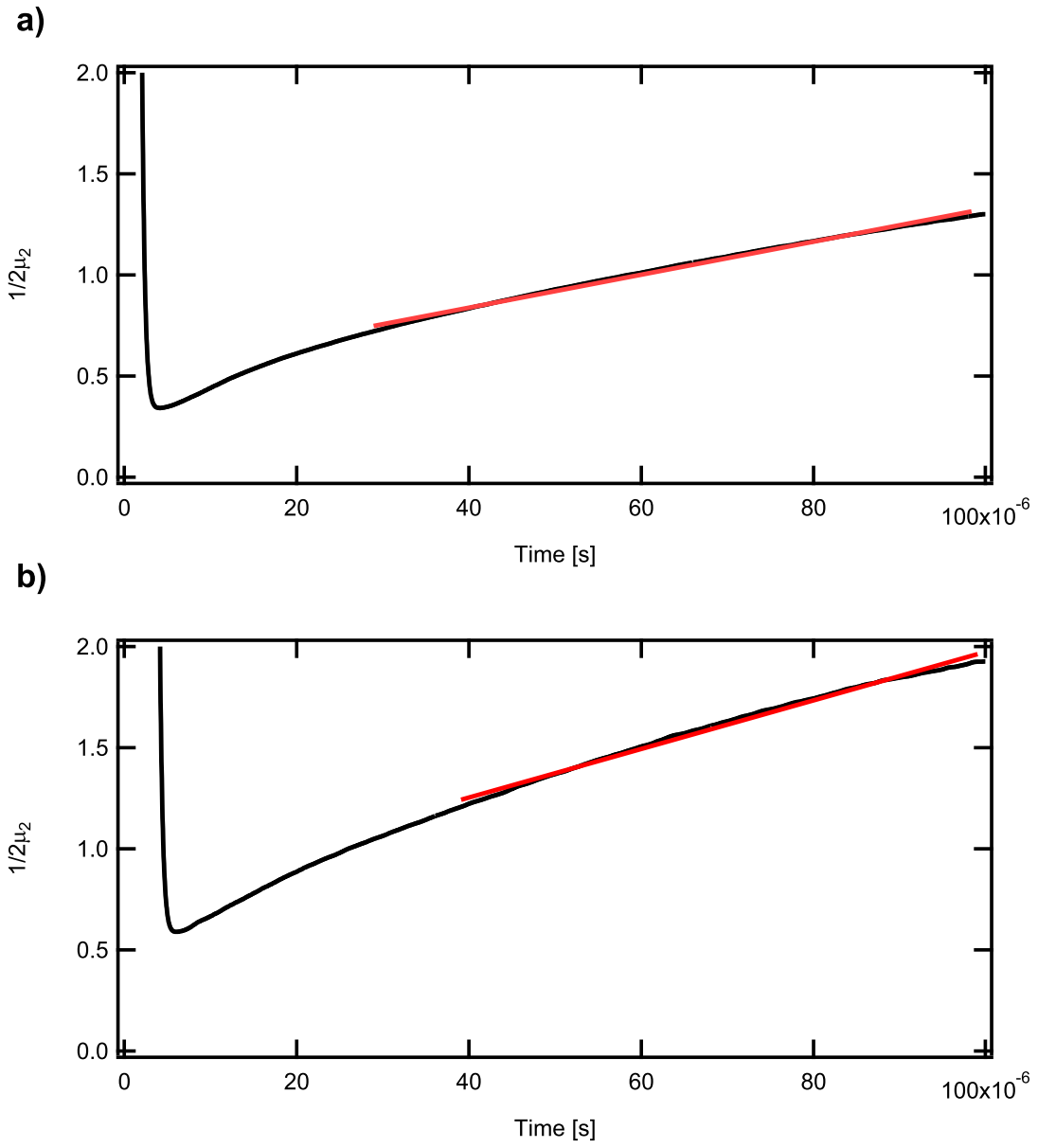

Figure 4.15: Extraction of dA/dt – The plots show the $1/2\mu_2$ for each spectrum measured over the measured period for the a) Antiresonant structure and b) resonant structure. By fitting a straight line to the latter times, where the signal has risen above the noise floor, it is possible to extract dA/dt. The slope for the antiresonant (resonant) structure is 8147.3 ± 11 (12018 ± 22).

4.5 Conclusion

In conclusion I have demonstrated a novel technique to obtain the total cavity loss and observe the spectral condensation of a VECSEL from within the first microsecond of power build-up. The use of the time-resolved PL measurements in combination with the intra-cavity power build-up to extract a cavity loss directly without having to change output couplers or operating conditions was demonstrated.

The spectrally resolved build-up measurements revealed a significant shift of up to 8 nm within the first 5 μs could be observed, which highlighted the need to align the quantum well emission with the spectral filter in order to observe only the power build-up due to the cavity population. Otherwise a convolution between cavity population and wavelength shift towards the peak of the gain is observed.

Furthermore the novel spectro-temporal technique enables the investigation of the gain spectrum of a VECSEL under operating conditions. This does not only allow to obtain a curvature of the gain filter, but also to observe whether it would evolve and change over time, where it was found that the shape of the gain spectrum remained constant. As comparison two different samples, a resonant and anti-resonant design have been investigated, where it was found that the gain spectrum of the resonant sample had a bandwidth of about 14 nm and the anti-resonant structure had a gain bandwidth of about 17 nm. The relatively small difference between the two samples is attributed to the low intrinsic gain bandwidth of the quantum wells, due to the low pump powers used, and the difference in spectral gain bandwidth, due to the different longitudinal confinement factors, was observable but severely reduced.

References

Barnes, M. E., Mihoubi, Z., Wilcox, K. G., Quarterman, A. H., Farrer, I., Ritchie, D. A., Garnache, A., Hoogland, A., Apostolopoulos, V., and Tropper, A. C. (2010). Gain bandwidth characterization of surface-emitting quantum well laser gain structures for femtosecond operation. *Optics Express*, 18(20):21330–21341.

Bernstein, L. (1966). Semiconductor Joining by the Solid Liquid Interdiffusion (SLID) Process. *Journal of The Electrochemical Society*, 113(12):1282–1288.

Borgentun, C., Bengtsson, J., and Larsson, A. (2011). Direct measurement of the spectral reflectance of OP-SDL gain elements under optical pumping. *Optics Express*, 19(18):16890–16897.

Chow, W. W. and Koch, S. W. (1999). *Semiconductor-Laser Fundamentals*. Springer.

Coldren, L. A. and Corzine, S. W. (1995). *Diode Lasers and Photonic Integrated Circuits*. Wiley.

Diehl, W., Brick, P., Chatterjee, S., Horst, S., Hantke, K., Rühle, W. W., Stolz, W., Thränhardt, A., and Koch, S. W. (2007). Dynamic behavior of 1040 nm semiconductor disk lasers on a nanosecond time scale. *Applied Physics Letters*, 90:241102.

El Amili, A. E., Gredat, G., Alouini, M., Sagnes, I., and Bretenaker, F. (2012). Experimental study of the delayed threshold phenomenon in a semiconductor laser. *the European Physical Journal Applied Physics*, 58(1):201210501.

Findlay, A. and Clay, R. A. (1966). The measurement of internal losses in 4-level lasers. *Physics Letters*, 20(3):277–278.

Hader, J., Hardesty, G., Wang, T., Yarborough, M. J., Kaneda, Y., Moloney, J. V., Kunert, B., Stolz, W., and Koch, S. W. (2010). Predictive Microscopic Modeling of VECSELs. *Journal of Quantum Electronics*, 46(5):810–817.

Hader, J., Wang, T., Yarborough, J. M., Dinee, C. A., Kaneda, Y., Moloney, J. V., Kunert, B., Stolz, W., and Koch, S. W. (2011). VECSEL Optimization Using Microscopic Many-Body Physics. *Selected Topics in Quantum Electronics*, 17(6):1753–1762.

Haug, H. and Koch, S. W. (2004). *Quantum Theory of the Optical and Electronic Properties of Semiconductors*. World Scientific Publishing, Singapore.

Kuznetsov, M., Hakimi, F., Sprague, R., and Mooradian, A. (1999). Design and characteristics of high-power (>0.5-W CW) diode-pumped vertical-external-cavity surface-emitting semiconductor lasers with circular TEM_{00} beams. *Selected Topics in Quantum Electronics*, 5(3):561–573.

Mangold, M., Wittwer, V. J., Sieber, O. D., Hoffmann, M., Krestnikov, I. L., Livshits, D. A., Golling, M., Südmeyer, T., and Keller, U. (2012). VECSEL gain characterization. *Optics Express*, 20(4):4136–4148.

Moloney, J. V., Hader, J., and Koch, S. W. (2007). Quantum design of semiconductor active materials: laser and amplifier applications. *Laser & Photonics Reviews*, 1(1):24–43.

Wilcox, K. G., Tropper, A. C., Beere, H. E., Ritchie, D. A., Kunert, B., Heinen, B., and Stolz, W. (2013). 4.35 kW peak power femtosecond pulse mode-locked VECSEL for supercontinuum generation. *Optics Express*, 21(2):1599–1605.

Chapter 5

Supercontinuum generation with amplified mode-locked VECSELs

5.1 Introduction

This chapter describes my work on supercontinuum generation with an amplified mode-locked VECSEL which has been published in Photonics Technology Letters (Head et al., 2013).

The generation of supercontinuum, or severe spectral broadening, in photonic crystal fibre (PCF) has found applications in a wide range of research areas such as telecommunications, metrology and spectroscopy. Typical laser sources used to generate supercontinuum are pulsed solid-state or fibre lasers that operate at repetition rates up to approximately 100 MHz. While these low-repetition-rate sources easily produce spectrally broad supercontinuum due to their high peak power, higher repetition rates are desirable for frequency combs. The resulting increased mode spacing in the frequency comb leads to more energy per frequency mode. Furthermore it is possible to isolate individual modes using a simple diffraction grating (Fortier et al., 2006; Bartels et al., 2009), thus VECSELs, which naturally work in the GHz repetition rate regime, are a potentially interesting laser source for frequency combs.

The supercontinuum generated for frequency combs should, however, be coherent. Coherence in this case means that every pulse generating supercontinuum produces the same phase structure for the spectral components. The shot-to-shot phase coherence is required to obtain the carrier-envelope offset frequency via a f-2f beat note technique to self-reference the frequency comb (Telle et al., 1999), which typically requires sub-100 fs pulse durations when using photonic crystal fibre (PCF) pumped close to its zero dispersion wavelength (ZDW)(Dudley et al., 2006). This limit can be stretched, with 170-fs pulses at a wavelength of 1.5 micron, as Stumpf et al. (2010) have demonstrated using state-of-the-art dispersion-flattened, polarization-maintaining, highly non-linear fibre. Alternatively supercontinuum with a high degree of coherence can be generated using all-normal dispersion PCF with pulse durations of several hundred femtoseconds (Heidt, 2010; Chow et al., 2006), although the supercontinuum generated in this manner has typically a narrower spectral width compared to supercontinuum generated with a PCF pumped closely to its ZDW.

VECSELs are potentially flexible sources for coherent GHz supercontinuum generation. Due to the *class-A* laser characteristics and the passive mode-locking mechanism they are low-noise sources (Paschotta, 2004; Wilcox et al., 2006; Quarterman et al., 2008; Wittwer et al., 2011, 2013) and could thus improve the stability of frequency combs. However although there has been tremendous progress in power scaling of VECSELs recently (see Chapter 3), the direct generation of both sub-100 fs pulses and high average output power in VECSELs has not been achieved yet.

Sub-picosecond pulsed fibre amplifier systems have reached output powers of 830 W at a 78 MHz repetition rate with a 640 fs pulse duration using a chirped pulse amplification architecture (Eidam et al., 2010). More recently a fibre master oscillator power amplifier (MOPA) system has achieved 110 W at a 1.3 GHz repetition rate with a 890 fs pulse duration requiring only modest pulse stretching (Zhao et al., 2012). As the repetition rate increases, the pulse energy decreases and the linear amplification regime can be used to correspondingly higher average powers before pulse stretching becomes necessary.

Inbetween the linear and non-linear amplification regimes lies a regime of parabolic amplification. In this amplification regime the non-linear interaction spectrally broadens

the pulse and due to the dispersion it is temporally elongated, in a self-similar manner. Depending on the pulse energy launched into the fibre the parabolic regime is reached after different propagation distances. Following a sufficiently long propagation distance in the amplifier fibre and in the parabolic regime the pulses acquire a nearly linear chirp which enables efficient compression of the amplified pulses. Furthermore due to the additional wavelength components created it is possible to compress the pulses to durations shorter than the duration of the seed pulse (Fermann et al., 2000).

Fibre MOPA systems provide a complementary technology to ML-VECSELs to enable high power GHz amplification and supercontinuum generation, especially via the parabolic amplification regime to obtain sub-100-fs pulse durations. In previous work Dupriez et al. (2006) reported a 500-femtosecond VECSEL seeded MOPA system where average powers of 53 W were reached and it was possible to compress the amplified pulses to a 110-fs duration. However only a few hundred milliwatts of the output power could be compressed due to the limited power handling of the aluminum reflection grating compressor used.

Chamorovskiy et al. (2012) have generated a supercontinuum with a VECSEL MOPA system where a 500 m long GeO_2-codoped silica fibre, driven by a 1.57 μm VECSEL MOPA producing 15.5 ps pulses, was used.

In this chapter I describe my work using a VECSEL MOPA system producing 40 W of average power from which a 70 %-throughput grating compressor was used to produce 400 fs pulses. These pulses were then used to generate supercontinuum in two samples of PCF; an all-normal dispersion PCF, and a PCF with a zero dispersion wavelength of 1040 nm.

5.2 Experimental methods

The amplified pulse source, shown in Figure 5.1, consists of three distinct sections; the VECSEL, the cascaded fibre amplifier system and the compressor. The compressed output was then launched into the PCF to generate supercontinuum. I describe the VECSEL in section 5.2.1 followed by the fibre amplifier and pulse compression system in section 5.2.2.

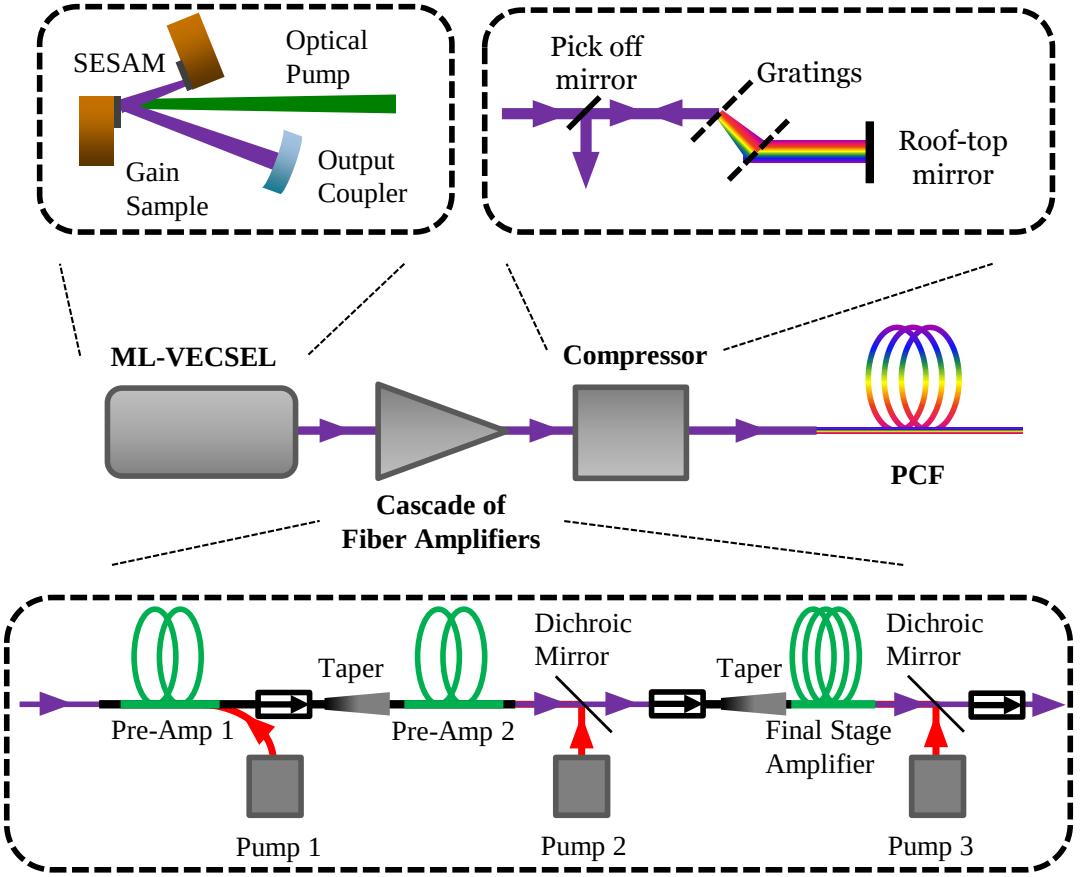

Figure 5.1: Schematic of the experimental set-up – The VECSEL was used as a seed laser for a three-stage ytterbium-doped fibre amplifier system. The amplified pulses, elongated due to dispersion in the fibres, were recompressed with a high throughput grating compressor and free-space launched into the PCF to generate supercontinuum.

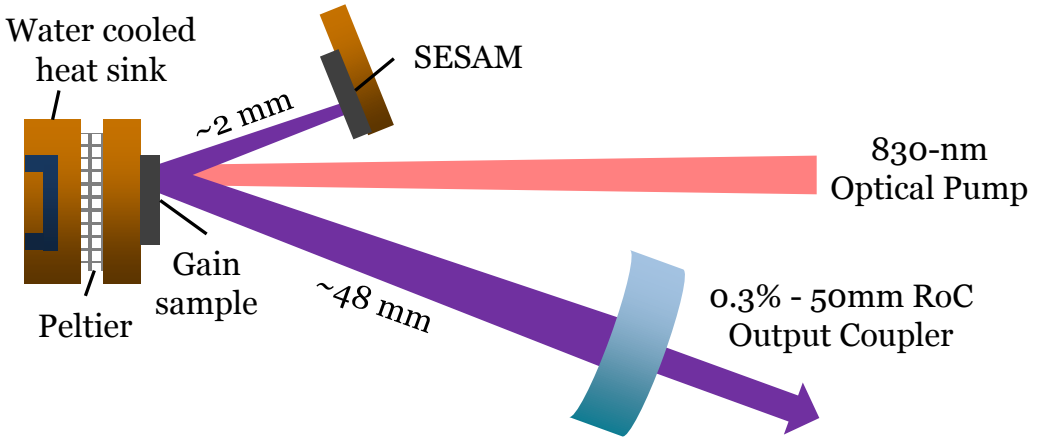

Figure 5.2: VECSEL cavity – A V-shaped cavity is formed by a 0.3 % output coupler with a radius of curvature of 50 mm, the gain structure, which acts as a plane folding mirror, and the SESAM, the cavity end mirror. The distance between the output-coupler and the gain sample is ∼48 mm and ∼2 mm between the gain sample and the SESAM. The gain sample is optically pumped by a 830-nm fiberized diode laser. The SESAM is used to passively mode-lock the VECSEL.

5.2.1 VECSEL

5.2.1.1 Cavity

The ML-VECSEL in this experiment consists of the gain structure, a Semiconductor Saturable Absorber Mirror (SESAM) and a spherical output coupler. A V-shaped cavity is formed by a 0.3 % output coupler with a radius of curvature of 50 mm, the gain structure which acts as a plane folding mirror, and the SESAM as the cavity end mirror, as shown in figure 5.2. The gain sample is optically pumped by a 830-nm fiberized diode laser. The cavity is designed to give a fundamental laser mode with a 60 μm radius waist on the gain, matching the pump spot, and a 20 μm radius waist on the SESAM, ensuring that the SESAM is saturated more strongly than the gain, to achieve mode-locking.

The gain structure is mounted on a water-cooled temperature-controlled copper block. Neither the gain nor the SESAM structure has been processed, limiting the maximum average output power (Okhotnikov, 2010). All components are directly mounted on a

single Invar plate to reduce misalignment due to vibrations or thermal drift and thus improve long-term mode-locked stability.

5.2.1.2 Output characteristics

The target wavelength for the VECSEL seed was 1040 nm in order to achieve optimal amplification in the ytterbium fibre amplifier system. For this particular combination of gain and SESAM wafers, a heat sink temperature of 15 °C and pump power of 1280 mW produced a laser spectrum centered at 1040 nm with a Full Width Half Maximum (FWHM) of 2.85 nm, corresponding to a train of near transform-limited 400 fs pulses at a repetition rate of 3 GHz and an average output power of 20 mW. Figure 5.3 shows the optical spectrum and intensity autocorrelation of the VECSEL output.

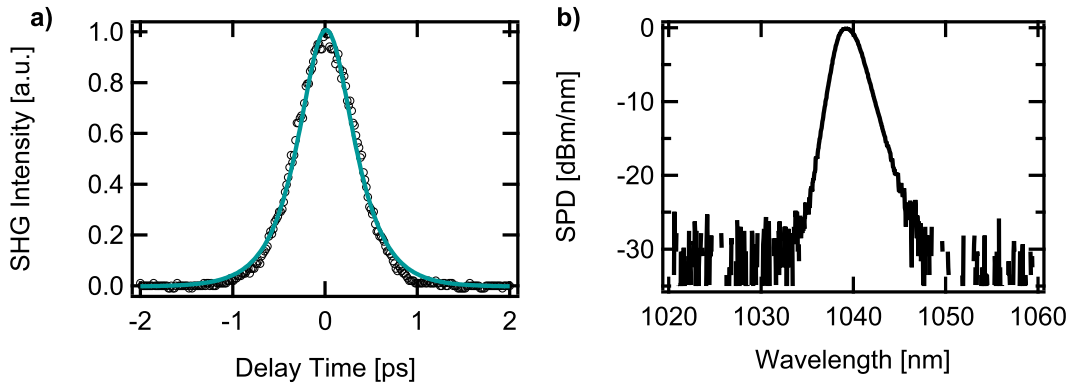

Figure 5.3: ML-VECSEL characteristics – a) Second harmonic generation (SHG) intensity autocorrelation of the pulse (black) with a sech^2 fit (blue). b) Normalized spectral power density (SPD) of the spectrum of the ML-VECSEL. The pulse duration of the VECSEL is 400 fs and the centre wavelength is at 1040 nm with a full width at half maximum of 2.85 nm.

5.2.1.3 Mode-locking stability

This particular VECSEL, gain sample and SESAM combination, produced a pulse train lasting several minutes. Any significant intermittency in seeding the amplifiers can cause severe amplification of spontaneous emission and ultimately destroy the amplifier fibres. It is important to note that a intermittency in seeding the amplifiers may be due not only to a drop in average power, but also due to a shift in wavelengths of the seeding laser to a wavelength outside of the gain spectrum. It was therefore important

to check what the characteristics of our VECSEL were when it lost its mode-locking. To investigate this we recorded the output spectrum of the VECSEL every second over several minutes fur multiple "takes". The spectrum of the VECSEL would typically narrow slowly over time and at some point jump into continuous wave operation, shown in figure 5.4. By investigating different combinations of samples and operating conditions (heat sink temperature and pump power) a combination was found that did not exhibit a significant jump in wavelength when mode-locking was lost. Figure 5.5 shows the shift of the centre wavelength (a) and the spectral bandwidth (b) for ten test runs.

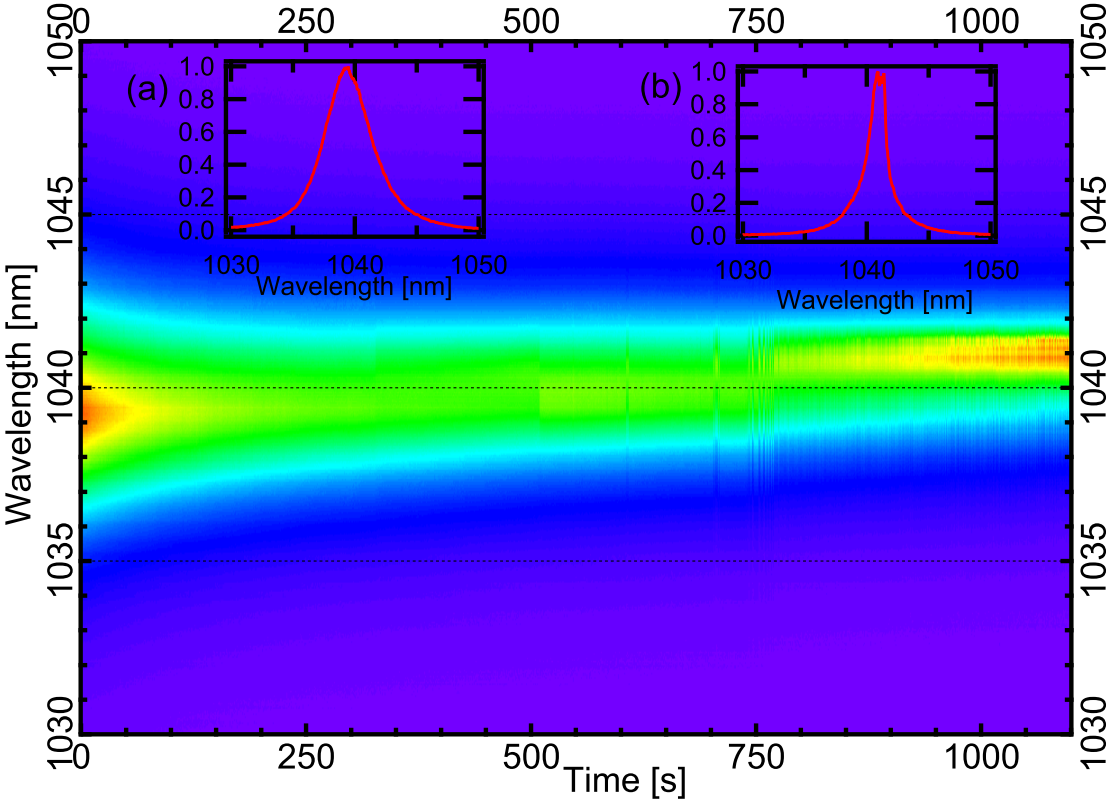

Figure 5.4: Spectral stability of a ML-VECSEL – Spectral behaviour over time of a mode-locked VECSEL where inset a) shows a mode-locked spectrum at 20 s and b) a continuous wave spectrum at 1050 s. The spectral bandwidth decreases over time until, at an unpredictable time, the laser switches from being mode-locked to continuous wave (CW) operation (here after about 750 s). There is however no significant wavelength jump when the laser goes into CW operation, ensuring a stable saturation of the pre-amplifiers of a ytterbium fibre amplifier system.

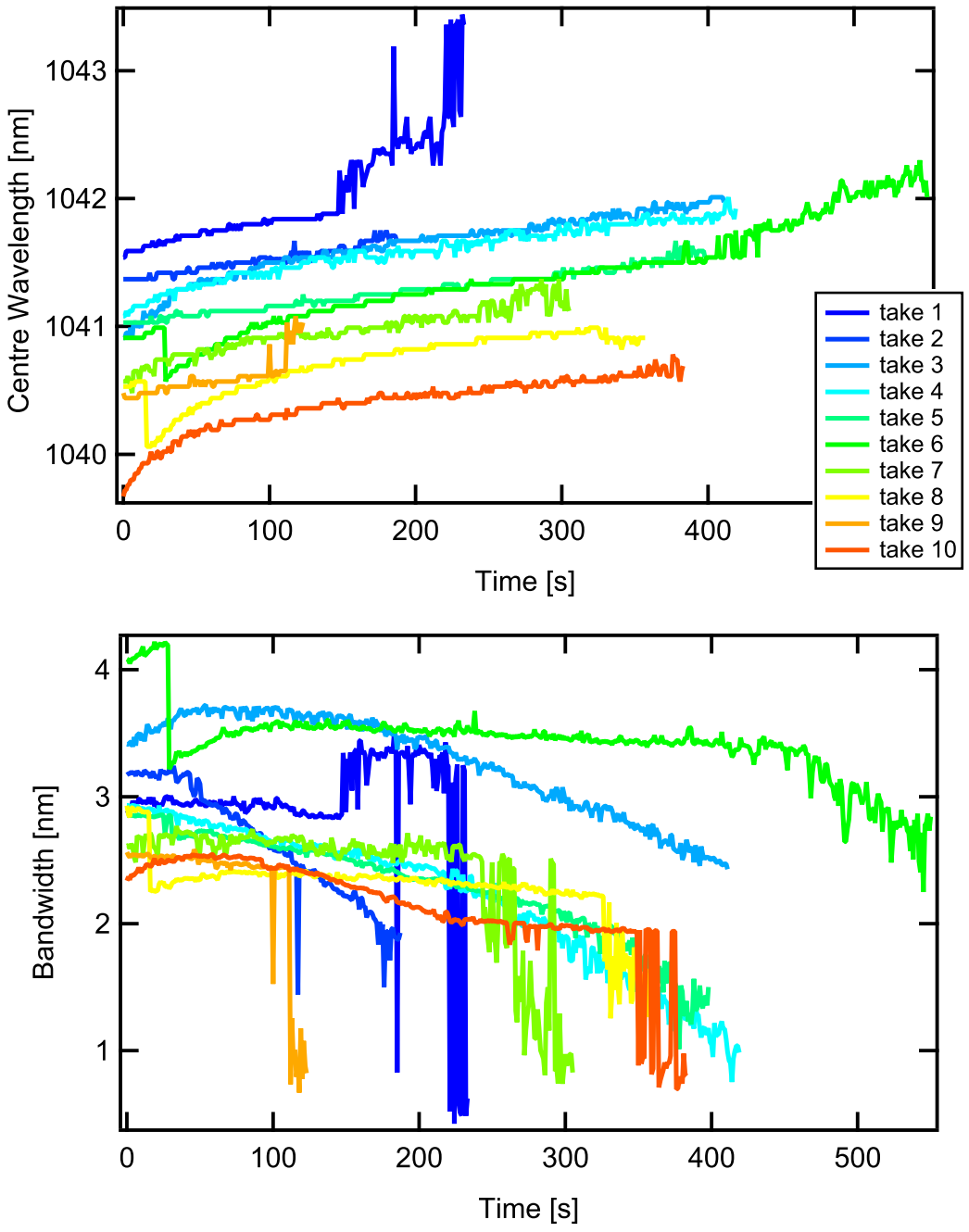

Figure 5.5: Mode-locking stability over ten test runs – a) The centre wavelength and b) the spectral bandwidth of the recorded spectra for ten test runs. For all test runs the spectra shift towards longer wavelengths over time at similar rates, whereas the bandwidth decreases, at different and unpredictable rates, until mode-locking is lost. The most significant shift of the centre wavelength observed, 1.5 nm, occurred during *take 1*, which is still within the acceptable limits for seeding a ytterbium doped fibre amplifier.

5.2.2 Amplifier system

The MOPA system used in this experiment is similar to the set-up used by Chen et al. (2010b,a) but with a VECSEL as master oscillator. The system is based on polarization-maintaining large mode area (LMA) fibre technology, ensuring a robust and stable amplifier system. The first and second pre-amplifiers are ytterbium-doped fibres with core diameters of 5 μm and 25 μm and lengths of 2 m and 2.7 m respectively. Both pre-amplification stages are reverse pumped using 975 nm fiberized diodes. The small core fibre in the first amplifier was chosen in order to maintain a good signal-to-noise ratio and to provide high gain with the low-power wavelength division multiplexed coupled pump-diode. The second preamplifier had a larger core to reduce non-linear effects and had sufficient output power to saturate the final amplifier. We used fibre lengths long enough to absorb the pump power efficiently, but short enough to avoid gain narrowing (He et al., 2006).

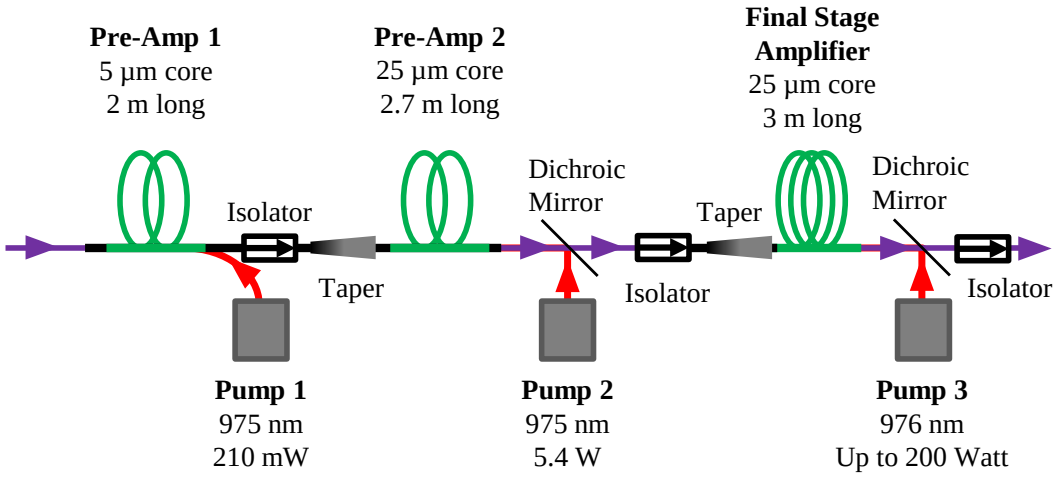

Figure 5.6: Cascaded amplifier chain – The first and second pre-amplifiers are ytterbium-doped fibres with core diameters of 5 μm and 25 μm and lengths of 2 m and 2.7 m respectively. Both pre-amplification stages are reverse pumped using 975 nm fiberized diodes. Following each amplification stage the signal is passed through an isolator. After pre-amplification the signal is free-space-coupled into the final-stage amplifier. The final-stage amplifier fibre, equivalent to that used in the second pre-amplifier, is a 3 m length of double-clad LMA ytterbium-doped fibre, which is reverse pumped with a high power fiberized diode laser source (Laserline LDM 200-200) at 976 nm. To achieve single mode operation from these few-mode LMA fibres the inputs to the second pre-amp and final-stage amplifier are pre-tapered.

Following each pre-amplification stage the signal is passed through an isolator. After pre-amplification the signal is free-space-coupled into the final-stage amplifier. The final-stage amplifier fibre, equivalent to that used in the second pre-amplifier, is a 3 m length of double-clad LMA ytterbium-doped fibre with a 340-μm diameter D-shaped inner-cladding, which is reverse pumped with a high power fiberized diode laser source at 976 nm (Laserline LDM 200-200). The pump launch efficiency for the final two amplifiers was estimated to be $\sim$ 70 %. The second and final amplifier stage 25-μm-core diameter fiber had a V-number of 4, meaning that in theory it could support $\sim$ 7 modes. To ensure single mode operation ($M^2 < 1.1$) the fiber was tapered down to a 9.2μm diameter and a corresponding V-number of 1.5 to act as a mode filter, as described by Chen et al. (2010b). Following the final stage amplifier, the amplified signal passes through an isolator and a high throughput compressor (Ibsen FSTG-PCG-1250-1064 gratings). The amplified and compressed VECSEL signal is then passed through a telescope to reduce the beamsize and is free-space coupled into the photonic crystal fibre.

5.2.3 Photonic crystal fibres

Optical fibres are typically made of two concentric glass cylinders that have a difference in refractive index, where the inner core has a higher index. Photonic crystal fibres (PCFs), for supercontinuum generation, use an air-hole region around a solid glass core where the air-hole region has a lower refractive index. By engineering the core and hole size and the distance between the holes it is possible to design the effective refractive index of the air-hole region to give the desired waveguide properties (Knight et al., 1996; Dudley et al., 2006). The resulting few micron core diameter leads to a high confinement of the electric field increasing the non-linear effects (Broderick et al., 1999). Due to the small core size, launching into the cores of the PCFs can be tricky, with typical launching efficiencies of $\sim$ 50 %. This tremendous loss can have detrimental effects on the launch itself as the lost power heats the fibre end causing movement of it, decreasing the launch efficiency further and thus increasing the power loss even further. To improve thermal

handling, and thus allow for a higher average power to be launched, the end-caps of the PCF were collapsed and polished.

The two different PCFs used in this experiment are a 10 m long all-normal dispersion PCF (NL-1050-NEG-1, NKT Photonics) with a dispersion minimum at 1050 nm; and a 1 m long PCF (SC-5.0-1040, NKT Photonics) with a zero dispersion wavelength (ZDW) of 1040 nm, closely matched to the wavelength of the amplified signal.

The spectral broadening processes in PCFs pumped closely to their ZDW, in the anomalous dispersion regime, are dominated by soliton dynamics, such as soliton fission and dispersive wave generation (Dudley et al., 2006). Due to the noise of the seed pulse and the stochastic nature of those processes, pulse durations below 100 fs are typically required, where self-phase-modulation (SPM) start to dominate the spectral broadening process, to generate coherent supercontinuum with a PCF pumped in the anomalous dispersion regime (Dudley et al., 2006). In all-normal dispersion PCF the soliton-related effects are suppressed and spectral broadening is predominantly due to SPM. This typically produces a supercontinuum with a high degree of coherence with symmetrical spectral broadening, while maintaining a smooth single pulse (Agrawal, 2001; Heidt, 2010).

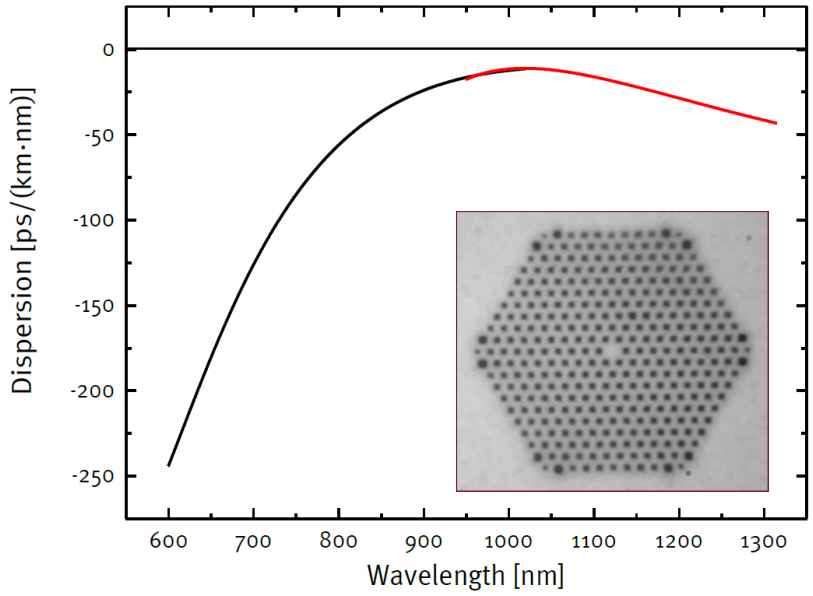

Figure 5.7: All normal dispersion photonic crystal fibre – Dispersion relation of the photonic crystal fibre with an all normal dispersion. The inset shows the structure of the all-normal dispersion photonic crystal fibre. Figures obtained from the specification sheet of the NL-1050-NEG-1 fibre from NKT photonics (NKT Photonics, 2013a).

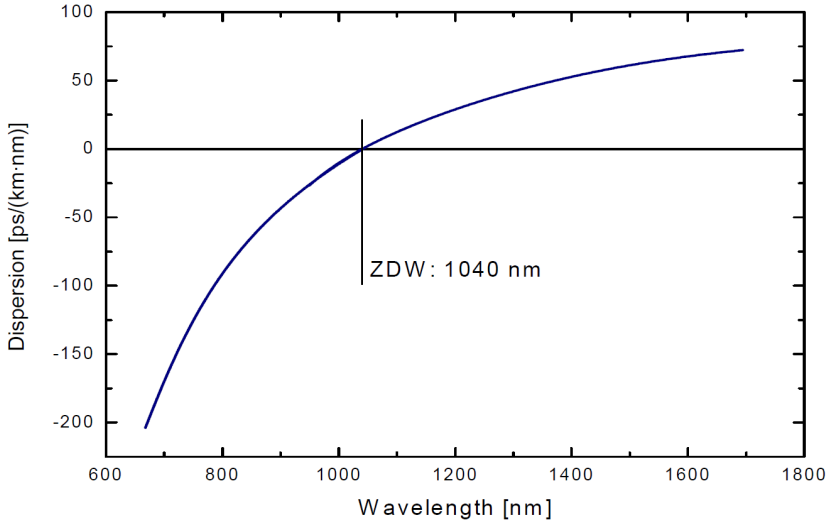

Figure 5.8: Zero dispersion photonic crystal fibre – Dispersion relation of the photonic crystal fibre with a zero dispersion wavelength at 1040 nm. At wavelength shorter than the ZDW the dispersion is in the normal dispersion regime, whereas at longer wavelengths the dispersion is in the anomalous regime. Figure obtained from the specification sheet of the SC-5.0-1040 fibre from NKT photonics (NKT Photonics, 2013b).

5.3 Experimental results

5.3.1 Amplification

The average power of the signal after the first two pre-amplification stages was 1.5 W with pulse durations of 1.7 ps. Pump powers of 210 mW and 5.4 W were used for the first and second stages respectively. It was possible to amplify the signal up to 3 W of average power, however we found that the long term stability of the launch tip of the single mode fibre, leading to the second taper, was considerably worse at powers above 1.5 W. Figure 5.9 shows the average power obtained following the power amplifier at various pump powers. 40 W was the highest output power we obtained limited by pump absorption due to the length of the available amplifier fibre, which had to be shortened

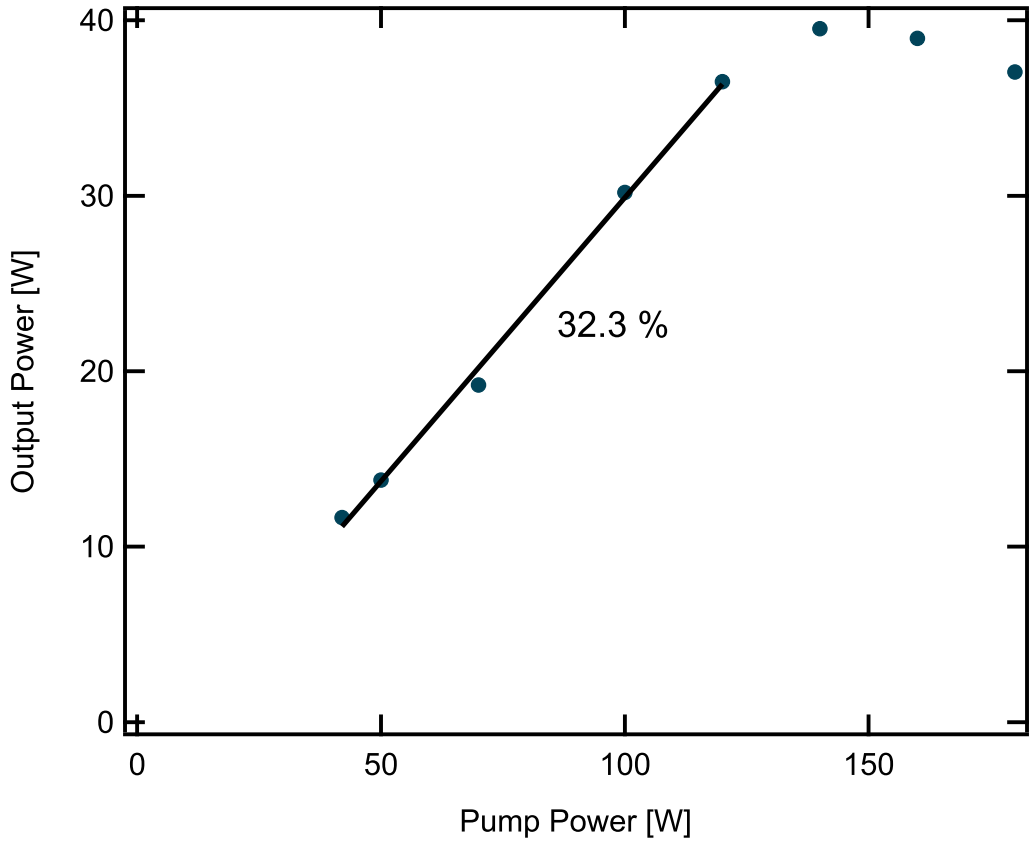

Figure 5.9: Amplified average power – The average power obtained following the power amplifier at various pump powers. 40 W at 130 W pump power was the highest output power obtained. The average power was limited by pump absorption, due to the length of the availlable amplifier fibre, evident in the output power drop at pump powers above 130 W.

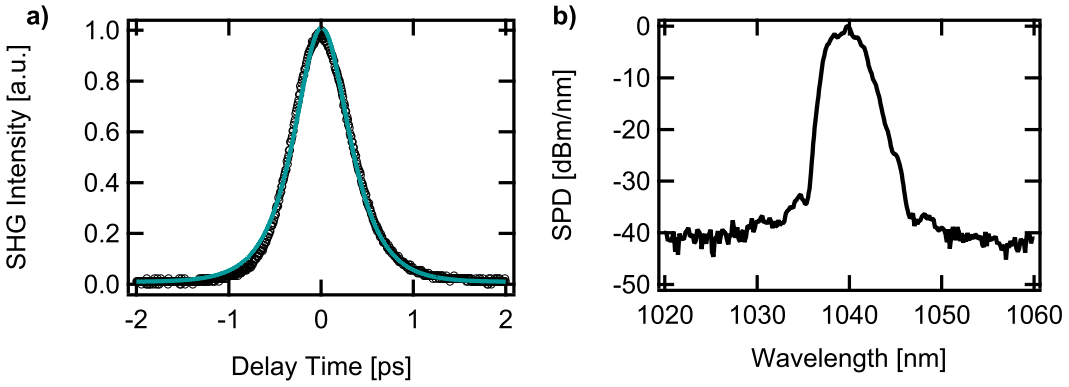

Figure 5.10: Autocorrelation and spectrum of the compressed pulse – a) Shows the autocorrelation (black) with a sech^2 fit (blue). b) Shows the spectrum measured following the recompression of the pulse. The duration of the recompressed pulse was 400 fs.

due to failures of the taper. The low slope efficiency of 32.3 % is thought to be due to the insufficient saturation of the gain and limited pump absorption. This is also evident at pump powers above 130 W where the average output power drops with increasing pump power.

The pulse duration after the final stage power amplifier was 3 ps at an average power of up to 40 W (Figure 5.11 b)). This pulse elongation was predominantly due to the fibre dispersion in the amplifier system. The obtained average powers were still in the linear amplification regime and so no significant spectral broadening could be observed and no complex phase structure was added by the amplifier chain.

It was possible to recompress the pulses to their original duration of 400 fs, as shown in Figure 5.10, with a 70 % throughput efficiency and a grating separation of approximately 2 cm. Figure 5.11 shows the pulse durations after each stage of the set-up. Scaling the average power to higher powers, $\sim$ 100 W, at which the system was designed to be in the parabolic pulse amplification regime would have allowed pulse compression to sub-original durations.

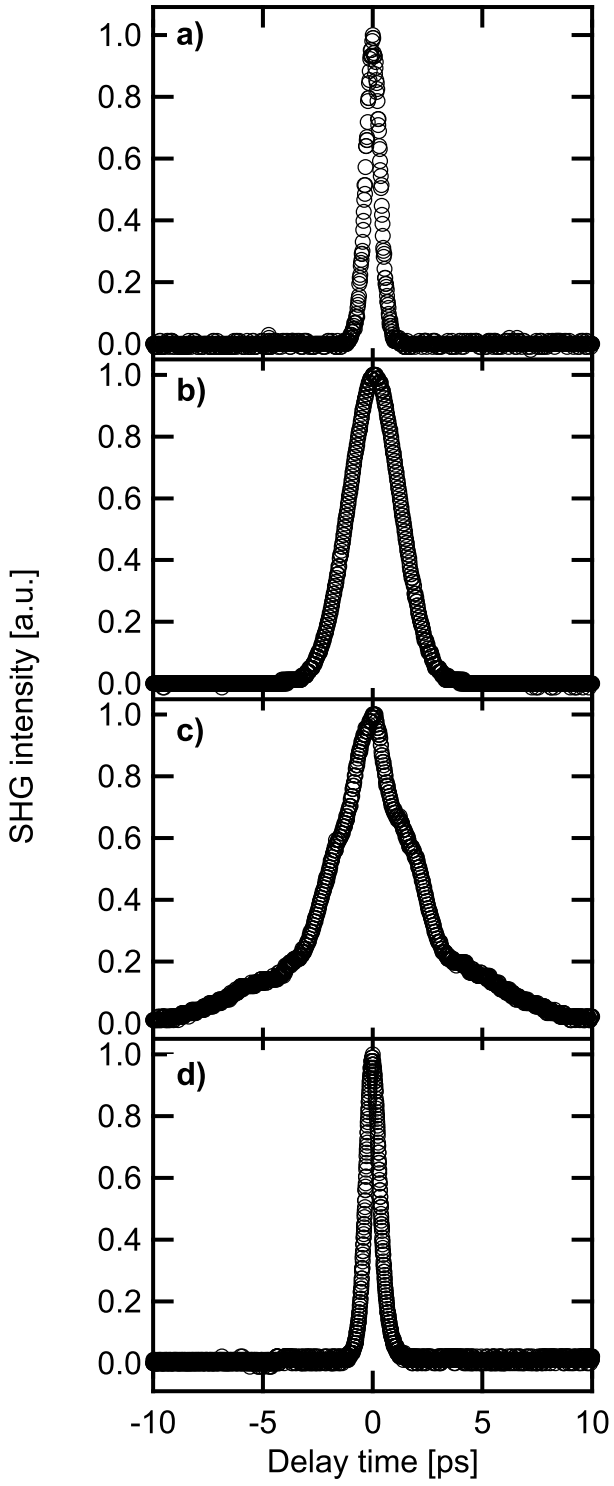

Figure 5.11: Autocorrelations after each stage of the set-up – a) Pulse of the ML-VECSEL, with a duration of 400 fs b) Pulse measured after the first two pre amplifiers, with a duration of 1.7 ps c) Measured pulse after the final stage amplifier at 40 W average power exhibiting a duration of 3 ps d) Autocorrelation of the pulse following recompression, down to a pulse duration of 400 fs, of the amplified pulses (c)).

5.3.2 Supercontinuum generation

The recompressed 400 fs pulses were launched into the two PCFs in turn, achieving in each case a transmission efficiency of $\sim 50\%$. The maximum average powers measured after the PCFs are 2.5 W and 3.9 W for the PCF pumped closely to its ZDW and all-normal dispersion PCF respectively, limited by thermal management of the passively cooled launch into the PCF. Figures 5.12 and 5.13 show the spectra of the supercontinuum generated with the VECSEL MOPA system. The 20 dB-bandwidth of the supercontinuum created with the all-normal dispersion PCF is 200 nm (Figure 5.12). We expect this supercontinuum to have a high degree of coherence, as the pulse predominantly acquires a linear chirp and it should be compressible with appropriate dispersion compensation (Heidt, 2010; Chow et al., 2006).

A 280 nm 20 dB-bandwidth supercontinuum is measured for the PCF with a ZDW of 1040 nm (Figure 5.13). The supercontinuum had spectral components between 750 nm and 1300 nm. The dip at about 900 nm is typical for PCFs with a ZDW and is due to the relation between the pump wavelength and the dispersive properties of the PCF, however for a detailed explanation a numerical model would be necessary (Dudley et al., 2006). In the case of the supercontinuum generation with a PCF with a ZDW the supercontinuum is thought to be temporally incoherent as the pulse duration launched into the PCF is significantly above 100 fs (Dudley et al., 2006).

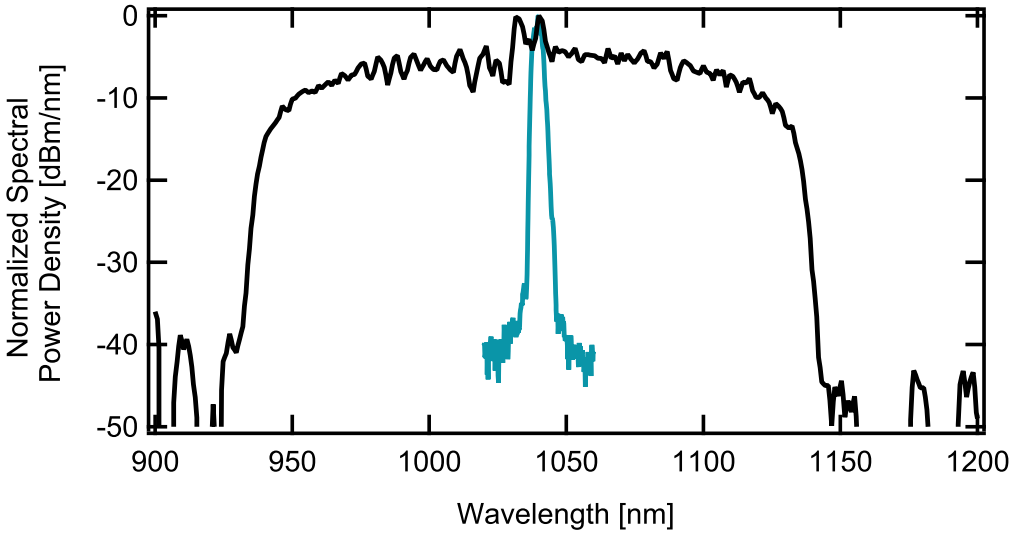

Figure 5.12: Supercontinuum generation with a all-normal dispersion PCF – Measured input spectrum (blue) and supercontinuum spectrum produced with the all-normal dispersion PCF (black). The 20 dB-bandwidth of the supercontinuum is 200 nm.

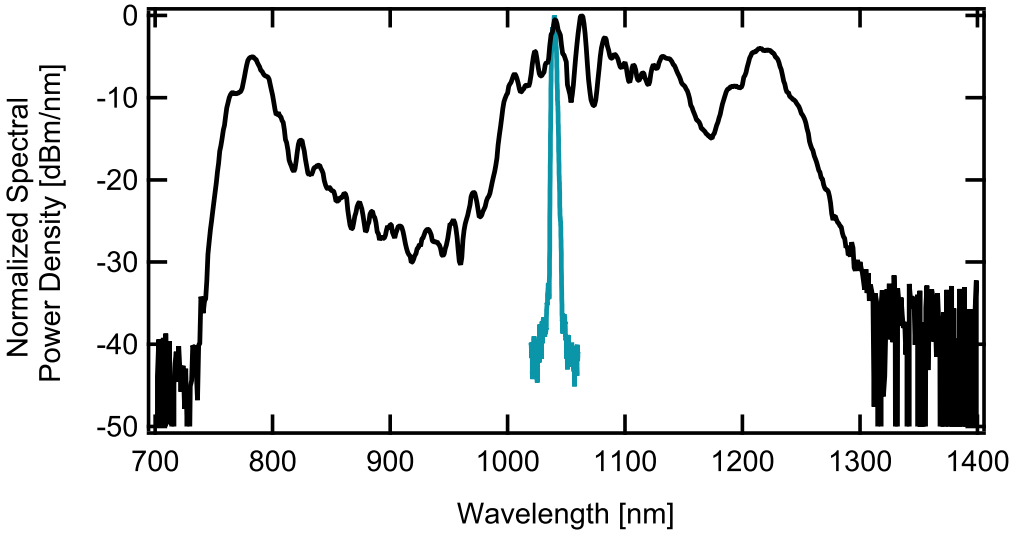

Figure 5.13: Supercontinuum generation with a PCF with a ZDW at 1040 nm – Measured input spectrum (blue) and supercontinuum spectrum produced with the PCF with a ZDW of 1040 nm (black). The 20 dB-bandwidth of the supercontinuum is 280 nm where spectral components can be observed between 750 nm and 1300 nm.

5.4 Conclusion

We have demonstrated that the combination of femtosecond ML-VECSELs and fibre amplifiers can be used to generate supercontinuum at multi-GHz repetition rates at average powers of several Watts (in a robust and practical system). Supercontinuum with a 20 dB bandwidth width of 280 nm and an average output power of 2.5 W was achieved with a PCF pumped close to its ZDW. For supercontinuum generated with all-normal dispersion PCF a 20 dB spectral bandwidth of 200 nm was achieved with an average output power of 3.9 W. The VECSEL-MOPA produced up to 40 W output power at a 3 GHz repetition rate. The pulses were re-compressed to 400 fs durations using a high throughput transmission grating compressor.

This work represents a first stepping stone towards VECSEL driven frequency combs and up to now no coherent octave-spanning supercontinuum seeded by a VECSEL, directly nor amplified, has been reported.

As our main limitation was the power handling of the PCF tip the follow-up experiment utilizes a two-stage fibre amplifier system that can achieve average output powers of $\sim$ 20-25 W. This system is based on a 10-μm core ytterbium fibre and should operate in the parabolic amplification regime at average powers above 15 W. This system should enable us to produce compressed pulses with durations of 100 fs at an average power of $\sim$ 10 W which we know can be handled by the PCF. The repetition rate of the VECSEL will be decreased to 1 GHz further increasing the peak power and improving the chance to generate coherent octave-spanning supercontinuum.

High average power, 39 W, supercontinuum generation with a PCF has been reported by Chen et al. (2010a) and we aim to use techniques developed in that work along with PCF with optimized dispersion characteristics, a ZDW shorter than the pump wavelength, to generate higher average-power and broader bandwidth supercontinuum in the future.

References

Agrawal, G. P. (2001). *Non-linear Fiber Optics 3rd ed.* (Academic, San Diego).

Bartels, A., Heinecke, D., and Diddams, S. A. (2009). 10-GHz Self-Referenced Optical Frequency Comb. *Science*, 326:681.

Broderick, N. G. R., Monro, T. M., Bennet, P. J., and Richardson, D. J. (1999). Nonlinearity in holey optical fibers: measurement and future opportunities. *Optics Letters*, 24(20):1395–1397.

Chamorovskiy, A., Kerttula, J., Rautiainen, J., and Okhotnikov, O. G. (2012). Supercontinuum generation with amplified 1.57 μm picosecond semiconductor disk laser. *Electronics Letters*, 48(16):1010–1012.

Chen, K. K., Price, J. H. V., Alam, S., Hayes, J. R., Lin, D., Malinowski, A., Codemard, C., Ghosh, D., Pal, M., Bhadra, S. K., and Richardson, D. J. (2010a). Picosecond fiber MOPA pumped supercontinuum source with 39 W output power. *Optics Express*, 18(6):5426–5432.

Chen, K. K., Price, J. H. V., Alam, S., Hayes, J. R., Lin, D., Malinowski, A., and Richardson, D. J. (2010b). Polarisation maintaining 100W Yb-fiber MOPA producing μJ pulses tunable in duration from 1 to 21 ps. *Optics Express*, 18(14):14385–14394.

Chow, K. K., Takushima, Y., Lin, C., Shu, C., and Bjarklev, A. (2006). Flat supercontinuum generation based on normal dispersion nonlinear photonic crystal fibre. *Electronics Letters*, 42(17):989–990.

Dudley, J. M., Genty, G., and Coen, S. (2006). Supercontinuum generation in photonic crystal fiber. *Reviews of Modern Physics*, 78(4):1135–1184.

Dupriez, P., Finot, C., Malinowski, A., Sahu, J. K., Nilsson, J., Richardson, D. J., Wilcox, K. G., Foreman, H. D., and Tropper, A. C. (2006). High-power, high repetition rate picosecond and femtosecond sources based on Yb-doped fiber amplification of VECSELs. *Optics Express*, 14(21):9611–9616.

Eidam, T., Hanf, S., Seise, E., Andersen, T. V., Gabler, T., Wirth, C., Schreiber, T., Limpert, J., and Tünnermann, A. (2010). Femtosecond fiber CPA system emitting 830 W average output power. *Optics Letters*, 35(2):94–96.

Fermann, M., Kruglov, V., Thomsen, B., dudley, J., and Harvey, J. (2000). Self-Similar Propagation and Amplification of Parabolic Pulses in Optical Fibers. *Physical Review Letters*, 84(26):6010–6013.

Fortier, T. M., Bartels, A., and Diddams, S. A. (2006). Octave-spanning Ti:sapphire laser with a repetition rate >1 GHz for optical frequency measurements and comparisons. *Optics Letters*, 31(7):1011–1013.

He, F., Price, J. H. V., Vu, K. T., Malinowski, A., Sahu, J. K., and Richardson, D. J. (2006). Optimisation of cascaded Yb fiber amplifier chains using numerical-modelling. *Optics Express*, 14(26):12846–12858.

Head, C. R., Chan, H.-Y., Feehan, J. S., Shepherd, D. P., Alam, S., Tropper, A. C., Price, J. H. V., and Wilcox, K. G. (2013). Supercontinuum Generation With GHz Repetition Rate Femtosecond-Pulse Fiber-Amplified VECSELs. *Photonics Technology Letters*, 25(5):464–467.

Heidt, A. M. (2010). Pulse preserving flat-top supercontinuum generation in all-normal dispersion photonic crystal fibers. *J. Opt. Soc. Am B*, 27(3):550–559.

Knight, J. C., Birks, T. A., Russel, P. S. J., and Atkin, D. M. (1996). All-silica single-mode optical fiber with photonic crystal cladding. *Optics Letters*, 21(19):1547–1549.

NKT Photonics (2013a). *NL-1050-NEG-1*. http://www.nktphotonics.com/files/files/NL-1050-NEG-1.pdf.

NKT Photonics (2013b). *SC-5.0-1040*. http://www.nktphotonics.com/files/files/SC-5.0-1040.pdf.

Okhotnikov, O. G., editor (2010). *Thermal management, structure design and integration considerations for vecsels, in Semiconductor Disk Lasers: Physics and Technology*. Wiley-VCH Verlag GmbH & Co. KGaA, Weinheim, Germany.

Paschotta, R. (2004). Noise of mode-locked lasers (Part II): timing jitter and other fluctuations. *Applied Physics B*, 79:163–173.

Quarterman, A. H., Wilcox, K. G., Elsemere, S., Mihoubi, Z., and Tropper, A. C. (2008). Active stabilisation and timing jitter characterisation of sub-500 fs pulse passively modelocked VECSEL. *Electronics Letters*, 44(19):1135–1137.

Stumpf, M. C., Pekarek, S., Oehler, A. E. H., Südmeyer, T., Dudley, J. M., and Keller, U. (2010). Self-referenceable frequency comb from a 170-fs, 1.5-μm solid-state laser oscillator. *Applied Physics B*, 99(3):401–408.

Telle, H. R., Steinmeyer, G., Dunlop, A. E., Stenger, J., Sutter, D. H., and Keller, U. (1999). Carrier-envelope offset phase control: A novel concept for absolute optical frequency measurement and ultrashort pulse generation. *Applied Physics B*, 69(4):327–332.

Wilcox, K. G., Foreman, H. D., Roberts, J. S., and Tropper, A. C. (2006). Timing jitter of 897 MHz optical pulse train from actively stabilised passively modelocked surface-emitting semiconductor laser. *Electronics Letters*, 42(3):159–160.

Wittwer, V. J., van der Linden, R., Tilma, B. W., Resan, B., Weingarten, K. J., Südmeyer, T., and Keller, U. (2013). Sub-60-fs Timing Jitter of a SESAM Modelocked VECSEL. *Photonics Journal*, 5(1):1400107.

Wittwer, V. J., Zaugg, C. A., Pallmann, W. P., Oehler, A. E. H., Rudin, B., Hoffmann, M., Golling, M., Barbarin, Y., Südmeyer, T., and Keller, U. (2011). Timing Jitter Characterization of a Free-Running SESAM Mode-locked VECSEL. *Photonics Journal*, 3(4):658–664.

Zhao, Z., Dunham, B. M., Bazarov, I., and Wise, F. W. (2012). Generation of 110 W infrared and 65 W green power from a 1.3-GHz sub-picosecond fiber amplifier. *Optics Express*, 20(5):4850–4855.

Chapter 6

Conclusions and Future Work

6.1 Conclusions

The work presented in this thesis demonstrates and outlines new potential applications of optical tweezers and VECSELs.

The control over the orientation of individual asymmetrical objects has been extended to nano-scale particles, further highlighting the high degree of control achievable with optical tweezers. It has been shown that the agglomerates rotate up to rotation frequencies of 320 Hz, the fastest we could rotate the polarisation of our trapping beam, suggesting that the alignment force is sufficient to overcome rotational drag forces on the nanorod agglomerates at the frequencies we were able to test. The use of rotating nanorods could be very interesting as nanomixers in microfluidics where the laminar flow enables highly accurate control over amounts of fluids but hinders mixing of different fluids.

Despite the recent increase in average power of mode-locked VECSELs to the multi-watt average power level, the need to optimize the gain structure design to obtain shorter pulse durations still remains. The novel tempo-spectral technique presented in this work allows for the observation of the curvature of the gain spectrum during actual operation and furthermore shows the evolution of the gain spectrum during lasing build up. The two investigated samples,with a resonant and an anti-resonant design, were found to have gain bandwidths of 14 and 17 nm, respectively.

High repetition rate mode-locked lasers are of interest for applications such as frequency comb generation. The scheme demonstrated in this work utilizing a fibre amplifier system to increase the average power of a femtosecond-pulsed mode-locked VECSEL to generate supercontinuum represents a first step towards VECSEL seeded frequency combs. The supercontinuum generated, with a PCF with a zero dispersion wavelength at 1040 nm, had spectral components over 500 nm. However as the coherence of the supercontinuum is crucial for frequency combs and the supercontinuum generated was thought to be incoherent, due to few hundred femtosecond pulse duration, a second PCF was used that had an all-normal dispersion profile, generating a supercontinuum with a spectral bandwidth of 200 nm.

6.2 Future work

6.2.1 Vibrational spectroscopy

In this project I propose to excite and detect vibrational modes of nano-scale objects, isolated and immobilized in an optical trap, with a tunable repetition rate VECSEL. Thus capitalising on my unique combination of experience which covers both of these areas. To provide a proof of principle of this novel concept it will be trialled in a test bed with gold particles, which have a well-known resonance frequency.

Wine glasses can be broken with hammers but this does not enable significant scientific observations. In a more refined and useful manner, wine glasses can also be made to oscillate to the level of breaking using only sound waves if the frequency of the sound is resonant with the vibrational resonance of the glass's shape.

Similar to wine glasses, objects in the nano-scale regime such as gold particles and viruses also have resonant frequencies, albeit in the gigahertz instead of the kilohertz regime. Laser systems currently used to investigate vibrational behaviour of nano-scale objects are based on $\sim$ 80 MHz repetition rate lasers. These systems are complex, do not work in real time and cannot resonantly excite nano-scale objects. Thus they are more the hammer to the wineglass approach.

VECSELs naturally operate in the GHz repetition rate regime and as demonstrated by Sieber et al. (2011) and Wilcox et al. (2011) continuous tuning of the pulse repetition rate is possible over a wide range of frequencies. By tuning the repetition rate to the vibrational resonance of the nanoparticle, it is possible to resonantly drive the vibrations of the particle into the potentially non-linear mechanical regime. This has previously not been possible. Furthermore the ability to continuously tune the repetition rate of a VECSEL over several GHz can be used to investigate and address specific vibrational resonances of nano-scale objects.

For experimental reasons it is currently necessary to attempt to observe resonance phenomena while the object of interest is supported on a substrate, which greatly dampens the response. In optical traps individual nano-scale objects can be investigated without

the presence of a substrate and thus yield far greater Q factors (as recently demonstrated by Ruijgrok et al. (2012)). The combination of the VECSELs ability to resonantly excite vibrational modes in combination with optical trapping is an exciting new prospect that could deliver many interesting insights into vibrational behaviour of nano-scale objects.

References

Ruijgrok, P. V., Zijlstra, P., Tchebotareva, A. L., and Orrit, M. (2012). Damping of Acoustic Vibrations of Single Gold Nanoparticles Optically Trapped in Water. *Nanoletters*, 12:1063–1069.

Sieber, O. D., Wittwer, V. J., Mangold, M., Hoffmann, M., Golling, M Südmeyer, T., and Keller, U. (2011). Femtosecond VECSEL with tunable multigigahertz repetition rate. *Optics Express*, 19(23):23538–23543.

Wilcox, K. G., Quarterman, A. H., Beere, H. E., Ritchie, D. A., and Tropper, A. C. (2011). Variable repetition frequency femtosecond-pulse surface emitting semiconductor laser. *Applied Physics Letters*, 99:131107.

Appendix A

Nomenclature

AR	Anti Reflection
BS	Beam Splitter
CW	Continuous-Wave
CM	Cold Mirror
DBR	Distributed Bragg Reflector
DLP	Degree of Linear Polarisation
FFT	Fast Fourier Transformation
FWHM	Full Width Half Maximum
GDD	Group Delay Dispersion
HR	High Reflector
LD	Laser Diode
LMA	Large Mode Area
LPF	LongPass Filter
MIXSEL	Mode locked Integrated eXternal-cavity Surface Emitting Laser
ML	Mode-Locked
MOPA	Master Oscillator Power Amplifier
NA	Numerical Aperture
NBS	Non-Polarising BeamSplitter
NIR	Near InfraRed
OC	Output Coupler

PBS	Polarising BeamSplitter
PCF	Photonic Crystal Fibre
PD	PhotoDiode
PL	PhotoLuminescence
PMT	PhotoMultiplier Tube
QW	Quantum Well
SESAM	SEmiconductor Saturable Absorber Mirror
SPF	ShortPass Filter
SPM	Self-Phase Modulation
TEM	Transmission Electron Micrographs
VECSEL	Vertical-External-Cavity Surface-Emitting Laser
ZDW	Zero-Dispersion Wavelength

Appendix B

List of publications

Head, C. R., Chan, H.-Y., Feehan, J. S., Shepherd, D. P., Alam, S., Tropper, A. C., Price, J. H. V., and Wilcox, K. G. (2013). Supercontinuum Generation With GHz Repetition Rate Femtosecond-Pulse Fiber-Amplified VECSELs. *Photonics Technology Letters*, 25(5):464–467.

Head, C. R., Kammann, E., Zanella, M., Manna, L., and Lagoudakis, P. G. (2012). Spinning nanorods - active optical manipulation of semiconductor nanorods using polarised light. *Nanoscale*, 4:3693–3697.

Head, C. R., Wilcox, K. G., Morris, O. J., Turnbull, A. P., Farrer, I., Beere, H. E., Ritchie, D. A. and Tropper, A. C.(2013). Spectral gain and cavity loss characterization of an optically-pumped external-cavity surface-emitting quantum well laser. *Conference on Laser and Electro-Optics CLEO/Europe, Munich, Germany (12-16 May 2013)*,

Head, C. R., Chan, H.-Y., Feehan, J. S., Shepherd, D. P., Alam, S., Tropper, A. C., Price, J. H. V., and Wilcox, K. G. (2013). Supercontinuum Generation with femtosecond pulse fiber amplified VECSELs. *Proceedings of SPIE Photonics West, San Francisco, USA (18 February, 2013)* , 860608.

Morris, O. J., Wilcox, K. G., Head, C. R., Turnbull, A. P., Farrer, I., Beere, H. E., Ritchie, D. A. and Tropper, A. C.(2013). Effects of cryogenic temperatures on the performance of CW VECSELs. *Proceedings of SPIE Photonics West, San Francisco, USA (18 February, 2013)* , 86060L.

Turnbull, A. P., Wilcox, K. G., Head, C. R., Morris, O. J., Farrer, I., Ritchie, D. A. and Tropper, A. C.(2013). Generation of 200-fs pulses with a short microcavity VECSEL. *Proceedings of SPIE Photonics West, San Francisco, USA (18 February, 2013)* , 86060O.

Wilcox, K. G., Quarterman, A. H., Apostolopoulos, V., Morris, O. J., Head, C. R., Turnbull, A. P., Beere, H. E., Farrer, I., Ritchie, D. A., and Tropper, A. C. (2012). Femtosecond semiconductor laser emitting high average power 175-GHz pulse train. *Conference on Lasers and Electro-Optics CLEO/US, San Jose, USA (6-11 May, 2012)*, JW2A.102

Morris, O. J., Wilcox, K. G., Head, C. R., Turnbull, A. P., Mosley, P. J., Quarterman, A. H., Kbashi, H. J., Farrer, I. Beere, H. E., ritchie, D. A., and Tropper, A. C. (2012). A wavelength tuneable 2-ps pulse VECSEL *Proceedings of SPIE Photonics West, San Francisco, USA (9 February, 2012)* 824212